Development of corrosion resistant coatings for Mg alloys and a general corrosion fatigue model

by

Jie Wang

A thesis
presented to the University of Waterloo
in fulfillment of the thesis requirement for the degree of
Doctor of Philosophy
in
Mechanical and Mechatronics Engineering

Waterloo, Ontario, Canada, 2020

Examining Committee Membership

The following served on the Examining Committee for this thesis. The decision of the Examining Committee is by majority vote.

External Examiner	DANIEL KUJAWSKI, Ph.D. Professor, Western Michigan University
Supervisor	HAMID JAHED, Ph.D. Professor, University of Waterloo
Supervisor	GRZEGORZ GLINKA, Ph.D. Professor, University of Waterloo
Supervisor	XIN PANG, Ph.D. Adjunct assistant Professor, University of Waterloo Research Scientist, Natural Resources Canada
Internal Member	HYOCK JU KWON, Ph.D. Associate Professor, University of Waterloo
Internal Member	ROBERT VARIN Ph.D. Adjunct Professor, University of Waterloo
Internal-External Member	ADIL AL-MAYAH, Ph.D. Associate Professor, University of Waterloo

Authors Declaration

I hereby declare that I am the sole author of this thesis. This is a true copy of the thesis, including any required final revisions, as accepted by my examiners.

I understand that my thesis may be made electronically available to the public

Abstract

Mg alloys find widespread applications in transportation industries especially in cars and trucks because of their edges in light-weight design, which can greatly help improve the fuel efficiency and decrease the greenhouse gas emissions of vehicles. However, Mg alloys' high susceptibility to corrosion limit their penetration in automotive applications. Surface coating is one of the most effective and economic ways to protect Mg alloys from corrosion and thus one major aim of this thesis comes to identify a robust and cost-effective surface coating system for Mg alloys. As most Mg automotive components are subjected to corrosion and cyclic load simultaneously, another focus of this work is the development of corrosion fatigue model suitable for Mg alloys.

First, after reviewing various surface treatment methods available for Mg alloys in literature Mn-P conversion coating was chosen to treat cast Mg alloy AZ31B for corrosion protection and surface protection. The conversion coating process was optimized by studying the effects of processing parameters such as solution temperature, pH value, processing time, and chemical composition of the coating bath on the surface morphology, thickness, microstructure, and corrosion behavior of the Mn-P coating using SEM/EDS and electrochemical testing methods. Based on the results of optimization experiments, a new two-stage conversion coating process was developed to obtain thick and crack-free Mn-P conversion coating on Mg alloys with excellent coating quality. Results of salt spray corrosion test and electrochemical test showed that the conversion coating deposited from this two-stage process had a better corrosion performance than that produced from a single coating process. To attain further corrosion protectiveness, a top polymer painting was applied on Mg alloy pretreated via a variety of surface treatment techniques (i.e. Mn-P conversion coating, chromate conversion coating (CCC), and micro-arc oxide coating (MAO)). In this study, extrusion/forged AZ80 and ZK60 alloys were used as the substrates for evaluating the efficacy of various coating systems. Corrosion tests of the Mg alloys with and without scribes in the salt spray chamber (ASTM B117) were used to characterize the coating properties. The results indicated that the MAO-powder coating system could provide the best corrosion performance for the ZK60 alloy without a scribe while CCC-powder coating system could provide the best corrosion performance for the ZK60 alloy with a scribe.

Next, more attention was placed to the work on modeling of corrosion fatigue behavior of Mg alloys. A process interaction model is proposed to be used to describe the corrosion fatigue crack growth life, assuming that corrosion fatigue is an interaction process between pure fatigue and stress corrosion cracking. In this model, corrosion fatigue crack propagation is divided into three parts: i) when stress intensity factor K is smaller than K_{ISCC}, no stress corrosion cracking occurs, and corrosion fatigue crack propagation rates are only contributed by fatigue described by modified Kujawski's model, in which two correlating parameters were introduced to explain the interactive effects of corrosion and cyclic loading on the material’s properties and the driving force ; ii) When K exceeds K_{ISCC}, stress corrosion cracking starts to kick in and join with modified fatigue to enhance corrosion fatigue crack growth rates; iii) With stress intensity factor K further increasing to a certain value where stress corrosion cracking is being independent to K, the effect of corrosion on the driving force of fatigue crack propagation can be neglected while the influence of corrosion on material properties still exists. Data of fatigue in vacuum and stress corrosion cracking for materials such as 4340 steel, 7075-T651, and Titanium alloy Ti-6Al-4V are used to validate this model and good agreements are obtained between the predictive corrosion fatigue crack growth rates and practical experiment results.

Acknowledgements

I would like to express my sincere gratitude to my supervisor, Professor Hamid Jahed, and my co-supervisors, Dr. Xin Pang, and Professor Gregory Glinka, for their invaluable supports, guidance, motivation, and patience at every step of this research work.

I would also like to thank Dr. Behzad Behravesh, Siavash Borhan Dayani, Shi Chao, Dulal Saha, and Yuna Xue for their aid in performing experimental work and sharing their exceptional research experience.

Lastly, I owe my deepest gratitude to my amazing parents and my brother for their unconditional love and inspiration throughout my educational life. This work would not have been possible without their unfailing support.

Table of Contents

List of Figures

List of Tables

Chapter 1 Introduction

Known as the green metal of 21st century, magnesium (Mg) and its alloys are becoming widely recognized as increasingly important materials in automobile industry, electronic components and aircrafts, etc. Despite the many excellent properties that Mg alloys possess such as high strength/density ratio and good dimension stability, these materials exhibit inferior corrosion performances when in contact with aqueous environment and other metals. This has become one of the major obstacles preventing widespread applications of Mg alloys. This chapter places an emphasis on answering these questions: why choose magnesium and what are the major challenges magnesium alloys are facing for automotive applications (thesis motivation)? What are the causes of these issues, how serious they are, and what are the possible solutions (problem statement)? What challenges do we plan to address in this work and what are the specific techniques and approaches that we are going to use (thesis objectives and methodology)?

1.1 Technical background and research motivation

Magnesium alloys are considered to be an excellent choice for engineering applications where weight is a critical design element. For automotive applications, according to the United States Automotive Materials Partnership (USAMP), it was estimated that 500 lbs of steel and 130 lbs of aluminum per vehicle will have been replaced by 350 lbs of magnesium alloys by this year. That is an overall weight reduction of 15%, which will lead to 9%-12% fuel savings and a significant drop in gas emissions [1]. Moreover, the improvement of the vehicle's handling and turning capabilities and reduction in vibration and overall noise could be achieved through the use of magnesium alloys. Besides, magnesium alloys' advantages in the recyclability and the castability greatly reduce the cost of the material. All of these make magnesium alloys highly competitive to aluminum and steel alloys in applications for the automobile industry [2-6].

However, Mg alloys are very susceptible to corrosion in humid environments especially the environments containing chloride ions even though a partially protective film forms on the surface of Mg alloys. The corrosion potential of Mg in a NaCl solution is the least noble among all engineering metals. A lot of research attention has been attracted to investigations on corrosion mechanisms of Mg alloys and approaches to improve corrosion resistance of Mg alloys. Among the various corrosion mitigation strategies, surface coating is considered one of the most effective and economic ways to prevent corrosion of Mg alloys. It provides a physical barrier between the corrosive environments and the Mg alloy substrate, and/or can considerably increase the polarization resistance of the alloy substrate and hence retard its corrosion significantly. Commonly used coating methods included anodizing, plating, chemical conversion, powder coating, electro-coat, vapor deposition and cold spraying.

A lot of research works on Mg corrosion focused on circumstances where mechanical load is not involved, and most of the protective coatings developed are for load-free applications. In real service conditions, especially for automobiles, structures and components are commonly exposed to both cyclic mechanical loading and corrosive environment (e.g water, salt, and road debris), which may lead to the occurrence of premature break down or failure of the material, a phenomena termed corrosion fatigue. According to NACE/ASTM G193 standard, corrosion fatigue is defined as the process wherein a metal fractures prematurely under conditions of simultaneous corrosion and repeated cyclic loading at lower stress levels or fewer cycles than what would be required to cause fatigue of that metal in the absence of the corrosive environment. Considering a scenario of pure mechanical fatigue, the evaluation criterion of material resistance to fatigue is the fatigue limit (σ_c) or fatigue strength, expressed by the stress amplitude below which the material will endure an infinite number of cycles or at least a number of determined cycles such as 1.0×10^7. Mg alloys show good fatigue strength in the air. Once they are exposed to an aggressive environment, however, their fatigue strength will be significantly reduced due to the interaction of cyclic load and corrosion. Corrosion fatigue can cause much worse damages than merely fatigue or corrosion or even the summation of fatigue and corrosion, because corrosion and fatigue can mutually promote each other. For example, corrosion pits easily resulted from electrochemical reactions on the Mg alloy surface can act as a stress raiser and hence facilitate the fatigue crack initiation; and hydrogen generated from corrosion reactions may diffuse into the Mg alloy and embrittle the material. In turn, cyclic loading could also increase the corrosion rate by changing the local electrochemical environments such as lowering the local pH value at the crack tip via solution refreshing or backflow during the repeated crack open/closure. Additionally, Mg alloys have hexagonal close packed (HCP) crystal structure and limited slip systems, and thus their fatigue damage mechanisms are different from those of steels and Al alloys which have body-centered cubic (BCC) or face-centered cubic (FCC) crystal structures. All the above make the understanding of corrosion fatigue of Mg alloys a far from simple task.

1.2 Problem statement and scope of work

Due to the inferior corrosion resistance of Mg and its alloys, plenty of work has been done on development of corrosion resistant coatings for protection of Mg alloys in various environments [7-13]. And the stress corrosion cracking (SCC) and corrosion fatigue of Mg and its alloys are also under active investigations. Nevertheless, little work has been seen in literature investigating the corrosion fatigue performances of Mg alloys with protective coatings. It is still not fully understood how factors such as the types of coatings, coating qualities, and various coating processing procedures influence the corrosion fatigue properties of the coated Mg alloys. And there is a lack of understanding on how surface coatings on Mg alloys interact with the corrosive environment and cyclic load in determining the fatigue life of the materials. These critical issues need to be addressed to ensure safe and economic utilization of Mg alloys in real industrial applications.

Besides experimental investigations, computational modeling is a powerful tool that can be used to study the behavior of a complex system. Modeling of corrosion fatigue behavior of the coated Mg alloys can assist in safety assessment of engineering structures and allow better component design minimizing the risk of corrosion fatigue damage. The corrosion fatigue life of a material or structure includes two parts: corrosion fatigue crack initiation (CFCI) time and corrosion fatigue crack propagation (CFCP) time. In order to model the total corrosion fatigue life of coated Mg alloys, how the coating influences the CFCI life and CFCP life needs to be understood first.

In order to quantify the effects of surface coating on corrosion fatigue life of Mg alloys, fully understanding of the corrosion mechanism and corrosion performances of coated Mg alloys are needed. In the present study, permanganate phosphate (Mn-P) conversion coating is chosen as a model coating for investigating the corrosion and corrosion fatigue behavior of coated Mg alloys. Chemical conversion coatings are characterized by its good corrosion resistance, low-cost and easy implementation and thus are extensively utilized for surface pretreatment of metals in automotive industry. Chromate conversion coating is well-recognized for its excellent corrosion resistance, but it has been prohibited due to the adverse environmental impact of the highly toxic Cr^{6+} used in the process. Mn-P conversion coating is opted in this study as it is considered one of the most promising alternative coatings to the chromate conversion coating. In this work, coating process was optimized to obtain dense protective Mn-P conversion coating on Mg alloys and the corrosion mechanism and corrosion behavior of the coated and uncoated Mg alloys were investigated. Surface coating apparently is expected to increase the CFCI life, but the actual effect very much depends on the mechanical properties and capability of the coating to maintain its integrity and protectiveness under the cyclic loading. For example, if the surface coating is very brittle like anodized coating or has internal net cracks like chromate conversion coating, the effect of the surface coating on CFCI may be very mild or even negligible. Modelling of CFCI life can be obtained by calculating the corrosion pit growth rate. A few CFCI models are reported in literature, most of which are established by simulating the pit growth behavior. However, verification of the CFCI model using experimental data can be very tricky and complicated because of the complex pit growth behavior and the difficulty in distinguishing the boundary between CFCI and CFCP. Besides, research work on the effect of cyclic loading on the pit growth behavior is rare. In this work, experimental investigations were done to study the corrosion behavior of Mg alloys with various coatings, so as to better understand and quantify the effect of surface coating on CFCI process

The effect of surface coating on CFCP behavior remains unclear because it seems that surface coating tends to influence the stage of CFCI rather than CFCP, but the fact is that the corrosion pit in the coating may act as a stress raiser and increase the CFCP rate. Modeling of CFCP life of coated Mg alloys can be realized by calculating the CFCP rate. The previous CFCP models in literature, such as the superposition model and the competition model, stated that the CFCP rate was closely related to pure mechanical fatigue, SCC, and the interaction of these two processes. However, those models were initially developed for structural steels and aluminum alloys that are only susceptible to SCC at high stress intensities. As to Mg alloys, they are generally more susceptible to SCC. Some susceptibility indexes such as I_{th} (defined as the ratio of threshold stress for SCC in the corrosive environment to that in the air) were used to characterize the tendency of Mg alloys. Even in distilled water, for some Mg alloys, the value of I_{th} can be reduced to approximately 0.6 [14]. More facts on SCC of Mg alloys will be discussed in the next chapter. Therefore, the previous models cannot be used directly to describe the corrosion fatigue behavior of Mg alloys. A new model with the ability to predict the CFCP behavior of Mg alloys is therefore necessary.

1.3 Research objectives and methodology

The overall objectives of this research include identification of a robust surface coating for the investigation of corrosion and corrosion fatigue behavior of magnesium alloys and computational modelling of corrosion fatigue behavior for the coated Mg alloys. Mg alloys treated with various types of laboratory synthesized and industrial coatings will be evaluated for corrosion and corrosion fatigue performances in order to understand the effects of surface coatings and coating processes on the corrosion performances and corrosion fatigue life of Mg alloys. One major goal of the study is to identify a robust and cost-effective surface coating for the corrosion protection of fatigue-critical automotive components such as suspension arm made of Mg alloys.

To achieve the above research goal, the following objectives are planned and conducted:

1- Identify a robust surface coating for Mg. In the first stage of the study, Mg alloy AZ31B was treated with Mn-P conversion coatings in laboratory. The coating process was optimized in order to produce Mn-P coatings of high quality. The effects of processing parameters such as solution temperature, pH value, processing time, and chemical composition of the coating bath on the surface morphology, thickness, microstructure, and corrosion behavior of the Mn-P coating were investigated using SEM and electrochemical testing methods. A new two-stage process was developed in order to obtained thick and crack-free Mn-P conversion coatings on Mg alloys.

2- Characterize the effect of commercially available top coatings on corrosion and corrosion fatigue of Mg alloys. In the second stage, the candidate Mg alloys were treated with various commercially available surface coatings commonly used in automotive industry. The corrosion and corrosion fatigue performances of the Mg alloys with surface coatings (including the Mn-P coating) were evaluated using advanced electrochemical testing techniques (i.e. open circuit potential test, potentiodynamic polarization, and electrochemical impedance measurement), salt spray corrosion testing, and rotating-bending fatigue testing in a NaCl solution. The corrosion degradation and corrosion fatigue fracture mechanisms of the coated and uncoated Mg alloys have been studied systematically. The effect of cyclic loading on the corrosion behavior of coated Mg alloys and the effects of surface coating on the corrosion fatigue behavior of Mg alloys were investigated using customized corrosion fatigue testing.

3- Develop a corrosion fatigue model capable of accounting for corrosion and fatigue interaction. At the same time, as the crucial part of the study, a CFCP model for Mg alloys based on previous CFCP models for other metals such as Al, Ti, and steel alloys will be established. In the prediction of corrosion fatigue life, both CFCI life and CFCP life are to be described explicitly for coated Mg alloys. Especially, for the CFCP model, it is divided into three stages: i) when the stress intensity factor K is lower than K_{ISCC} below which stress corrosion cracking does not occur, the only contribution to the CFCP comes from the mechanical fatigue. The corrosion fatigue process in this region can be described in terms of crack growth rate given by Kujawski's equation valid at different stress ratios $da/dN=C_f\,(\beta\Delta K^{1-\alpha}K_{max}^{\alpha})^{\theta m_f}$, where the parameters θ and β represent the effect of corrosion on the material properties "m_f" and the crack propagation driving force $\Delta K^{1-\alpha}K_{max}^{\alpha}$ for fatigue, respectively; ii) When K exceeds K_{ISCC}, stress corrosion cracking starts joining with the mechanical fatigue in accelerating the corrosion crack growth by an integration of stress corrosion cracking velocity, $2\int_{t_0}^{1/f} Cscc(\beta K)^{n}dt$, in which t_0 is the beginning time of stress corrosion cracking; iii) When the stress intensity factor K further increases to the level above which stress corrosion cracking becomes independent of K, the effect of corrosion on the driving force on fatigue crack propagation can be neglected whereas the influence of corrosion on material properties will still remain. Experimental data on CFCP and SCC of Al, Ti, and steel alloys from literature will be used to validate the model.

1.4 Thesis outline

This thesis consists of 7 chapters with the following contents.

Chapter 1, current chapters, describes the research motivation, goals, and objectives.

Chapter 2 provides a literature review including corrosion mechanism and corrosion protection methods of Mg alloys, corrosion fatigue crack initiation and corrosion fatigue crack propagation models for metals.

Chapter 3 outlines the detailed information on the investigated materials, specimen characteristics and preparation, as well as the procedure of surface coating treatments. Also, the experimental techniques and equipment to characterize the microstructure, corrosion, and corrosion fatigue performance of the coated and uncoated samples are presented in this chapter.

Chapter 4 gives the effects of the solution pH, immersion time, and bath temperature on the microstructure, corrosion behavior of the Mn-P coating. A two-stage conversion process to obtain a thick and crack-free Mn-P coating is developed, and the coating is also characterized in this chapter.

Chapter 5 involves the evaluation of several corrosion protection methods on the Mg alloy ZK60 and AZ80. An E-coat and a powder coating are both used as a topcoat for the conversion coating and micro-arc oxidation coating. Cross-section microstructure, coat thickness, and corrosion performance of these coat systems are characterized and compared in this chapter.

Chapter 6 contains a detailed description of the proposed corrosion fatigue crack propagation model based on the existing models. A verification for this model is obtained by using experimental data from Al alloys, Ti alloys, and steel alloys from literature.

Chapter 7 summarizes the conclusions of the work in chapter 4-6 and provides recommendations for the future work.

Chapter 2 Literature review

2.1 Introduction - magnesium alloys

The growing environmental issues due to serious greenhouse gas emissions necessitate the light weight design of automotive components [2-6], considering the fact that every 10% reduction in vehicle weight leads to a 7% enhancement in fuel economy [3][7]. Magnesium alloys are considered to be alternatives to steel and aluminum alloys to achieve this goal because of their high specific strength and low density and thus are increasingly utilized in the automotive, aerospace and electronics industries, etc. Table 2-1 gives a comparison of properties of magnesium alloys and other metals. From the point view of engineering design, Mg alloys may not be the best choice due to their low elastic modulus. However, for the weight-light applications, it can be seen that magnesium alloys with a density of 1.74-1.95 g/cm^3, about 2/3 that of Al and 1/4 that of Fe, have an evident edge as compared to other engineering metals. For example, by replacing a front engine cradle made of a cast aluminum alloy with a magnesium alloy, the weight could be reduced from 15.8 kg to 10.3 kg [3].

Table 2-1 Comparison of Properties of Mg alloys, Al alloys, Ti alloys, and steels [8]

Metals	Density (g/cm^3)	Young's modulus (GPa)	Yield strength (MPa)	Tensile strength (MPa)	Fracture toughness (MPa·√m)	Environmental resistance in salt water
Mg alloys	1.74-1.95	42-47	70-400	185-475	12-18	D
Al alloys	2.5-2.9	68-82	30-500	58-550	22-35	B
Ti alloys	4.4-4.8	98-120	250-1245	300-1625	14-120	A
Stainless steel	7.6-8.1	189-210	170-1000	480-2240	62-280	A
Carbon steel	7.8-7.9	200-217	250-1155	345-1640	12-200	C

Since Mg alloy was first applied to the Beetle model by Volkswagen, many R&D efforts for Mg alloys have been made by worldwide automobile companies such as Fiat and Volkswagen to reduce the weight of motor vehicles. Although Mg alloys have been used increasingly for various applications, problems related to their low cold workability and inferior corrosion properties restrict their further applications.

2.2 Corrosion and corrosion mechanism of Mg alloys

2.2.1 Review on corrosion of magnesium alloys

Low corrosion resistance of magnesium and its alloys has significantly limited their applications in automobile industry, especially when they are exposed to aqueous solutions containing aggressive species such as chlorides. Partly protective $Mg(OH)_2$ film formed on specimen surface apparently cannot prevent magnesium alloys from being attacked by corrosive solution. The high activity of magnesium and its alloys can be clearly seen from the E-pH diagram of pure Mg in water, as presented in Figure 2-1 [13]. This diagram could be simply divided into four regions: Corrosion Area (Area 1), Passivity Area (Area 2), Immunity

Area (Area 3), and an area between Corrosion area and Immunity area (Area 4). It is concluded that pure magnesium tends to be corroded in most of areas except in that small Immunity Area.

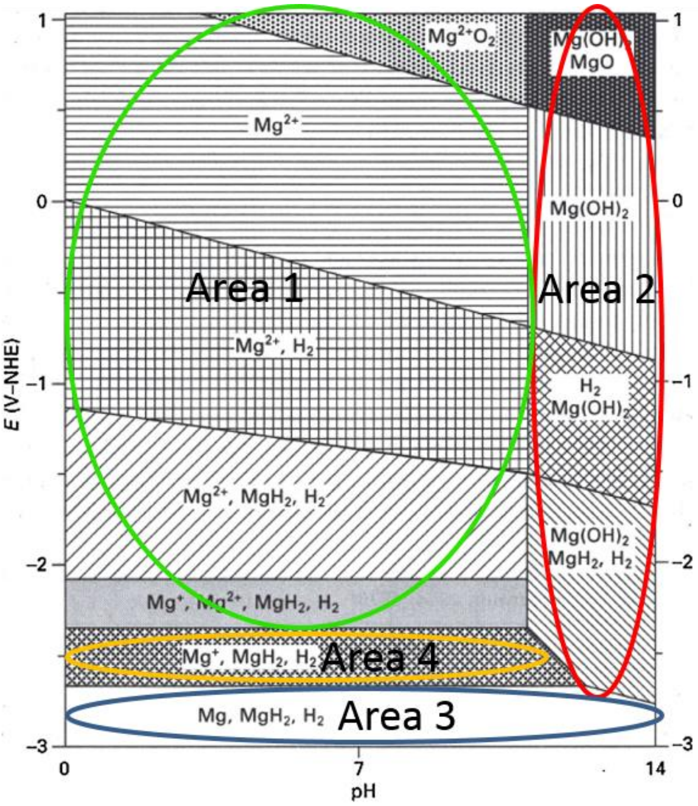

Figure 2-1 E-pH diagram of Mg in pure water [13]

For magnesium and its alloys, there is a very strange and typical manifestation related to hydrogen evolution in corrosion process, namely negative difference effect (NDE) [15]. Figure 2-2 could be used to describe this strange phenomenon in Mg corrosion process. With an electrode gradually polarized in anodic direction, hydrogen evolution rate is expected to decrease, and cathodic reaction will cease at some certain potential. However, in the case of magnesium, the hydrogen evolution rate increase with anodic polarization. Some literature has demonstrated the existence of the NDE. For example, Song et al. [16] found that hydrogen evolution rates of both MEZ and AZ91 are higher when polarized to +0.5mA/cm^2 compared to those at their corrosion potential. The most common explanation of NDE is based on a monovalent magnesium ions (Mg$^+$) theory proposed by Petty et al. [17]. The sequential reactions are presented as follows:

$$Mg \rightarrow Mg^+ + e^- \qquad 2\text{-}1$$

$$2Mg^+ + 2H_2O \rightarrow 2Mg^{2+} + 2OH^- + H_2 \qquad 2\text{-}2$$

The reaction (2-1) is an anodic reaction, and Mg$^+$ ions are strong reducing agents in the reaction. When the magnesium electrode is polarized in anodic direction, the rate of reaction (2-1) increases and thus produces more and more reductants (i.e. Mg^+ ions), which then increase the hydrogen evolution rate and perfectly explain the phenomenon NDE.

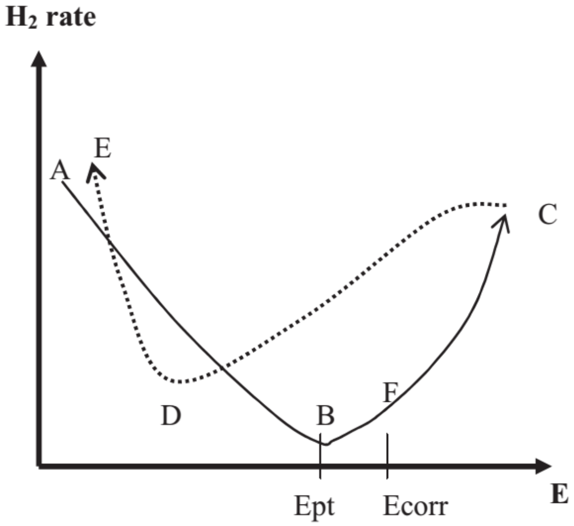

Figure 2-2 A schematic illustration of the dependence of the H_2 evolution rate from a polarized magnesium [15]

In most cases, the corrosion type of Mg alloys is localized corrosion such as galvanic corrosion and pitting corrosion [15-24]. In galvanic corrosion as shown in Figure 2-3, the Mg α-matrix acting as an anode due to its low corrosion potential readily form galvanic couples with the β phase or other intermetallic compounds that act as cathodes. The general corrosion reaction is:

Overall reaction: $Mg + 2H_2O \rightarrow Mg(OH)_2 + H_2$ 2-3

Anodic reaction: $Mg \rightarrow Mg^{2+} + 2e^-$ 2-4

Cathodic reaction: $2H_2O + 2e^- \rightarrow 2OH^- + H_2$ 2-5

As can be seen from above reactions, corrosion of Mg alloys is always accompanied by hydrogen evolution.

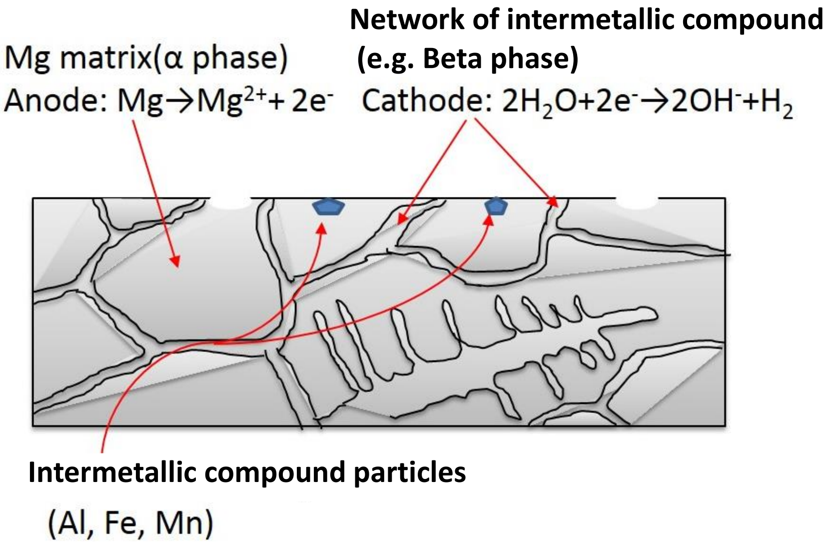

Figure 2-3 Schematic of galvanic corrosion in Mg alloys

Another common form of localized corrosion is pitting. It is in particular related to passivating alloys or alloys with protective coatings in an aggressive environment containing Cl^-, SO_4^{2-}, Br^-, etc. The preferential adsorption of halide ions to oxygen and water molecules on the surface of Mg alloys followed by the penetration of ions through the oxide film or the coatings encourages the degradation of Mg alloys. Pitting corrosion is more dangerous as the pits are usually covered by corrosion products and may act as stress concentration sites to initiate fatigue [20]. Consequently, the fatigue strength of Mg alloys in an aggressive environment decreases significantly.

2.2.2 Stress corrosion cracking

Stress corrosion cracking (SCC) often takes place in a component or structure by a combination of sustained mechanical loading and an aggressive environment. Mg and its alloys possess high susceptibility to SCC, especially the wrought magnesium alloys [25]. A lot of papers investigated the mechanism of SCC of magnesium alloys. It has been reported that this type of environment assisted cracking is generally ascribed either to preferential anodic dissolution under stress conditions or hydrogen induced embrittlement at the crack tip [26]. SCC due to anodic dissolution is usually a continuous process and it is an intergranular fracture, which is always related to some chemical heterogeneity along the grain boundaries that provide an electrochemically active path for the corrosion process to occur. Whereas SCC caused by hydrogen induced embrittlement is a discontinuous process and normally characterized as a transgranular fracture [27-29]. Hydrogen generated from cathodic reaction can diffuse into the Mg alloys [30] and decrease the material's ductility after the rupture of the passive film on the Mg surface. Transgranular SCC shows a brittle cleavage-like morphology and it occurs more often for Mg alloys [31].

Experimental evidence has shown that the crack velocity of SCC mainly depends on the value of stress intensity factor, as presented in the Figure 2-4. It can be seen that there is a threshold stress intensity factor, K_{ISCC}, below which the crack growth rate is small enough to be neglected. Apparently, K_{ISCC} can be used for the structural design. When the stress intensity factor exceeds this critical value, the crack velocity quickly increases until a plateau region is reached, during which the crack velocity is K-independent. With the stress intensity factor further increasing, the crack velocity will again accelerate until failure. It should be noted that the last region is not necessarily observed for some magnesium alloys [25].

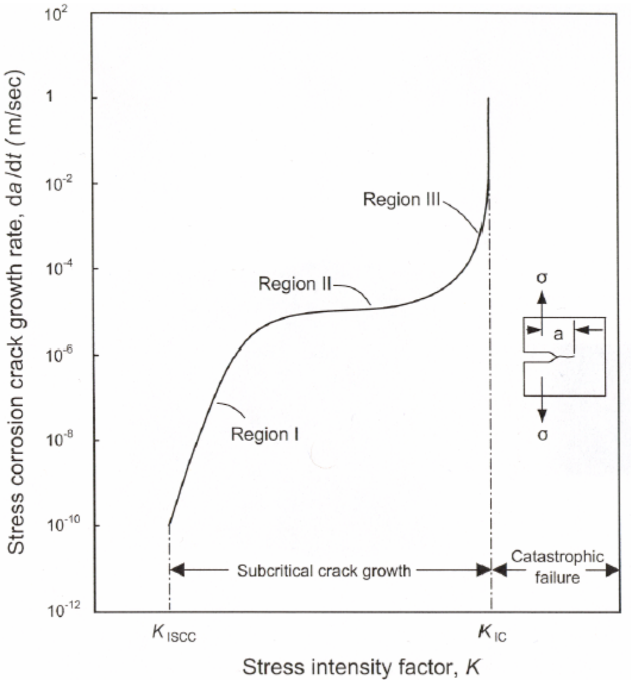

Figure 2-4 A schematic diagram of stress-corrosion crack growth rate, da/dt, as a function of stress intensity factor K [32].

2.2.3 Corrosion fatigue of Mg alloys

Compared to the pure corrosion problem, the inferior corrosion fatigue property is actually recognized as a bigger challenge to the extensive application of Mg alloys now [32]. Under the combined interactions of external chemical environment and cyclic loading, corrosion fatigue can lead to much unexpected cracking behavior and failures of engineering structures [33]. Compared with other metallic engineering materials, Mg alloys are far less studied for corrosion fatigue behavior but rather extensively studied for corrosion performances due to their high susceptibility to corrosion.

The fatigue life and fatigue strength of Mg alloys in corrosive environments are significantly reduced considering those in the air as a reference. A systematic corrosion fatigue study on magnesium alloys including die-cast AZ91D, AM50 and extruded AZ31, AM50, AZ80, ZK60 in NaCl-based solutions and a $Na_2B_4O_7$ solution saturated with $Mg(OH)_2$ was done by Eliezer et al. [34]. Results showed that the fatigue life of all the alloys was longer in air than that in NaCl-based solutions (Figure 2-5). Unigovski et al. [35] also carried out corrosion fatigue test on extruded AZ31, AM50, and ZK60 alloys in air, NaCl-based and borate solutions and obtained similar results.

The reasons for the reduced fatigue properties can be two folds. Take the fatigue life as an example. As the total fatigue life consists of fatigue crack initiation life and fatigue crack propagation life, the reduced fatigue life in a corrosive environment includes the reduced CFCI life and CFCP life. On one hand, in general, fatigue crack initiation of Mg alloys without corrosion attack at room temperature is related to slip at preferred orientations and the existence of micropores. However, when in aggressive environments, many papers reported that the fatigue initiation is closely related to the corrosion pits formed on the specimen surface. Nan [36] studied the corrosion fatigue behavior of AZ31 alloy in 3% NaCl solution and concluded that life in low stress region is determined by the corrosion pit grow behavior. Bhuiyan et al. [37] investigated the corrosion fatigue process of extruded AZ61 alloy under three different environments: 80% relative humidity, 5 wt% NaCl solution and 5wt% $CaCl_2$ solution. Their results suggested that NaCl environment enhances pit formation and growth more than $CaCl_2$ environment due to its high Cl^- concentration and low pH value. On the other hand, the reduced corrosion fatigue life can be also resulted from the accelerated fatigue crack propagation rate. The fatigue properties of Mg alloys may be deteriorated after the involvement of corrosion. Stephens et al [38] studied the fatigue behavior of Mg alloy AZ91 in both air and 3.5% NaCl environment and determined the material constants in the well-known fatigue crack propagation Paris' equation ($da/dN=C(\Delta K)^m$), as presented in Table 2-2. It can be easily deduced that the Mg alloy in the corrosive environment has a higher fatigue crack propagation rate. Other researchers [39-41] also reported the loss of ductility of Mg alloys in tensile tests and cleavage fracture surfaces after immersing specimens in an aqueous solution. That is to say, hydrogen is generated from the electrochemical reactions on the Mg surface during immersion and could diffuse into the specimen. The hydrogen embrittles the Mg alloy and hence assists the crack growth.

The improvement of corrosion resistance is beneficial to improve the fatigue life of Mg alloys in the aggressive environments. Wittke et al [42] reported that the fatigue strength of the alloy Mg-4Al-2Ba-2Ca in the NaCl environment can be greatly enhanced by decreasing its corrosion rate. Significant efforts have been spared to find a way to reduce the corrosion rate of Mg alloys.

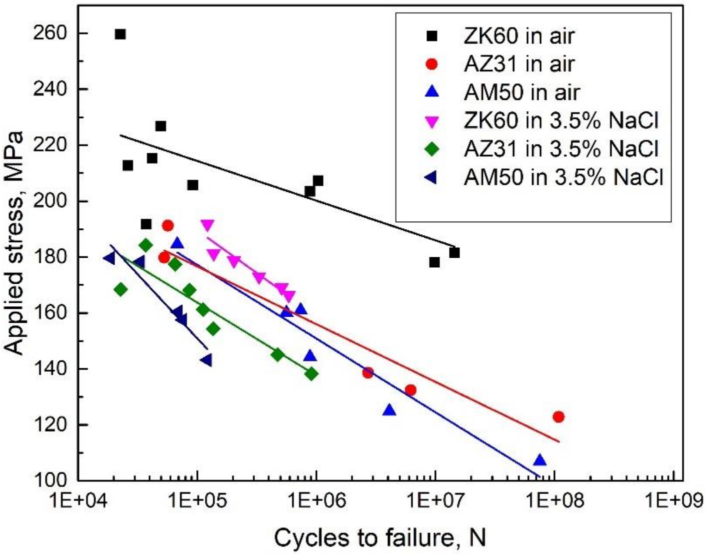

Figure 2-5 S-N curves of extruded ZK60, AM50, AZ31 alloys in air and 3.5% NaCl solution saturated with $Mg(OH)_2$ [34].

Table 2-2 Constant amplitude fatigue crack growth properties (Unit m: MPa • $\sqrt{m}$ and C: m/cycle) [38]

	Air environment	Corrosion environment
C (stress ratio R=0.05)	2.4×10^{-10}	5.2×10^{-10}
m (stress ratio R=0.05)	3.7	4.7
C (stress ratio R=0.5)	1.1×10^{-9}	2.2×10^{-10}
m (stress ratio R=0.5)	3.2	7.0

2.3 Corrosion protection strategies for Mg alloys

Materials in this section appeared in a journal paper by wang et al. [43]. A coating system is typically needed to achieve a class A (Class A in automotive industry refers to the glossy, smooth appearance that is required for readily visible, outer surfaces of automobiles) quality of surface finish on Mg parts, as shown in Figure 2-6 [44]. In the coating system, the first layer is the surface treatment (i.e. the chemical conversion coating or anodizing, etc.), aiming at removing the mill and pressing oils and improving corrosion resistance and paint adhesion property. The second layer, a precursor such as E-coat, is applied to further enhance corrosion resistance and to improve the ability against mechanical damage, followed by the final topcoat consisting of a base coat and a clear coat to ensure the stability of the coating system and provide cosmetic appearance. In this work, surface coatings consisting of only the first layer (chemical conversion coating or MAO) and the second layer (E-coat or powder coating), with no final topcoat (i.e. base coat + clear coat) were investigated.

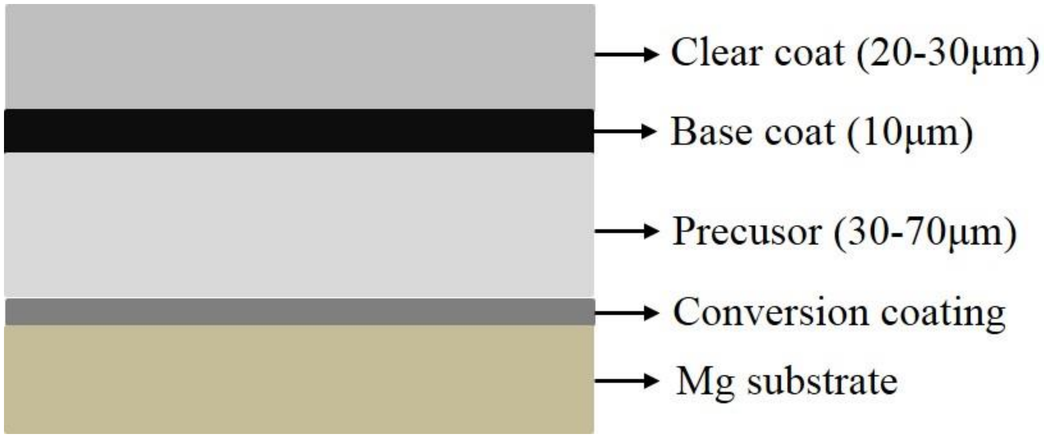

Figure 2-6 Typical coating system for surface finish of Mg die-castings in class A quality [44]

In most cases, prior to the application of the surface treatment, Mg components must go through a cleaning process and an activation process, as shown in Figure 2-7. The cleaning process includes mechanical cleaning methods (e.g. grinding, polishing) and chemical cleaning approaches (e.g. alkaline degreasing, organic solvent cleaning), which together macroscopically and microscopically remove most of the oils, lubricants, dirt, oxide or hydroxide layers arising from previous manufacturing or forming processes respectively. Then, the activation process (usually an acidic pickling for Mg alloys) is used to further provide a homogenous and oxide free Mg surface for the subsequent surface treatment. Detailed information regarding surface preparation prior to coating has been described by Höche, D., etc. [45] and standard procedures to prepare the Mg alloy surfaces can be found from Standard ATSM D 2651 and the International Magnesium Association.

Figure 2-7 Schematic procedure of surface processing

As for the surface coating, various methods have been developed for Mg alloys. Based on the data from web of science using corresponding key words such as “surface coating AND magnesium”, the number of publications for different surface coatings since 1990 have been illustrated in Figure 2-8. It appears that anodizing & micro-arc oxidation (MAO), chemical conversion coating, and chemical vapor deposition attract considerable researcher attention. Further, ion implantation, organic coating, and plating (include electroless plating and electrochemical plating) account for a large portion of those publications as well. In addition, according to a review on corrosion protection of Mg alloys based on patents [46], chemical conversion coating, anodizing, plating, and organic coating were represented as the most widely used methods to improve the corrosion resistance of Mg alloys. Therefore, the emphasis of the next section will be placed on these four types of coatings and their applications in automotive. Other processes like the vapor-based deposition, and some emerging techniques such as cold spray will also be briefly introduced.

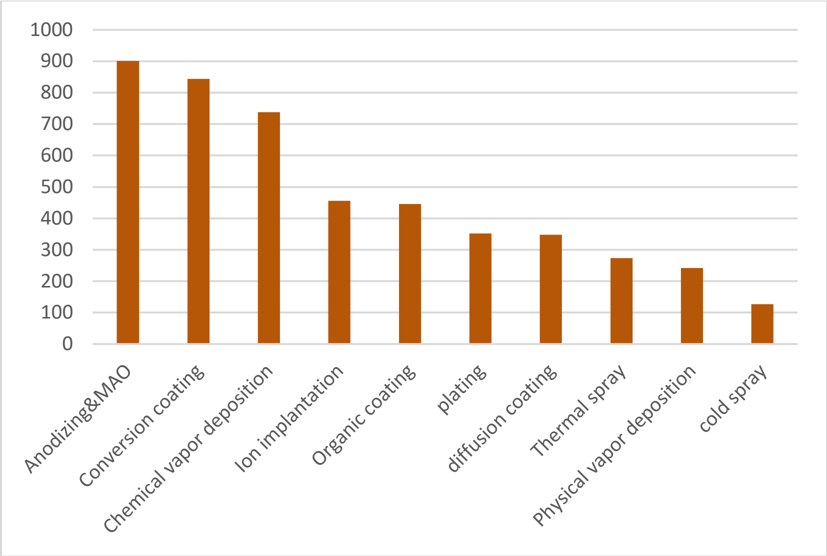

Figure 2-8 Number of publications of different surface coatings on Mg alloys since 1990

2.3.1 Chemical conversion coating

Chemical conversion coating is one of the most widely adopted surface treatments in industries due to its low cost, good corrosion resistance and simple operation procedures [47]. By simply immersing the substrate into a conversion bath, an adherent, insoluble, crystalline or amorphous layer can be produced to provide corrosion resistance and good paint adhesion to Mg alloys. The most common conversion coating used on Mg alloys in automotive industry had been a chromate treatment (e.g. dichromate, chrome manganese, the chrome pickle) [48]. Cr-based conversion coatings could provide high levels of corrosion protection, abrasive resistance, good paint adhesion and self-healing capability, but nowadays their use is strongly limited because of the main drawback represented by the toxicity issue. Therefore, a number of non-chromate chemical conversion coatings have been developed to substitute the Cr-based conversion coating; for instance, phosphate based coating [49-51], stannate coating [53], fluorozincate/fluorotitanate coating[54-55], Ti/Zr coating [56] and rare earth coating [57-58]. A comparison of these chemical conversion coatings is presented in Table 2-3. Among them, phosphate based coatings (mainly Mn-P and Zn-P), fluoride based coatings (F/Ti, F/Zr), and Ti-Zr coatings seem to be the most promising options in automotive industry, which can be demonstrated through some commercial products as presented in Table 2-4. All of them are chrome-free, environmentally friendly, and can provide excellent paint adhesion and corrosion protection.

At present, one of the most widely used pretreatments in automotive industries is Zn phosphating, as reviewed in Ref. [59]. Since this phosphate solution is acidic (pH=3.0-3.5), Mg parts will be highly dissolved when entering the bath. Moreover, in contrast to an alkaline cleaning process for steel and Al components, Mg alloys require an acidic cleaning. Thus, the current way to address this issue is separately treating single Mg pieces before they are assembled to the vehicle. From Table 2-3, phosphate based coatings (mainly Mn-P), conversion coatings based on Ti-, Zr or Ti/Zr seem to be the most promising options for Mg parts in automotive industry, which can be demonstrated from the current commercial products as presented in Table 2-4. The conversion coatings based on Ti-, Zr or Ti/Zr are relatively new and are developed to replace phosphate-based coatings. Because in addition to cause some environmental problems such as eutrophication in lakes, phosphate baths can generate massive sludge containing metal ions. These problems are solved now by conversion coatings based on Ti-, Zr or Ti/Zr due to the use of free of phosphate compound baths with a tiny amount of ionic species [60][61]. At this time, these conversion coating are already commercialized in the surface treatment of Al alloys and some steels, but there is only a few data with respect to Mg alloys [61][62].

As for the conversion coatings applied to corrosion protection of Mg automotive components, it has been reported that a conversion coating with brand name Henkel Alodine 5200 was used to protect the Mg instrument panel from pitting on the sport car 2005 Ford GT [63]. The corrosion protection of Mg lifegate on the 2010 Lincoln MKT also included the Alodine 5200 sub-micron thick chemical conversion coating [64]. A Cr-free conversion coating based on Ti/Zr has been used on the Mg doors of the Ford Contour vehicle [64]. Another example used the combination of MagPass-Coat and a 200 μm polyester powder coating to protect the inlet pipe of the Audi W 12 Mg (AZ91) cylinder engine [65]. Also, Meridian Technologies applied a conversion coating base on chrome-free patented fluorozincates and fluorotitanates to a front end carrier [64]. Additionally, in a Canada-China-USA collaborative R&D project aiming at developing comprehensive application technology suitable for Mg alloy in the front end where corrosion is a major concern, researchers from Institute of Metal Research (IMR) developed an environmentally friendly and corrosion resistant conversion coating from a Mn-based phosphate bath [66]. This coating has the characteristics of simple process, long life of bath solution, low cost and high bonding strength to the car body. Moreover, this coating has attained industrialization level and has already been used in the Mg alloy hood shield by FAW, as shown in Figure 2-9.

Table 2-3 Summary of mechanism of coating process, advantages and disadvantages for each conversion coating [47, 49-50, 52-54, 67-69]

Coating	Mechanism of coating process	Advantages	Disadvantages
Chromate coating	The substrate is oxidized by oxidizing agent $Cr_2O_7^{2-}$, which causes an increase in pH at the liquid-alloy interface. Thus, soluble hexagonal Cr^{6+} is reduced to insoluble Cr_2O_3 deposited on the Mg surface. A self-healing ability is given by trapping hexagonal Cr into the coating.	Excellent corrosion resistance; good abrasion resistance; self-healing capability and mature process	High toxicity due to hexagonal Cr; Instable at high temperature (>60℃)

Phosphate coating	Oxidizing agent and acidified phosphate solution (PO_4^{3-}) in the conversion solution cause the dissolution of the substrate, resulting in a rise in pH and metal ions concentration, thus leading to the precipitation of insoluble metal phosphate on the Mg alloys surface.	Environmentally friendly; comparable corrosion resistance to chromate coating; good adhesive property	Network cracks
Stannate coating	Oxidization of the Mg substrate favors the nucleation and growth of hemispherical magnesium stannate particles ($MgSnO_3$) initially at the cathodic sites and then to the whole surface, with a porous under-layer made of magnesium hydroxide.	Environmentally acceptable; good corrosion resistance	Long time and high temperature treatment; thin coating (1-5 μm).
Fluoride-based coating	The acidic fluoride solution (F^-) oxidizes the metallic substrate to form a porous $Mg(OH)_2$ layer and simultaneously F ions are incorporated into this layer by substituting the OH^- or by forming insoluble MgF_2.	Reasonable corrosion resistance; good adhesive property	Long time treatment and large consumption of HF.
Rare earth coating	The acidic rare earth salts solution (Ce^{3+}/Ce^{4+} or La^{3+}) firstly dissolves the air-formed oxide film and the substrate, leading to a rise in local pH , then followed by a precipitation of rare earth hydroxide or oxide on the porous layer containing $Mg(OH)_2/Al(OH)_3$.	Excellent corrosion resistance; environmentally friendly	Long time treatment, Increased instability of the coating with time elapsing and expensive.

Figure 2-9 IMR phosphate conversion coating used on Mg alloy hood shield by FAW [66]

Table 2-4 Commercial conversion coatings on Mg alloys

Coating	Manufacturer	Characteristics and applications
Alodine 5200 [70]	Henkel	A chrome-free passivation specifically formulated for treating Al, Mg, Ti alloys. It provides excellent base for bonding of adhesives and organic coating and can be applied by spray or immersion
Magpass-Coat[71]	AHC Oberflachentechnik	A chrome-free conversion coating suitable for all Mg-based material. It is electrically conductive and withstands high temperature exposure (No effect subjected to 90ºC for 6 months)
Gardobond X4729[72]	Chemetall	A chrome-free, eco-friendly conversion composite coating based on zirconium and titanium for Al and Mg alloys. It offers excellent paint adhesion and corrosion protection. It is an easy-to-handle and low-maintenance process.
Oxsilane 0611[73]	Chemetall	It is used as stand-alone protection or paint pretreatment and used only in aerospace and military industries
Metalast TCP-HF[74]	Chemeon surface technology	It is a trivalent chromium conversion coating as well as a sealer for anodized Al, Mg and Zn alloys. It offers excellent paint adhesion and corrosion protection.
Surtec 650[75]	SurTec	A chromate-free passivation for Mg and Al alloys. Can be used as post treatment of anodic coating and can be applied by spray, immersion and wipe application

Interlox 5707[76]	Atotech	Zr-based coating. Free of P, Cr, Zn, Ni and Co. It can operate at room temperature and produces little to no sludge. It allows for automated control and can be used for multi-materials.
Zircobond 4200[77]	PPG	Zr-based coating. It is designed to replace Zinc-phosphate pretreatment. The process can be installed into existing lines without changing the process flow.

Chemical conversion coating has the ability to prevent Mg dissolution in the subsequent organic coating or top coating process and also can protect the Mg components during transport and storage. However, the corrosion protection provided by this type of coating is very limited because chemical conversion coating is generally too thin and too weak, making it easily damaged during assembly. For example, the thickness of Magpass-Coat is typically less than 1μm [71]. Besides, the quality of the surface treatment is very sensitive to the previous cleaning process, activation process, and conversion bath parameters such as pH, immersion time or temperature. Additionally, it is difficult to produce a conversion coating which is defect-free and uniform. Therefore, there remains a strong demand for developing more robust, chromate-free conversion coatings, especially involving self-healing capability.

2.3.2 Anodizing coating

Anodizing is a widely used strategy to produce a thick, hard, stable and ceramic-like coating which can offer excellent corrosion protection on Mg parts [78]. The anodizing coating usually has a porous morphology and a cellular structure as shown in Figure 2-10, through which corrosive species can penetrate into the Mg substrate. Thus, it is very necessary to seal the anodized film to achieve enough corrosion resistance. The porous nature of anodizing makes it an excellent paint base in the vehicle coating line, and cosmetic finish can also be obtained. In addition, the anodizing layer can provide excellent wear resistance, which therefore makes Mg components less likely to be damaged during assembly than conversion coating. Essentially, anodizing is an oxidation reaction in the aqueous solution which can be technically accomplished by two different conditions: voltage controlled or current controlled. Different voltage or current regions result in different coating formation processes such as sparking, micro-arcing anodizing at high voltages. Conventional commercial anodizing treatments using relatively low voltage such as DOW 17 and HAE [71] can provide superior anticorrosion property on Mg alloys, but their anodizing baths include chromates and/or HF and thus they are now restricted to industry use. New anodizing processes called micro-arc oxidation (MAO) or plasma electrolytic oxidation (PEO) [79], which are much less hazardous, have been developed for Mg alloys. MAO employs higher voltage than conventional anodizing such that micro discharges occur, and the resulting plasma modifies the surface structure of Mg alloys. This MAO process can produce thicker layer with higher corrosion and abrasion resistance as well as improved temperature and load capacity compared with the DOW 17 and HAE heat process.

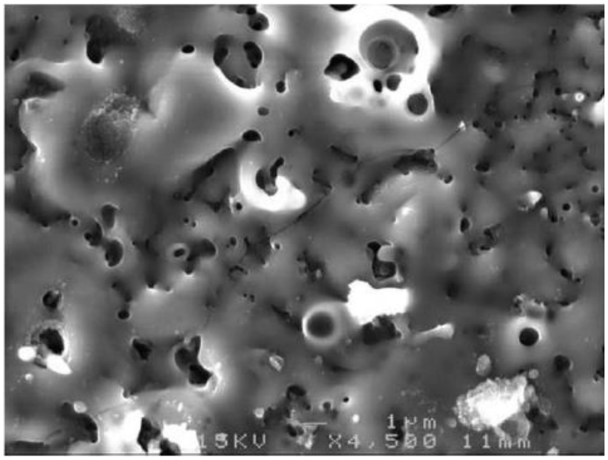

Figure 2-10 A typical microstructure of an anodizing coating formed on AZ91D in a silicate-containing solution [80]

At present, anodizing has been successfully used in the Al alloys for many years. However, it is more complicated when this technique is applied to magnesium alloys. For example, it requires much higher voltage to anodize Mg alloys than Al alloys. Besides, the microstructure of the anodizing coating formed on Mg alloys is irregularly porous whereas it is regular for Al alloys. Some industrial anodizing processes developed for Mg alloys are summarized in Table 4. These commercial anodizing films have already been applied in Mg automotive components such as gearbox housing, wheel rim, engine blocks, door inners, suspension parts, intake manifolds, cradles, pistons, etc. An example of Tagnite coating in protection of a Mg oil pump housing is shown in Figure 2-11[81]. Also, in a case of a hybrid-electric Ford Focus, an Al part used to house the power distribution unit was replaced by a Mg one, in which the Mg surface was protected with a Tagnite anodizing coat [64].

There is no question that the anodizing coating can offer a better corrosion resistance, wear resistance and paint adhesion property than conversion coatings. However, anodizing coatings suffer some challenges. For example, the electrochemical inhomogeneity due to the phase separation in magnesium alloys makes it difficult to produce an adherent and uniform coating. Besides, the fatigue strength of magnesium alloys modified by this surface treatment is evidently decreased. Furthermore, anodizing has environmental issues and is more expensive due to the large consumption of electricity.

Table 2-5 Some industrial anodizing process developed for magnesium alloys [80, 82, 83]

Anodizing process	Manufacturer	Description	Characteristics	SST Hours
DOW 17	Dow chemical	The first anodizing coating for magnesium alloys; produced at voltage below 100V in a solution containing dichromate, ammonium acid fluoride and phosphoric acid at pH 5 above 70 °F.	The coating thickness ranges from 5μm to 75μm; the color varies between light and dark green depending on coating thickness; the composition mainly consists of MgF_2, $NaMgF_3$, $Mg_{x+y/2}O_x(OH)_y$ and a small amount of Cr_2O_3.	48
HAE	Pitman-Dunn Laboratories	The electrolyte contains potassium permanganate, potassium fluoride, trisodium phosphate, potassium hydroxide and aluminum hydroxide; applied with alternative current and voltage below 125V at pH 14 and a temperature between 20-30℃.	The coating thickness ranges from 5μm to 75μm; the color varies between light tan and dark brown depending on coating thickness.	48
Anomag	Magnesium Technology Ltd	It is a non-sparking process; the anodizing bath contains ammonia, sodium ammonium phosphate, without chromate and fluoride.	The thickness varies from 5μm to 25μm; a wide range of colors can be obtained.	300
Magoxid	AHC Oberflache-ntechnic	Obtained in a solution containing borate or sulfate, phosphate and fluoride or chloride at pH 5-11 buffed by amines at a DC current preferably with a voltage up to 400V.	The thickness varies from 15μm to 25μm; the color of the coating normally varies between white to light gray, sometimes black can be obtained; the coating mainly contains MgO, $Mg(OH)_2$, MgF_2, $MgAl_2O_4$.	500
Tagnite	Technology Application Group	Produced in an alkaline aqueous solution containing hydroxide, fluoride and silicate species with no chromium or other heavy metals; operated at voltages exceeding 300V DC and a temperature between 4-15℃.	The thickness ranges from 2.5μm to 22.5μm; the coating is white and mainly consists of hard magnesium oxide with minor hard fused silicates.	400
Keronite	Keronite	Performed with a bipolar pulsed electrical current using a specific wave form in a proprietary, chrome and ammonia-free, low concentration alkaline electrolyte at a temperature between 20 ℃ and 50℃.	The thickness ranges from 20 to 80μm; the layer is mainly composed of spinel ($MgAl_2O_4$) together with SiO_2 and SiP.	600
MgC	Henkel	Plasma electrolytic ceramic deposition process using pretreatment tanks; no information available on operation conditions.	Coating thickness ranges from 2-6μm; Ceramic black coating comprised of Mg compounds.	200-500
Alodine EC2[53]	Henkel	Operated at voltage ranges from 300-450V for time duration of 1-5 minutes and a temperature of 15-50℃.	Coating thickness ranges from 2-15 μm; Electro-ceramic coating comprised of Ti dioxide; compatible with most typical paint finishes and liquid paint systems; fewer steps, faster process and reduced processing costs compared to traditional methods.	N/A

Figure 2-11 Mg oil pump housing with Tagnite coating: Tagnite with paint (left); Tagnite alone (right) [81]

2.3.3 Electrochemical plating

Apart from chemical conversion coating and anodizing, electrochemical plating has achieved commercial importance on Mg alloys not only because of the improved corrosion and wear resistance but also the metallic coatings deposited on Mg part surfaces offer beautiful appearance, good solderability, electrical and thermal conductivity. Electrochemical plating is a reduction process, in which the dissolved metal ions in the bath are reduced to their metallic form and deposited on the surface of the part. Unfortunately, high chemical activity makes plating of Mg alloys very difficult. Only Ni and Zn can be directly electroplated on Mg alloys. A suitable undercoating pretreatment is necessary to prevent the Mg surface from oxidation. At present, zinc immersion and direct electroless nickel plating are widely used pretreatments in Mg alloys [67, 84-85].

Electrochemical plating is generally classified as either electroplating process [85] or electroless plating process [86] depending on the different driving forces for the reduction process. An external force such as voltage is necessary for an electroplating process and a chemical reducing agent for an electroless plating process. As with the electroplating, different metallic coatings such as Ni, Zn, Cr, Cu, Ag, and Au have been applied to Mg alloys according to specific applications. For example, Cu is always used as a base layer to ensure good adhesion in multiple-plate electroplating; Ni is used to improve the corrosion resistance; Ag is used for anti-fretting purposes; and both Ag and Au are sometimes used to provide electrical conductivity and optical reflectance. Instead of a single metallic layer, multilayered metal coatings are commonly used on Mg components. Cu/Ni/Cr coatings are conventionally applied to some indoor and mild outdoor Mg components in automotive applications. For example, a Cu/Ni/Cr coating with Zn immersion pretreatment was reported to be used in the Mg interior panel of Porsche Cayenne [85]. Some other examples of plated Mg components in automotive industry have also been presented in Figure 2-12 [86]. Another multilayered

Ni/Au coating for Mg alloys is mainly utilized in the aerospace field. As for the electroless plating, Ni-P is the most common process. By immersing the parts into an aqueous solution, a uniform thickness film can be produced on even an irregular surface. Generally, due to limited corrosion protection, electroless Ni-P plating after sealing tends to be applied in mild industries such as computer and electronic (3C) industries [67].

Nevertheless, electrochemical plating still has some challenges in the application of Mg alloys. Besides magnesium's high susceptibility to corrosion, the intermetallic compounds, such as Mg_xAl_y, distribute along grain boundaries, making it especially difficult to uniformly plate magnesium alloys. Moreover, that different Mg alloys require different pretreatments makes the plating process more complicated. Additionally, as the noble metallic coatings have a big electrochemical potential with respect to Mg alloy, galvanic corrosion can easily occur if the plating has pores. Other problems such as the large consumption of electricity and difficulty in coating complex shapes in electroplating and, for electroless plating the short bath life, also limit their application.

Figure 2-12 Examples of plated Mg components: (a) Top cover of Mg alloy AZ91D engine using direct electroless Ni-P plating followed by Cu/Ni/Cr plating (b) Back cover of Mg alloy AZ91D engine using Zn immersion followed by Cu/Ni/Cr plating (c) Motorcycle wheel hub of Mg alloy AM60 using Zn immersion followed by Ni plating and Cu/Ni/Cr electroplating (d) Interior panel of Porsche Cayenne using Zn immersion followed by Cu/Ni/Cr plating [86]

2.3.4 Organic coating

Organic coating, which plays a significant role in improving corrosion resistance, wear property and decoration, is commonly used as a topcoat in a normal coating system for Mg alloys [67]. Resin (e.g. epoxy, vinyl, acrylic polyurethane) is the main composition of an organic coating. A typical organic coating is composed of a binder, pigments, and additives such as dryers, stabilizing agents, corrosion inhibitors. Prior to organic coating, an appropriate surface preparation is critical because of poor adhesion strength. Not only does organic coating require the surfaces of Mg alloys to be free of contaminants, smut and oxides, but the water and air in the defects must be removed as well. From Hu's review [87] on the progress of organic coating for Mg alloys, organic coatings can be formed by several techniques such as painting, powder coating, electrophoretic coating (E-coating), sol-gel coating and plasma polymerization. Table 2-6 summarizes a description of these techniques and their corresponding advantages and disadvantages.

Table 2-6 Summary of formation process description, advantages and disadvantages for each organic coating [87]

Organic coating	Description	Advantages	Disadvantages
Painting	Paint typically consists of resin, solvent, pigment and additives. One of the most important steps to paint magnesium alloys is to choose an alkali-resistant primer (resin) such as acrylic, polyvinyl butyral, polyurethane, vinly epoxy or baked phenolic. The painting film is usually formed by evaporation of the solvent or by some chemical reactions.	Flexibility; little restriction on the shape of substrate.	Use organic solvent; multistep
Powder coating	The thermoplastic powders are deposited by techniques such as electrostatic powder spraying or flame spraying to the Mg substrate and then heated to fuse the polymer together in a uniform, pinhole-free film.	Use no solvents, environment friendly; low hazards of flammability/toxicity and energy consumption; obtained in a single operation; almost 100% powder utilization	The powder stored in pulverized form requiring very dry; difficulty in obtaining thin coating; difficult to coat recessed areas; high process temperature
E-coating	The electrophoretic coating (E-coating) is obtained by a precipitation of charged particles in a liquid on the charged substrate surface under an electric field.	Short formation time; high coating material utilization; automatic processing; simple apparatus; even coating thickness; no requirement for binder burnout	Complicated electrical control and bath solution maintenance; roughness of substrate obvious
Sol-gel coating	The formation of a sol-gel coating is accomplished through gelation of a colloidal suspension which involves hydrolysis, condensation polymerization of monomers to form particles, followed by agglomeration of the polymer structures and a heat treatment.	Process temperature is low; being possible to form coatings on complex shapes and to produce thin films; waste-free and excludes the stage of washing	Lengthy process flow; phase separation during curing; limited thickness; crackability due to stresses developing during drying and thermal treatment

Currently, powder coating and E-coating are the two most popular organic coatings used in the corrosion protection of Mg components in the automotive industry [88]. Powder coating has been reported as the best top coating for corrosion protection of Mg alloys because it provides better general and galvanic corrosion resistance than E-coating [88]. Conversely, other researchers argue that E-coating of Mg has more advantages than powder coating, such as lower cost, no line-of-sight limitations, and the capability of coating complex parts [89]. Some commercially available products for powder coating (e.g. from ProTech, Akzo/Interpon and DuPont) and for E-coating (e.g. from PPG, BASF, and DuPont) have both been reported to be used in protection of Mg automotive parts [90]. For instance, the Mg instrumental panel of the sport car 2005 Ford GT was first pretreated by Henkel Alodine 5200 conversion coating, then followed by a Protech epoxy urethane powder coating [64]. Figure 2-13 also shows an application example of powder coating in certain Mg engine parts [91].

Figure 2-13 Mg engine parts using powder coating which shows perfect appearance and excellent protection [91]

Similar to other coatings, some challenges also appear in the deposition of organic coating on Mg alloys. First, a uniform, defect-free organic coating is difficult to be produced on Mg surface without careful surface preparations. Even so, an additional layer of polymer or other powder coating on top of that is still necessary. Thus, it is necessary to apply multiple layers of these coatings to achieve sufficient corrosion performance. Besides, there are still some environmental issues because of the used solvent in these coating processes.

2.3.5 Other process

Other surface technologies such as layered double hydroxides (LDHs), cold spray, thermal spray, physical vapor deposition (PVD), chemical vapor deposition (CVD), and laser surface coating have been also applied to improve the corrosion resistance of Mg alloys [48, 67, 92], but few of them achieved commercial applications in automotive industry. LDHs with a tunable brucite structure are essentially a class of anionic clays (e.g, NO_3–, PO_4^{3-}, CO_3^{2-} [93-97]. Their unique layered structures regarded as nano-canpsules are capable of storing and releasing corrosion inhibitors, which allow researchers to develop more functional coatings. Besides, LDHs can be used to replace the conventional sealing strategies to seal the anodized film. However, so far this surface technology is mainly developed for medical application, more research is needed to extend their application. Cold spray is an emerging technique to coat and repair a wide range of industrial components [98-99]. It was initially aimed towards the aerospace industry because it can provide much harder, thicker coatings compared to other available coatings. However, with this technology moving forward, there is a high potential of its commercialization in the automotive industry. The conventional thermal spray processes such as flame spraying, arc spraying, and plasma spraying requires heating sprayed particles into molten metal droplets. In contrast, cold spray is a process of applying coatings by exposing the substrate to a high velocity (300-1200m/s) powder particles which are accelerated by a supersonic jet of compressed gas such nitrogen, helium, air or a mixture of them at a temperature well below the melting temperature of the material, i.e. forming coatings from particles in the solid state. In this way, it mitigates or even eliminates the deleterious effects of high temperature oxidation, phase transformation, residual stresses, porosity and other problems resulting from the thermal spray approaches [100]. The plastic behavior of both particle materials and the substrate is closely related to the formation of the cold sprayed coating. When high velocity particles impact with the substrate, severe plastic deformation of the particles occurs. At the same time, significant penning effect due to the impact of particles on substrate surface induces deformation of the substrate. Consequently, the interfacial deformation and localized heat between sprayed particles and the substrate contributes to forming a good adhesive coating by mechanical interlocking and metallurgical bonding. It is recommended that the material with more plastic than the substrate should be used.

To date, pure Al, aluminum alloys, aluminum alloys blended with Al_2O_3 have been used to coat various Mg alloys by cold spray technique [101-104]. Result shows that cold sprayed coatings can significantly improve the corrosion resistance of Mg alloys, which show their promising application in corrosion protection of magnesium alloys. However, as an emerging technique, cold spray is still mainly in research and development stage, more coating performance data needs to be collected.

2.4 Literature review on modeling of corrosion fatigue life

Corrosion fatigue has become one of the most important engineering research area since the observations of damage in the Royal Navy's paravane towing cables during World War I [32]. The synergistic effect of the corrosive environment and cyclic loading can lead to early fatigue crack initiation and enhanced fatigue crack growth rates and thus early failure of structures and components. It is important to understand the essence of the interaction of material-loading-environment system so that an appropriate damage design could be achieved to meet the practical in-service requirements. It is well known that a corrosion fatigue process can be split into two stages: crack initiation and crack propagation, and so is the modeling of corrosion fatigue life.

2.4.1 Modeling of Corrosion fatigue crack initiation (CFCI) life

The influence of corrosion on crack initiation is generally more than on crack propagation. Corrosion pits are considered as the nucleation sites of fatigue crack. Acting as geometrical discontinuities, corrosion pits can cause stress concentration and eventually lead to an earlier crack initiation [105]. To model the pitting-induced CFCI life, problems such as the evolution of pit size, pit-to-crack transition, etc. have to be addressed to characterize the corrosion fatigue initiation process.

2.4.1.1 The evolution of pit size

It can be clearly seen from Figure 2-14 that how the corrosion pit evolves and the crack initiates and propagates from corrosion pit [106]. A small corrosion pit first initiated from a weak section in the matrix

(Figure 2-14 (a)) and quickly grew up to a critical pit with larger depth and length (Figure 2-14 (b)). Then, under the combined effect of corrosion environment and stress conditions, some secondary pits were formed at the bottom of the first pit, which further increased the extent of stress concentration. Consequently, the crack readily developed from the bottom or the mouth of the pit (Figure 2-14(c)(d)). After the crack nucleated from the pit, it started with a stage of small crack propagation (Figure 2-14(e) (f)), followed by a long crack propagation (Figure 2-14(g)) when the crack reached a critical length. For predicting the CFCI life, it is necessary to make the quantitative evaluation of pitting growth behavior. To date, extensive studies have been conducted on the pit size development and some models have been proposed to predict the evolving pit. The models developed by some researchers [107] [108]suggested that the pit growth was taken to be only controlled by corrosion and elapsed time, giving a similar power law curve ($a = \alpha t^{B}$, where a represents pit depth, α and B are experimentally determined constants). Kondo [109] proposed a deterministic model based on two different low-alloy steel to predict the corrosion pit size with taking into account the effect of cyclic stress in the pitting corrosion process. It was found that the effect of stress on pit growth rate was prone to be evident at high stress levels. The aspect ratio used to define the shape of the pit (defined as the ratio of pit radius (c) to pit depth (a)) remained constant during pit development. Corrosion pit growth could be formulated as $2c \propto t^{1/3}$. Ishihara [110] studied the effect of stress amplitude and stress cyclic frequency on the corrosion pit growth behavior using aluminum alloys 2024-T3 and found that the corrosion pit depth (μm) can be expressed by the equation of $a = 2.34 \times 1.014^{\sigma_a} t^{B}$.

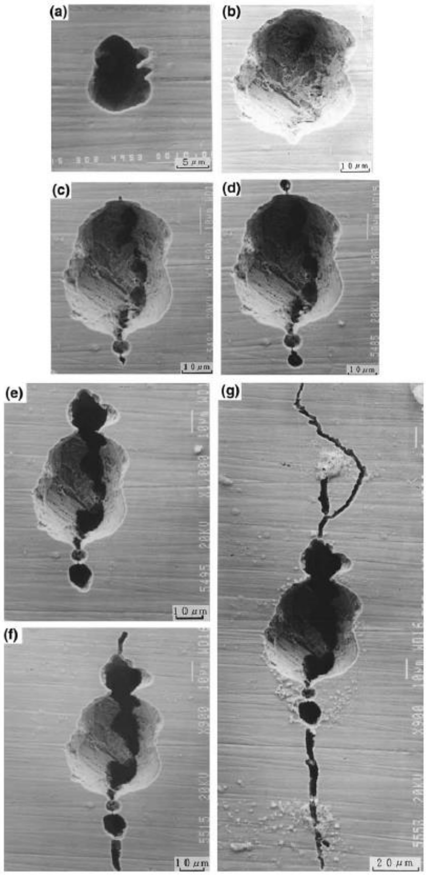

Figure 2-14 Corrosion fatigue crack initiation and propagation process in association with corrosion pit, 228 MPa, 3% NaCl aqueous solution (318 K): (a) 4.95×10^6, (b) 5.45 ×10^6, (c) 5.48×10^6, (d) 5.485×10^6, (e) 5.495×10^6, (f) 5.515×10^6 and (g) 5.55×10^6 cycles [106]

Further, based on Kondo's model, Harlow and Wei [112] proposed a model using Faraday's law by assuming a hemispherical pit growing at constant volumetric rate from initial pit radius a_0. The pit growth rate (with volume $2\pi a^3/3$) could be given as follows:

$$\frac{dV}{dt} = 2\pi a^2 \frac{da}{dt} = \frac{MI_P}{nF\rho} = \frac{MI_{P0}}{nF\rho} exp\,(-\frac{\Delta H}{RT}) \qquad 2\text{-}6$$

By a simple integration of equation (2-6) to be given by:

$$t = \frac{2\pi nF\rho}{3MI_{p0}}(a^3 - a_0^3)exp\,(\frac{\Delta H}{RT}) \qquad 2\text{-}7$$

Where the pitting current I_p in equation (2-6) normally refers to the galvanic current that is generated between the intermetallic compounds and matrix of the alloy. It can be expressed in terms of the pitting current coefficient I_{p0}, the activation energy ΔH of the base alloy, and the temperature T in which the process takes place according to the Arrhenius law [111]. a is the pit radius at time t, M is the molecular weight of the metal, F is Faraday constant and ρ is the density of the metal, and R is the universal gas constant. Then, Sriraman and Mao, etc. [113] [114] made some modifications on the base of the Wei's model, such as by considering the shape of pit to be semi-ellipsoidal and incorporating the effect of stress into pit corrosion fatigue process by inferring the result of the Ishihara's model. The pit growth behavior can be expressed as:

$$c = \left(\frac{3C_p}{2\pi\lambda^2}\right)^{1/3} t^{1/3}\, C^{\sigma_a} \qquad \text{2-8}$$

Where $C_p = \frac{MI_{P0}}{nF\rho} \exp\left(-\frac{\Delta H}{RT}\right)$, λ is the aspect ratio, C is a constant and σ_a is the stress amplitude. In this research, the Sriraman's model was adopted to determine the CFCI life. The critical problem is the determination of the critical pit depth above which the crack would start to initiate.

2.4.1.2 Pit-to-crack transition

Based on above knowledge, it is known that pit-to-crack transition was one of the most important issues in the prediction of CFCI life. Likewise, several mechanisms and corresponding models have been proposed to explain the pit-to-crack transition. One of them is based on fracture mechanics [110-115]. A pit is usually considered to be an equivalent surface crack in this model. It is deemed that there is a critical pit size in which the local mechanical condition is exactly met for the onset of crack growth. That is when the stress intensity factor of the pit reaches the threshold stress intensity factor of fatigue crack propagation ($(\Delta K)_{pit} \geqq (\Delta K)_{th}$). On the other hand, Kondo [105] believed that whether fatigue crack initiates depends on the relationship between the crack growth rate and pit growth rate. Only when the crack growth rate exceeds the pit growth rate the crack begins to initiate ($(dc/dt)_{crack} \geqq (da/dt)_{pit}$). The models based on fracture mechanics may be useful in practical application but in short of elaborating the interaction of pitting evolution and fatigue. Another mechanism is based on continuum damage mechanics (CDM) [116][117], in which the pit was assumed to be a notch. In this model, the pit-to-crack transition condition was similar to the critical pit size model. The difference is that the fatigue crack initiation is considered to be determined by the stress distributed over a finite volume ahead of the pit named as a process zone rather than by the maximum stress around the pit. Therefore, the fatigue notch sensitivity factor (K_f) was used to replace stress concentration factor (K_t) to calculate the pit-to-crack transition condition. Although the models based on CDM have edges in accounting for the synergistic effect of corrosion and fatigue, there are too many parameters and the model process was far from complex.

In this research, a theory based on Neuber's rule [118] is attempted to analyze the pit-to-crack transition process. By assuming the pit to be a notch at the transition point, corrosion fatigue crack will be initiated at the bottom of the pit when maximum applied strength exceeds the theoretical material strength.

$$K_t S \geq \sqrt{E\sigma_e\varepsilon_e} \qquad \text{2-9}$$

Where K_t is the stress concentration factor, which is a function of the geometry of the pit. S is the applied stress. E is Young' modulus. σ_e is the fracture strength and ε_e is the ductility. The critical pit depth can be determined from the stress concentration factor at the pit-to-crack transition point.

Fatigue crack would readily nucleate from the pit with maximum stress concentration factor [119]. Pidaparti, et al. [120] studied the stress distribution around corrosion pits using finite element analysis and found that the stress was firstly increased by 80% within 30 min corrosion and then the increment of stress just changed about 6% from 30 min to 60 min corrosion and finally reach a plateau. Cerit [121] also investigated the stress concentration of corrosion pit with assumption of the pit being semi-elliptical based on the finite element analysis. It was concluded that the aspect ratio of corrosion pit was an important factor deciding stress concentration factor value and could be estimated by an empirical equation as follows:

$$K_t = \frac{1+6.6\lambda}{1+2\lambda} \quad 2\text{-}10$$

Where λ is the aspect ratio of corrosion pit. According to the finite element analysis, the maximum stress should appear at the bottom or slightly below the mouth of corrosion pit. Cerit [121] further studied the effect of secondary pit formed at the primary pit on stress concentration. It was found that the stress distribution was completely changed and the overall stress concentration was much larger than that of a single primary pit. Based on Cerit's work, Zhao et al. [122] emphasized their study on the quantitative measurement of stress concentration having a secondary pit formed at the bottom of a primary pit. By considering these two pits separately as a single pit, the stress concentration of the compound pit was estimated by:

$$K_t = K_{t1} \times K_{t2}^{0.95} \quad 2\text{-}11$$

Where K_{t1} is stress concentration factor of the primary pit and K_{t2} is stress concentration of the secondary pit

2.4.2 Modeling of corrosion fatigue crack propagation (CFCP) life

Modeling of corrosion fatigue crack propagation becomes more complex due to the synergistic effect of aggressive environment and cyclic loading compared to that of pure fatigue. To date, there are three major corrosion fatigue models and their extended versions reported in literature:

2.4.2.1 Superposition model

The superposition model was first developed by Wei et al. [123-125] who suggested that the crack growth rate in an aggressive environment is a summation of three components:

$$(\frac{da}{dN})_e = (\frac{da}{dN})_f + (\frac{da}{dN})_{cf} + (\frac{da}{dN})_{scc} \quad 2\text{-}12$$

Where $(^{da}/_{dN})_f$ represents the crack growth rate in an inert environment (pure fatigue term); $(^{da}/_{dN})_{cf}$ is the crack growth rate of a cycle-dependent corrosion fatigue process and $(^{da}/_{dN})_{scc}$ corresponds to the sustained load crack growth rate at K levels above K_{ISCC} (threshold stress intensity factor in stress corrosion cracking), which can be expressed by $\int_0^T \frac{da}{dt}dt$, where da/dt is the crack growth rate related to stress intensity factor and T is the cyclic period [126]. Kim [127] applied this superposition model into the prediction of corrosion fatigue life in aluminum alloys by considering the mechanism of corrosion fatigue to be hydrogen induced embrittlement. However, it was recognized that determination of the second term $(^{da}/_{dN})_{pcf}$ of equation (5) was extremely difficult [127][128].

2.4.2.2 Competition model

According to Austen [129], two different corrosion fatigue crack propagation behavior below and above the threshold stress intensity ($K_{ISCC)}$ for stress corrosion was discovered. The corrosion fatigue behavior, therefore, could be divided into three types, as presented in Figure 2-15. True corrosion fatigue (Figure 2-15 (a)) is characterized by the synergistic effect of corrosion and cyclic loading; stress corrosion fatigue (Figure 2-15 (b)) only occurs when stress intensity factor range exceeds K_{ISCC}. Figure 2-15 (c) implies that true corrosion fatigue and stress corrosion fatigue can occur concurrently in some situations. Based on above knowledge, Austen [129] proposed that the process of fatigue and stress corrosion fatigue are mutually competitive and the crack growth is determined by the process that has a faster growth rate at prevailing ΔK:

$$(\frac{da}{dN})_e = Max\,\{\left(\frac{da}{dN}\right)_f, \left(\frac{da}{dN}\right)_{scc}\} \qquad 2\text{-}13$$

This model proved not to be appropriate at low stress intensities and showed difficulty in predicting the CFCG rate at low frequencies [130]. Main reason was found to be the effect of the process interaction.

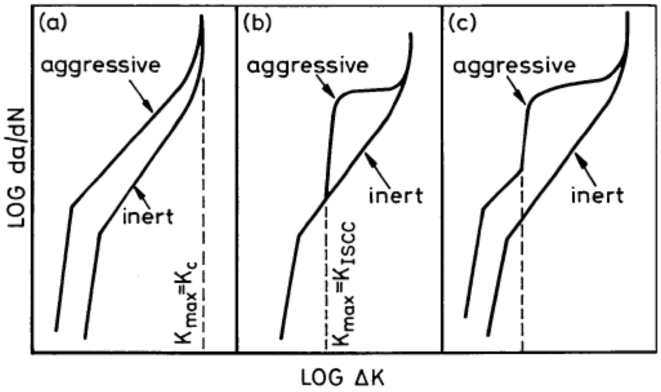

Figure 2-15 Basic types of corrosion fatigue crack growth behavior: (a) true corrosion fatigue; (b) stress corrosion fatigue; (c) the combination of true corrosion fatigue and stress corrosion fatigue [129]

2.4.2.3 Process interaction model

Rhodes [130] stated that corrosion fatigue is an interaction process between pure fatigue crack propagation and stress corrosion cracking. The effects of fatigue crack propagation and stress corrosion cracking are added together but each process is modified by the other to account for the process interaction:

$$(\frac{da}{dN})_e = C(\Delta K_{eff})^m + \int_0^{1/f} A\gamma K_{eff}^{\alpha} dt \qquad 2\text{-}14$$

Where K_{eff} is the effective stress intensity factor adjusted to explain the effect of environment on fatigue and γ is used to account for the effect of cyclic loading on stress corrosion rate. C, m are material constants. A and α are coefficients originating from the relationship between K and K_{eff}. This "process interaction model" appears to be able to give better correlation with experimental results than either superposition model or competition model. As the significance of stress corrosion cracking is emphasized in this model and the studied magnesium alloys in this paper are highly susceptible to the corrosive environment, it is appropriate to model the corrosion fatigue crack propagation behavior of magnesium alloys based on the "process interaction model". However, this model over emphasized the significance of the SCC in the whole crack propagation process and not considered the effect of SCC in unloading portion.

Overall, from the CFCP models published in literature, the corrosion fatigue crack propagation process should be closely related to fatigue and stress corrosion cracking but the interaction between them was not explicitly explained. To narrow down this gap, a new corrosion fatigue crack propagation model is proposed and will be detailed discussed in chapter 6.

Chapter 3 Materials and experimental methods

This chapter is on materials and methods. It mainly includes information on the materials, specimen preparation, and characterization, as well as the procedure of conversion coating treatment. In addition, this chapter provides detailed information regarding the experimental techniques and equipment to characterize the microstructure, corrosion and corrosion fatigue performances of coated and uncoated samples.

3.1 Materials

The Mg alloys used in this research include a direct chill cast alloy AZ31B, a commercial extruded alloy AZ80, and a commercial extruded alloy ZK60. As-cast AZ31B with the dimensions of Φ300 mm×500 mm, and as-extruded AZ80, and as-extruded ZK 60 with the dimensions of Φ63.5 mm×65 mm were all provided by Magnesium Elektron North America. The chemical composition of these alloys is given in Table 3-1.

Table 3-1 Chemical composition of Mg alloys used in this investigation (wt.%)

Alloy	Al	Zn	Mn	Si	Cu	Zr	Others	Mg
AZ31B	2.9	0.76	0.25	0.01	<0.03	/	<0.30	Balance
AZ80	8.4	0.48	0.20	0.026	0.0026	/	<0.30	Balance
ZK60	/	5.8	/	/	/	0.61	<0.30	Balance

The first part of this research focuses on the surface corrosion protection of Mg alloys, and thus the flat specimen geometry was used. In order to optimize the conversion coating process parameters, as-cast AZ31B was utilized as the base substrate in this part of the research. Flat coupons with the dimensions of 50mm×25mm×3mm (Figure 3-1(b)) were machined from the as-cast billet as present in Figure 3-1(a). These coupons were first mechanically ground up to 800 grit emery sandpaper with ethanol, followed by ultrasonic degreasing in acetone. Then they were stored for subsequent coating treatment after rinsing in ethanol and drying in dry air stream.

The developed surface corrosion protection methods were further studied on an actual component. A lower control arm forged from Mg extrusion was the component used. A control arm is a vital part of the front suspension in a vehicle. A Mg control arm, as a potential replacement of the current Al one, for the sake of light-weight design was employed in this part of the study. As-extruded AZ80 [131] and ZK60 [132] billets were forged into the shape of a control arm as presented in Figure 3-1(c) under 250°C at a rate of 20 mm/sec. Flat coupons with the same dimensions as the cast alloy coupons (Figure 3-1(b)) were cut from the control arm for the subsequent corrosion research stage, in which the optimal conversion coatings plus a top powder coating are applied to the coupons to investigate the overall corrosion performances of the extrusion-forged control arm.

To characterize the fatigue behavior of uncoated and coated Mg alloys, different specimen geometry was adopted for fatigue testing as presented in Figure 3-1(d), based on the American Society for Testing and Materials (ASTM) standard, ASTM E8/E8M [133]. The cylindrical fatigue specimen was as well cut from the as-cast billet and the control arm at the Machine Shop of the University of Waterloo.

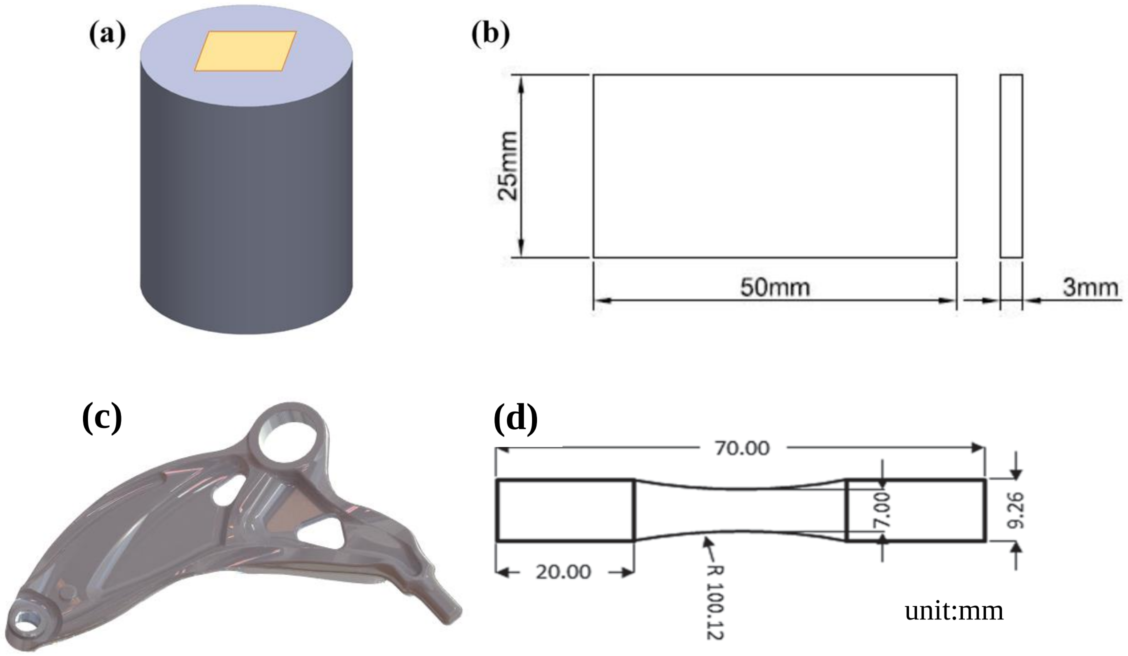

Figure 3-1 Illustration of the original billet and component used for machining test coupons and dimensions of coupons: (a) cast billet (the rectangular area shows an example of the flat specimen cut from the billet); (b) flat coupon for screening tests; (c) extrusion-forged front lower control arm; and (d) cylindrical specimen for fatigue tests

3.2 Coating treatment

Phosphate permanganate (Mn-P) conversion coating and chromate conversion coating (CCC) were selected based on literature to treat AZ31B. Electrophoretic coating (E-coating) and powder coating were both used as a topcoat in the coat system.

3.2.1 Phosphate permanganate conversion coating

Conversion coating treatment was conducted in the corrosion lab of CanmetMATERIALS. Potassium permanganate ($KMnO_4$ 15g/L), potassium dihydrogen phosphate (KH_2PO_4 3g/L), manganese sulfate ($MnSO_4$ 4g/L) and ethylenediaminetetraacetic acid, namely EDTA ($C_{10}H_{16}N_2O_8$ 1g/L) were used to prepare the aqueous conversion bath. This recipe was modified from Ref.[51] by replacing manganese nitrate ($Mn(NO_3)_2$) with $MnSO_4$ for the free Mn^{2+} and adding a tiny of EDTA which plays an important role in facilitating the formation of corrosion resistant oxides [134]. The effect of each processing parameter on coating resistance was studied. To figure out the optimal processing parameters, an orthogonal testing matrix was quite necessary to reduce the number of tests. The experiment design is presented in Table 3-2.

Table 3-2 Description of Mn-P based conversion coating process

Process reference number	Bath pH value	Immersion time (s)	Bath temperature (ºC)
1	1.8	45, 70, 90, 180, 600	Room temperature (RT)
2	1.8, 2.3, 2.8	90	RT
3	1.8, 2.0, 2.5, 3.0	180	RT
4	3.0	600	RT, 50, 75

The following reviews the detailed steps of producing a Mn-P coating on Mg alloy coupons.

(1) Dissolution of the conversion bath constituents and heat treatment

Chemical constituents (no order required) were firstly dissolved in de-ionized water on a Cole-Parmer magnetic stirring hot plate (Figure 3-2), and then the conversion solution in a beaker was heated to a targeted temperature (20℃, 50℃, 75℃). Graduated cylinder and mass scale were used to measure the amount of water and chemical reagents needed, respectively.

Figure 3-2 Mn-P conversion process on a magnetic stirrer with a heat plate

(2) Adjustment of pH value of the conversion solution.

After stabilization of the bath temperature, the pH value of the conversion solution needed to be adjusted to a targeted level by adding potassium hydroxide (KOH) or nitric acid (HNO_3). A pH reader was used to determine the pH value of the prepared solution.

(3) Chemical conversion processing

Flat coupons of Mg alloy AZ31B were immersed in the solution for a certain period of time and then were immediately washed by water and dried by air stream. Coated samples should be stored in a drying oven for subsequent testing. After the coating process, the conversion solution was transferred to a disposal bottle and marked carefully.

3.2.2 Chromate conversion coating

This coating process is very similar to that of Mn-P coating except that the bath solution was prepared by using manganese(II) sulfate monohydrate ($MnSO_4 \cdot H_2O$ 50g/L), magnesium sulfate ($MgSO_4$ 50g/L), and sodium chromate dehydrate ($Na_2Cr_2O_7$ 100g/L) [135][136]. It is worth noticing that the disposal of this bath solution should be carefully performed because of the toxicity of chromate.

3.2.3 Top coating

The E-coating process was performed by a local company MetoKote in Cambridge, Ontario, Canada. As explained in Chapter 2, E-coating as a 'wet' process typically involves immersing the sample into a bath solution consisting of epoxy resin, painting assisted by an electric field, and a step of curing in an oven to promote more uniform distribution of the coating. In contrast, powder coating is a “dry” process in which a spray gun is usually used to apply the dry powder consisting of chemicals such as epoxy resin and some curing agents onto the Mg surface. Curing in an oven is also necessary to finalize the coating. In this research, powder coating was provided by the company JP Powder Coating Inc in Kitchener, Ontario, Canada. Two types of powder coatings were obtained via being cured under a high temperature (P1) and a low temperature (P2). The specific treatment parameters are proprietary and not given here. Figure 3-3 shows the images of flat coupons and cylindrical specimens with an E-coat.

Figure 3-3 Typical flat coupons and cylindrical fatigue specimens with an E-coat

3.3 Experimental Methods

After coatings were deposited on the Mg ally specimen surface, the following analysis and tests were conducted to characterize the surface morphology, corrosion performance, and corrosion fatigue property:

3.3.1 Microstructural characterization

The surface morphology, microstructure and chemical composition of the conversion coating were characterized using Philips XL30 SFEG SEM in the secondary electron (SE) mode as presented in Figure 3-4(a) at CanmetMATERIALS, Hamilton, Canada. The composition of the surface and cross-section of the coatings were analyzed by Energy Dispersive Spectrometry (EDS) mapping incorporated into the SEM. EDS was performed at 20 keV. Additionally, the composition of the corrosion product of the Mg alloy coupons post corrosion testing was investigated by x-ray Diffraction (XRD) using Cu-Kα radiation with a Bruker-D8 Discover equipped with advanced 2D-detector as presented in Figure 3-4(b) at the University of Waterloo.

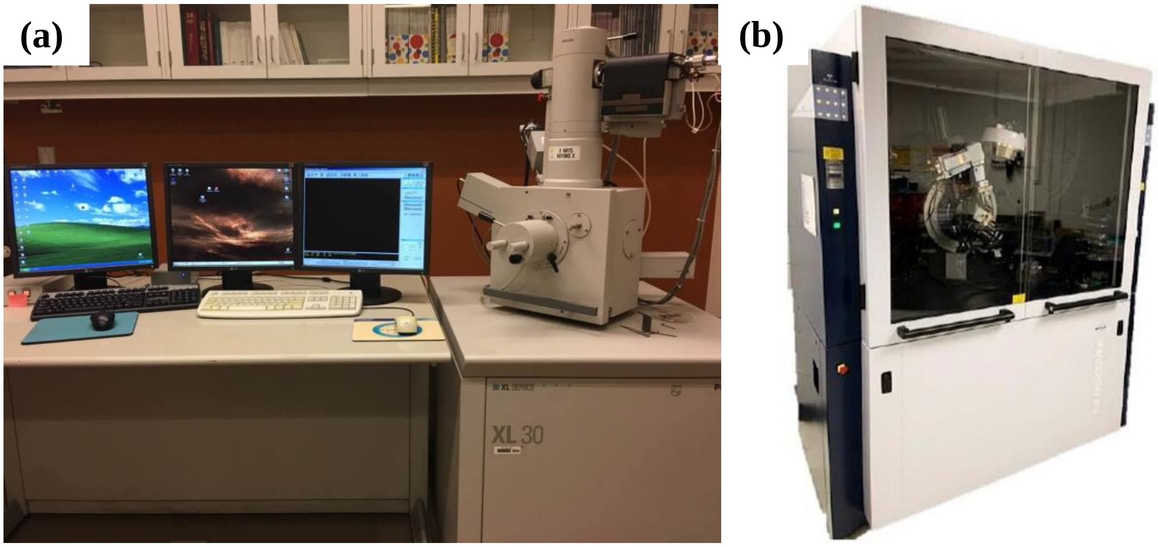

Figure 3-4 (a) Scanning electron microscopy and (b) Bruker D8-Discover XRD machine

3.3.2 Electrochemical testing

Advanced electrochemical testing techniques including potentiodynamic polarization and electrochemical impedance spectroscopy (EIS) measurements were performed to study the corrosion behavior of the uncoated and coated Mg alloy coupons. The electrochemical tests were all conducted in a 3.5% sodium chloride (NaCl) aqueous solution using a potentiostat/galvanostat electrochemical system (Solartron SI 1287 and 1255B as seen in Figure 3-5) at room temperature. A traditional three-electrode setup was adopted with the Mg alloy specimen acting as working electrode, a platinum gauze as counter electrode, and an Ag/AgCl electrode in a saturated KCl solution as reference. The exposed surface area of the specimen was about 1 cm^2.

Prior to the polarization scan and EIS measurement, each sample was immersed in the testing solution for 30min to reach a steady open circuit potential (E_{OCP}). The potentiodynamic polarization measurement was then conducted by sweeping the potential from -200mV to +500mV with respect to the E_{OCP} at a scan rate of 1 mV/s and a Tafel plot was obtained after the electrochemical measurement, as can be seen from a typical Tafel polarization diagram [137] in Figure 3-6 (a). For Mg alloys, the cathodic branch is related to hydrogen evolution (see Eq.2-5) and the anodic branch is related to Mg alloys' dissolution (see Eq.2-4). While for Mg alloys with a surface coating, the anodic branch generally reveals the features regarding on the corrosion resistance of the surface coating. Corrosion current density (i_{corr}) can be acquired by an extrapolation of the cathodic or anodic Tafel slop back to E_{corr}. Figure 3-6 (b) [137] shows the polarization diagram for a passivable system with anodic and cathodic branches. At potentials higher than E_{corr}, corrosion rate or the current density increases until the passivation potential (E_{pp}), where the active-passive transition occurs. Above the E_{pp}, it is the passive zone in which the current density is maintained at a steady and low value. When the applied potential reaches a point where the current density increases again, pitting corrosion or breakdown of the film occurs. This potential is defined as pitting potential (E_p).

The EIS measurement was conducted using a frequency response analyzer (FRA) and the spectrum was recorded in the frequency range of 10 mHz – 100 kHz at an open circuit potential with a sinusoidal perturbation amplitude of 10mV. The impedance data was displayed as a Bode plot.

All the experimental data were presented in the form of the average± the standard deviation of three measurements.

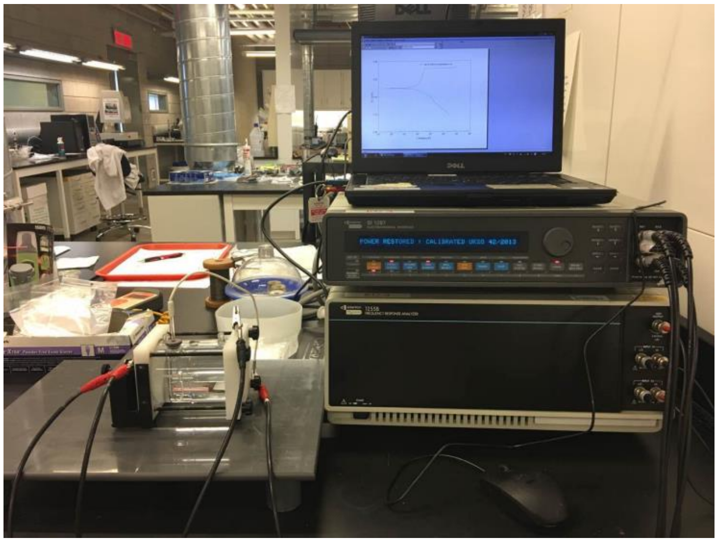

Figure 3-5 The Solartron Analytical 1287A potentiostat/galvanostat and Solartron 1255B frequency response analyzer use for electrochemical testing

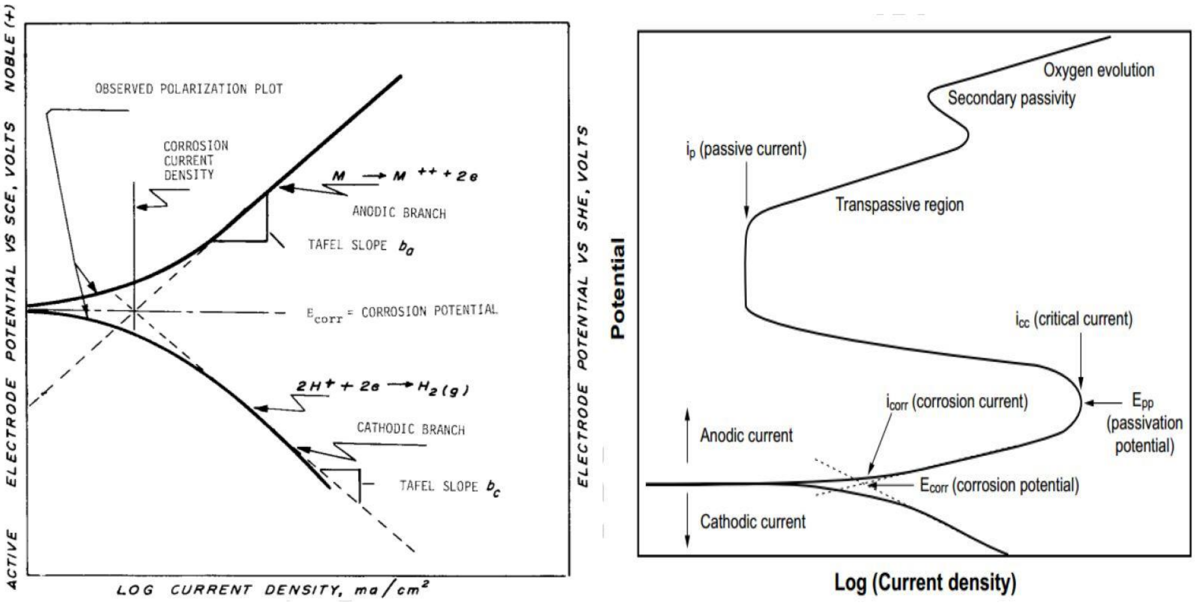

(a) (b)

Figure 3-6 (a) Typical cathodic and anodic Tafel polarization diagram; (b) Hypothetical polarization diagram for a passivable system with anodic and cathodic branches [137]

3.3.3 Salt fog/spray chamber corrosion test

The salt spray chamber test was performed at the corrosion lab of CanmetMATERIALS, and two types of chamber corrosion tests were used in this research. One is based on the standard ASTM B117 [138], which is a static corrosion test. This test was conducted in a chamber as presented in Figure 3-7, containing 5.0 wt. % NaCl fog with the temperature maintained at 36˚C and the solution pH maintained between 6.5 and 7.2. For characterizing coated Mg alloys, the scribe test based on standard ASTM D1654 [139] was conducted and the scribed coated specimens were exposed to the corrosive continuous salt fog environment given by ASTM standard B117. The lengthwise scribe line with a width of 0.5μm was obtained via a specialized scribing tool. The other chamber corrosion test is based on the standard SAE J2334 [140], which is a cyclic corrosion test. One cycle of this test includes first 6 hours of wet exposure under 100% relative humility (RH) at 50℃, followed by15 minutes of salt spraying consisting of 0.5%NaCl, 0.1%$CaCl_2$, 0.075%$NaHCO_3$ at 23-25℃, and then 17 hours and 45 minutes of air drying under 50% RH at 50℃.

In each test, the coupons were placed in the corrosion chamber at an angle of 15˚-30˚ from the vertical direction. Two samples were taken out each time at desired time point to characterize the corrosion kinetics of the specimens. After the salt fog or spray testing, a chromate solution was used to clean the tested coupons and the corrosion products obtained from the surface of coupons were analyzed by XRD. To calculate the weight loss, the weight of each bare or coated sample was recorded prior to and post the corrosion test after removing the corrosion products. For the scribed coated sample, the scribe width should be measured from at least six points around the corrosion area and recorded to determine the average rust creepage (c) following the equation below:

$$c = \frac{w_c - w}{2} \qquad 2\text{-}15$$

where w represents the width of the original scribe prior to the chamber corrosion test and w_c is the mean overall width of the corrosion zone post the chamber corrosion test.

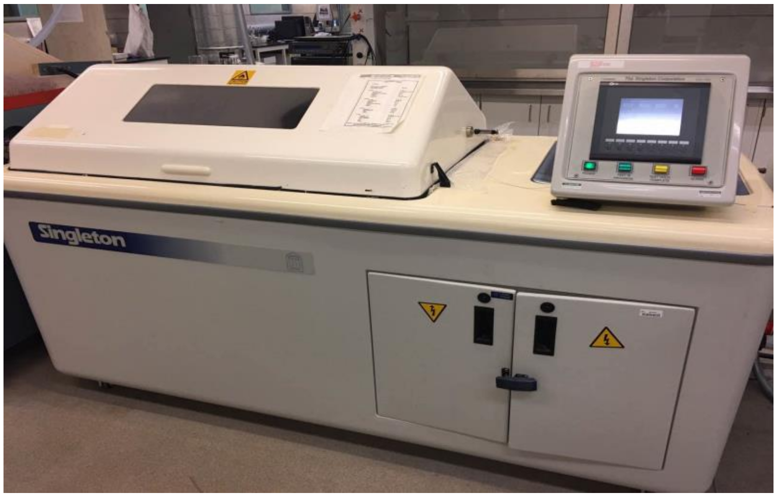

Figure 3-7 The chamber for corrosion test

3.3.4 Characterization of corrosion pits

In order to further investigate the corrosion behavior of the coated sample, the specimen from the chamber corrosion test above was cleaned and prepared for characterizing the corrosion pits using a 3D laser profilometer as seen in Figure 3-8 in the corrosion lab of CanmetMATERIALS. The rectangular coupon surface was divided into four equal areas, from which 20 corrosion pits were selected to determine the average corrosion pit depth.

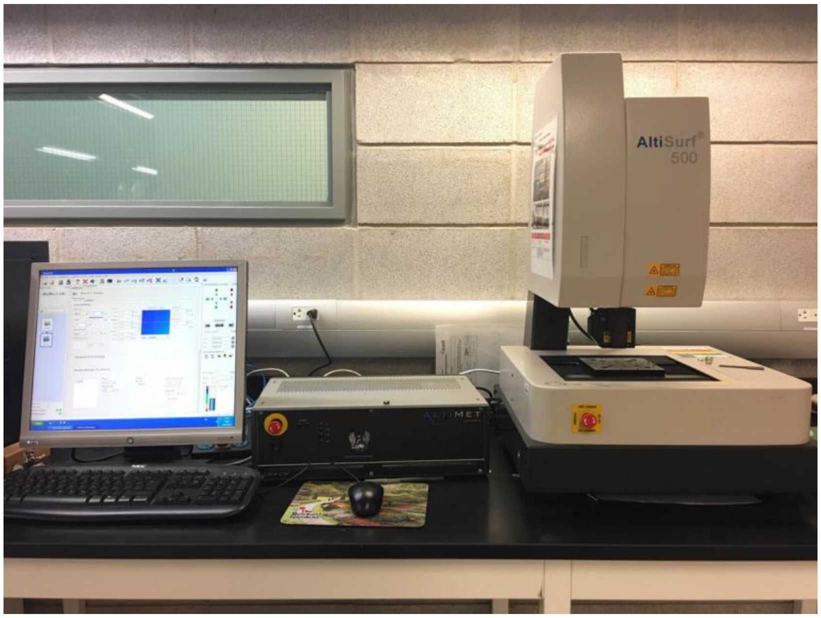

Figure 3-8 3D optical profilometer for charactering the corrosion pit

3.3.5 Fatigue and corrosion fatigue test

The R.R.Moore machine, recognized as the standard facility for rotating beam fatigue test, was used to perform the fatigue and corrosion fatigue tests on straight shank specimens, incorporating the equipment bringing in a corrosive environment, as shown in Figure 3-9. The machine is based on the rotating beam principle. The specimen functions as a simple beam symmetrically loaded at two points. When rotated a full revolution, the specimen would pass through a full reversal of compression and tension. During testing, the specimen's surface is subjected to the greatest amount of stress and hence this type of fatigue testing is especially useful for determining fatigue properties of surface coatings. Additionally, an easy-to-read digital cycle counter is able to provide an accurate display of completed cycles. By applying different loads to the tested specimen, different numbers of cycles to failure will be generated and so is the S-N curve.

The fatigue test was conducted at different stress amplitudes ranging from 60 MPa to 200 MPa. Test frequency was between 60-100 Hz. For the corrosion fatigue test, the specimens were tested at various stress amplitudes between 40 and 140 MPa. A corrosive environment can be achieved by dripping a salt solution (generally 3.5% NaCl) down onto the specimen gauge surface through a tube from a large container which had a controlling valve to control the solution flow rate during the fatigue testing, as can be seen in the designed salt chamber in Figure 3-9(b) [141]. The solution would be recycled by another tank underneath the fatigue machine. The drop speed that flowed over the gauge section of the specimen was maintained at roughly 40 ml/min during the test. To reveal the effect of the corrosive medium on the fatigue performance of the specimen, a fixed frequency of 30 Hz was used for all fatigue and corrosion fatigue tests. A test terminates whenever a specimen breaks or when it reaches the run-out limit of 10 million cycles. Two specimens were tested for each stress amplitude to give an average of the test results.

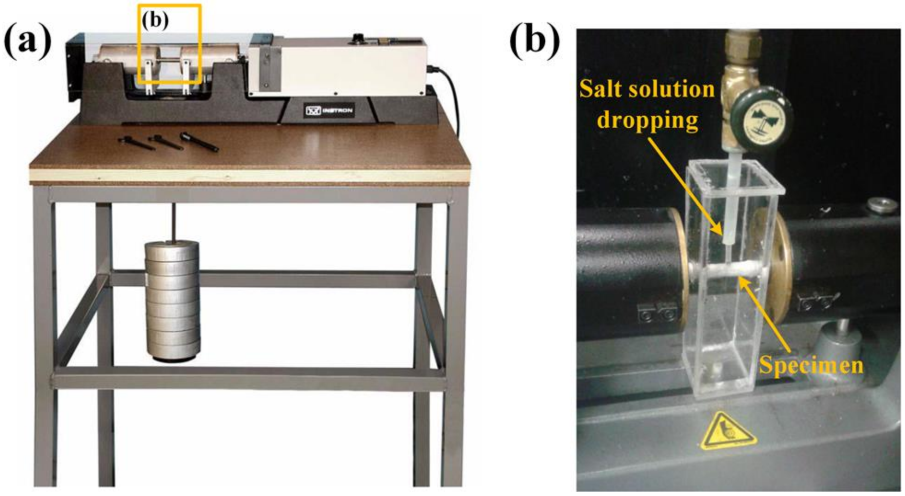

Figure 3-9 (a) An Instron Rotating-bending test machine and (b) the device designed for introduction of the corrosive medium during corrosion fatigue test

Chapter 4 Fabrication of corrosion protective surface coating on AZ31B

To fulfill the objectives of this research, a corrosion protective surface coating was first deposited on the Mg alloys. Mn-P conversion coating is a pretty promising candidate for the replacement of chromate conversion coating for surface preparation and corrosion protection of Mg alloys owing to the similarity of permanganate to chromate. In this chapter, with no variation in the chemical composition of the coating bath, and the effects of coating processing parameters including the solution pH, immersion time, and bath temperature were investigated. Based on these results, a two-stage conversion coating process was developed to obtain a high-quality Mn-P coating.

4.1 Processing parameters-microstructure-corrosion performance relationship of the Mn-P coating

As reviewed in literature [51][142][143], the formation of the Mn-P conversion coating may include the following several stages:

At first, when the AZ31 alloy is immersed into the bath solution, the loose oxide film formed on the surface of the substrate (Mg and Al are both highly active and easily oxidized in the air) is preferentially dissolved according to reactions (4-1) and (4-2), leading to the substrate exposed to the bath solution.

$$MgO + 2H^+ \rightarrow Mg^{2+} + H_2O \qquad 4\text{-}1$$

$$Al_2O_3 + 6H^+ \rightarrow 2Al^+ + 3H_2O \qquad 4\text{-}2$$

Then, the Mg begins to dissolve in the solution and hydrogen evolution occurs through reaction (4-3). The deletion of H+ by reactions (4-1) to (4-3) causes a pH increase at the Mg coupon and solution interface. Consequently, the excess of Mg^{2+} and OH^- will immediately precipitate in the form of $Mg(OH)_2$ through reaction (4-4) as the first layer of the coating.

$$Mg + 2H^+ \rightarrow Mg^{2+} + H_2 \uparrow \qquad 4\text{-}3$$

$$Mg^{2+} + 2OH^- \rightarrow Mg(OH)_2 \downarrow \qquad 4\text{-}4$$

Next, the continuous consumption of H^+ accompanied by hydrogen evolution facilitates the precipitation of insoluble manganese oxide (MnO_2) and insoluble manganese phosphate ($Mn_3(PO4)_2$) through reactions (4-5) and (4-6) on top of the $Mg(OH)_2$ film. Dehydration of the coating in the subsequent drying process results in the transition of $Mg(OH)_2$ to MgO and thus network cracks are usually observed. In the end, the Mn-P conversion coating would mainly contain phases such as MnO_2, MgO, $Mn_3(PO4)_2$, $Mg(OH)_2$. The processing parameters play a key role in controlling the coating thickness, compactness and compositions proportion, so a systematical experimental study on the effects of processing parameters on the microstructure and corrosion performance of the Mn-P coating is carried out.

$$2\mathrm{MnO_4^-} + 3\mathrm{Mn^{2+}} + 2\mathrm{H_2O} \rightarrow 5\mathrm{MnO_2} \downarrow + 4\mathrm{H^+} \qquad 4\text{-}5$$

$$4Mn^{2+} + 3H_2PO_4^- \rightarrow MnHPO_4 + Mn_3(PO_4)_2 \downarrow + 5H^+ \qquad 4\text{-}6$$

4.1.1 The effects of immersion time

Figure 4-1 shows the effect of the immersion time on the coating morphology of coupons treated in a bath at pH value of 1.8 under room temperature. It can be clearly seen from the optical images of the coated samples (Figure 4-1 (a, c, e, g, i)) that a golden-yellow layer started to form on the alloy surface after 45 s. With the increase in the immersion treatment time, the color of the coating became darker and darker and even a black coating was obtained after 600 s. Furthermore, the adhesion property of the coating became unacceptable when the immersion time went beyond 180 s as the coating layer could be wiped off easily. From the SEM images, we can see that after 45 s (Figure 4-1 (b)), the substrate was coated with a thin layer while some cast defects and second phase particles containing elements Mg, Al and Zn (Figure 4-1 (k)) remained uncovered. Besides, a few shallow cracks appeared in the coating. With the immersion time increased to 70 s, the coating became thicker as almost all the cast defects which appeared in Figure 4-1(b) were almost not found in Figure 4-1(d). From the EDX result (Figure 4-1(m)) for Area 1 in Figure 4-1(f), the produced coatings were mainly composed of elements Mg, O, Mn, and P, which corresponded to the $Mn_3(PO4)_2$, $Mg(OH)_2$ according to reactions (4-4) to (4-6). Meanwhile, some white compounds containing Mn, Mg, O (Figure 4-1 (l)) which are likely the mixtures of MnO_2 and MgO started to precipitate along the shallow cracks. MnO_2 and MgO are both insoluble in the aqueous solution and thus they could prevent the outside corrosive species from penetrating through these shallow cracks and reaching the Mg substrate [51]. At 90 s of the immersion time, wider cracks (Figure 4-1 (f)) formed in the coating, which would reduce the corrosion resistance of the coating. After 90 s, cracking issue became more severe and the adhesion property of the coating was deteriorated, as shown in Figure 4-1 (h, j).

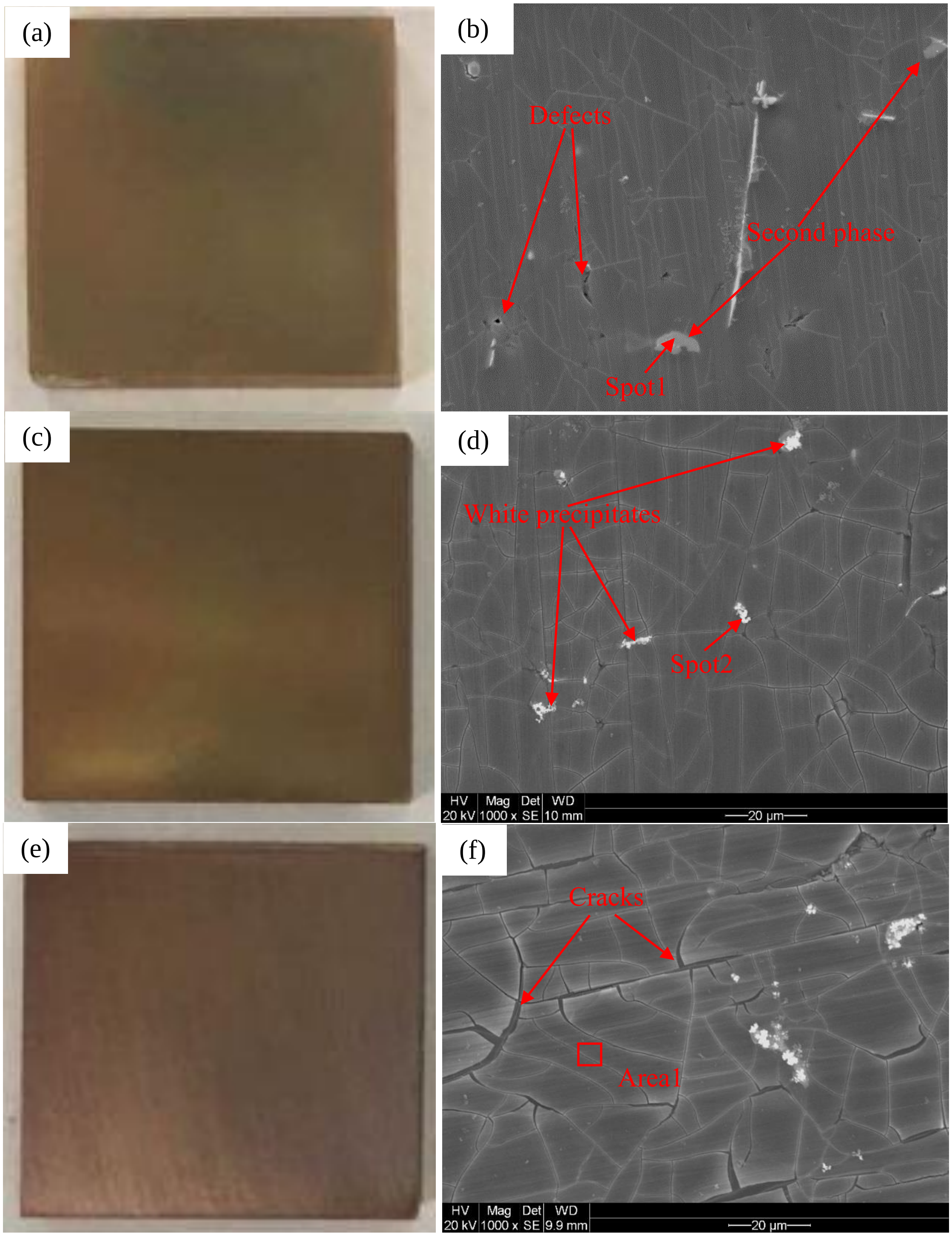
(a)
(b)
Defects
Second phase
Spot1
(c)
(d)
White precipitates
Spot2
HV Mag Det WD
20 kV 1000 x SE 10 mm
20 μm
(e)
(f)
Cracks
Area1
HV Mag Det WD
20 kV 1000 x SE 9.9 mm
20 μm

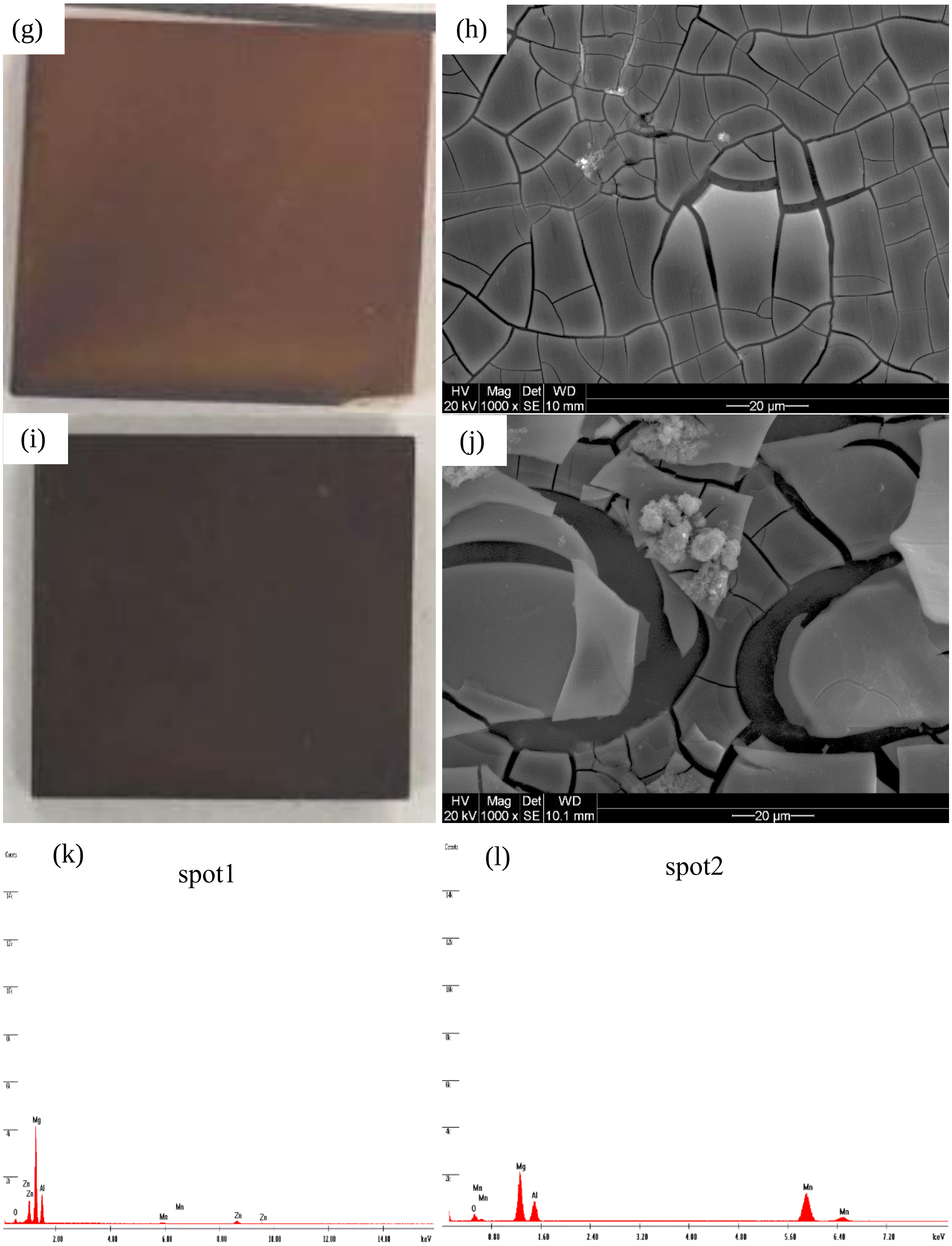
(g)
(h)
HV
Mag
Det
WD
20 kV
1000 x
SE
10 mm
20 µm
(i)
(j)
HV
Mag
Det
WD
20 kV
1000 x
SE
10.1 mm
20 µm
(k)
spot1
Counts
14k
12k
10k
8k
6k
4k
2k
Mg
Zn
Zn
Al
O
Mn
Mn
Zn
Zn
2.00
4.00
6.00
8.00
10.00
12.00
14.00
keV
(l)
spot2
Counts
14k
12k
10k
8k
6k
4k
2k
Mg
Mn
Mn
O
Al
Mn
Mn
0.80
1.60
2.40
3.20
4.00
4.80
5.60
6.40
7.20
keV

(m)

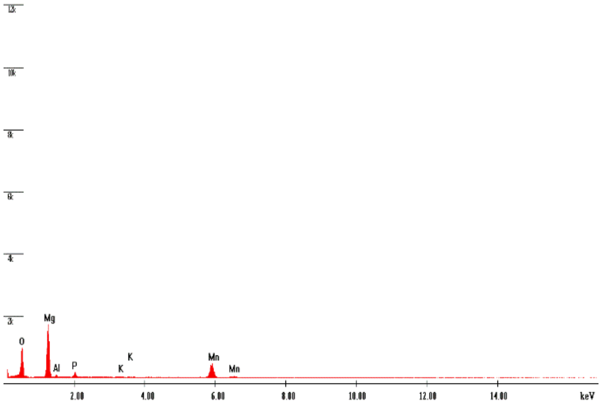

Figure 4-1 The optical (a, c, e, g, i) and SEM (b, d, f, h, j) images (1000x) of the Mn-P coated AZ31B alloy samples obtained after various immersion time in a solution at pH 1.8 under room temperature: (a)(b) 45 s; (c)(d) 70 s; (e)(f) 90 s; (g)(h) 180 s; (i)(j) 600 s.(k)(l)(m): The EDS results for corresponding spot1, spot2, and area1 in (b)(d)(f)

Potentiodynamic polarization test was then performed on coated Mg alloy coupons to investigate the effect of immersion time on the corrosion performance of the coating. The corrosion potential and corrosion current can be obtained from the polarization curve. Corrosion potential (E_{corr}) is defined as a potential at which the anodic reaction rate equals the cathodic reaction rate and thus no net current flow occurs; It generally gives a corrosion tendency of a given material and can be measured from the potential difference between a reference electrode and the surface of a metal [144]. Corrosion current is the dissolution current at E_{corr}; It is proportional to the corrosion rate. A smaller corrosion current indicates a lower corrosion rate and better corrosion resistance. As can be seen from Figure 4-2, the corrosion potential of all the coated samples shifted towards more noble direction and lower corrosion current was seen for all coated samples compared to the bare substrate, showing improved corrosion resistance resulted from the coating. The change of corrosion potential of the coated samples was not monotonous with the increase of immersion time. For instance, the corrosion potential of the sample coated for 45 s was -1.389 V in contrast to -1.486 V for the bare substrate. When the immersion time increased to 70 s, the corrosion potential of the coated alloy became more noble (-1.287 V). However, after 70 s, the corrosion potential of the coated alloy started to decrease (became more negative) with the further extension of immersion time. Therefore, the potentiodynamic polarization results show that the sample treated for 70 s exhibited the best corrosion resistance among all coated samples. When the immersion time exceeded 180 s, thicker coatings were obtained but with more defects and cracks, which led to lower corrosion resistance and more negative corrosion potential. The results are consistent with the microstructural analysis above (Figure 4-1).

In summary, with the increasing immersion time, the coating grew thicker and more corrosion resistant. Simultaneously, the content of corrosion resistant precipitates containing MnO_2 and MgO in the coating increased as well. However, when the treatment time was too long, the corrosion resistance of the coated samples would decrease due to the formation of large cracks in the coating. The formation of cracks is caused by the tensile stress developed in the coating due to volume contraction during the subsequent drying process. Larger volume contraction for the case of a thicker coating resulted in more residual tensile stress in the surface coating [82]. Therefore, an optimum conversion treatment time exists for a given bath under certain pH and temperature conditions. In the above case, where the sample was treated in a solution with pH 1.8 at room temperature, the optimum immersion time is no more than 90 s.

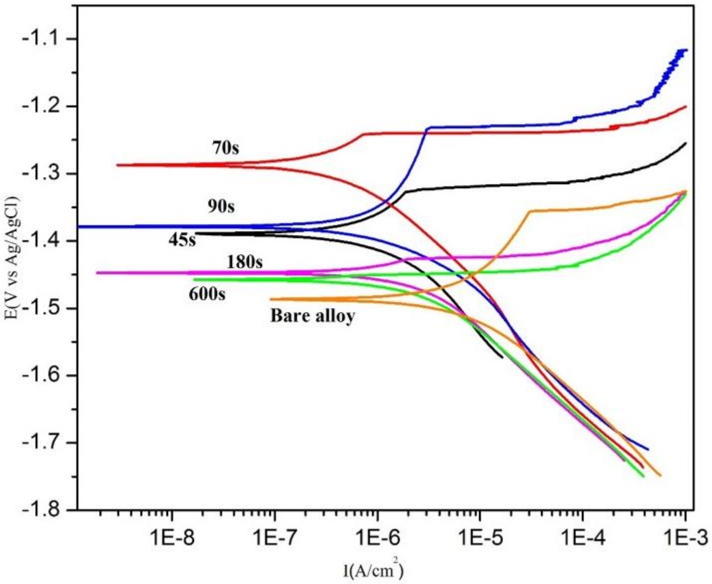

Figure 4-2 Polarization curves for the bare and coated AZ31B samples treated after various time periods in the coating bath at pH 1.8 under room temperature.

4.1.2 The effects of pH value

Bath pH is reported to significantly influence the surface morphology and thickness of the Mn-P coating. This is mostly related to the reaction rate promoted or retarded by H^+ concentrations in the bath solution. To investigate the effects of pH on the microstructure and corrosion property of the Mn-P coating, AZ31B alloy specimens were treated at three pH values (1.8, 2.3, and 2.8) for 90 s and at four pH values (1.8, 2.0, 2.5, and 3.0) for 3 min. Figure 4-3 presents the surface morphology of the coated AZ31B alloy obtained at various pH values with an immersion time of 90 s. As can be seen from the SEM images, at bath pH 1.8, a crystalline surface coating was deposited on the surface of the AZ31 alloys but many cracks in the coating were seen on the sample surface (Figure 4-3(a)). Dehydration in the dry process causes the shrinkage of the coating volume, which induces internal tensile stresses and thus generate a number of cracks. Surface cracks are detrimental to the coating because they would allow the outside corrosion species to penetrate into the substrate [51]. However, if a thick coating was formed, it is still possible that the cracks only existed on the outer layer of the coating and may not penetrate through the entire thickness of the coating. For the sample treated at pH 2.3, surface grooves of the substrate and second phase precipitates from casting were still visible on the sample surface, indicating that the coating was very thin (Figure 4-3 (b)). However, no cracking was seen in the coating, which was different from the commonly seen features of Mn-P coatings published in literature. In addition, there was no white compounds found in the coating like those appeared in the coating treated at bath pH 1.8. With the bath pH increased to 2.8, more apparent abrasion grooves were observed on the sample surface, which suggested that 90 s was too short to form a thick enough and corrosion resistant coating layer on the sample surface. This was also confirmed by the results of potentiodynamic polarization tests, as presented in Figure 4-4. It can be seen that even though there existed a few wide cracks, the coating obtained at bath pH 1.8 showed a higher corrosion potential and lower corrosion current than the other two coatings obtained at higher pH values, which manifested the importance of the coating thickness. In contrast, the samples treated in the solution with pH 2.3 and pH 2.8 had similar corrosion potentials and corrosion currents. Their corrosion potentials are only slightly higher and corrosion currents slightly lower than those of the bare substrate, which can be attributed to the small thickness of the coatings (i.e. a very thin coating layer). The bath solution with a low pH value would provide a higher concentrations of hydrogen ions for accelerating the reaction (4-3) to produce a larger amount of Mg^{2+} than a bath solution with a low pH value under the same immersion time. In this way, more content of $Mg(OH)_2$ would be generated in the conversion coating. Meanwhile, with plenty of hydrogen ions deleted, more content of MnO_2 and $Mn_3(PO_4)_2$ are acquired through the reactions (4-5) and (4-6). This explains why a low pH value generally increases the thickness of the Mn-P coating.

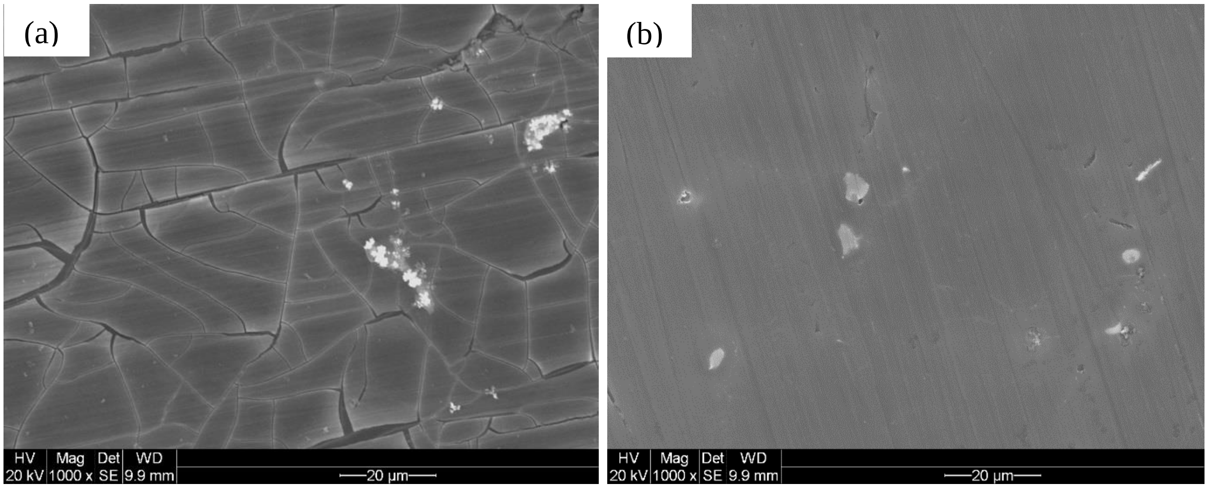

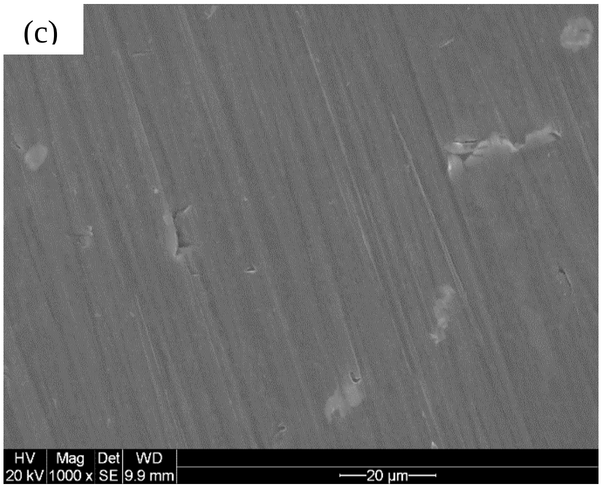

Figure 4-3 SEM images of the surface morphology of the coatings obtained at various pH values and 90 s of immersion time: (a) pH 1.8; (b) pH 2.3; and (c) pH 2.8

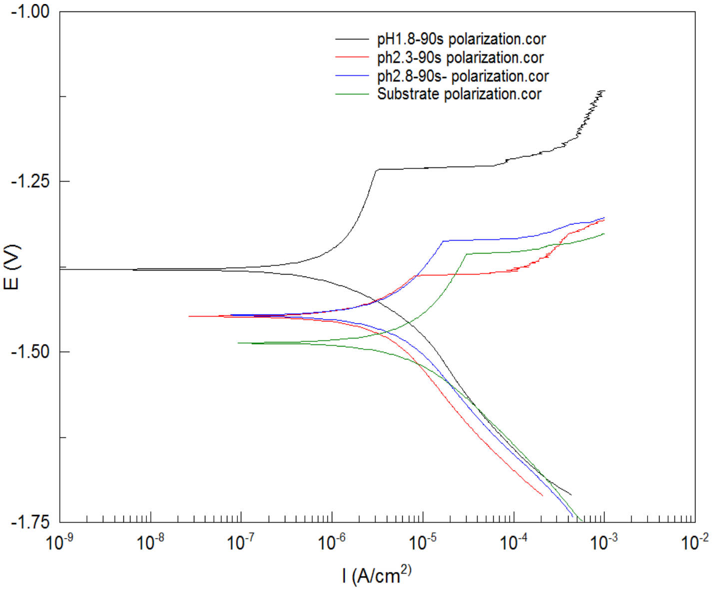

Figure 4-4 Potentiodynamic polarization curves for the bare AZ31B and coated samples obtained at various pH values and 90 s of immersion time under room temperature

Figure 4-5 and Figure 4-6 give the results of the SEM surface analysis and polarization test for the samples coated for 3 min (180 s) at various pH values (1.8, 2.0, 2.5, and 3.0). A similar trend like that for the above mentioned 90 s of immersion time on the coating microstructure was observed: thick coatings with severe cracking were obtained at low pH values while thin coatings with few or no cracks were obtained at high pH values. The coating generated at pH 3.0 showed the highest corrosion resistance compared to other coatings obtained at lower pH values (Figure 4-6), which probably can be ascribed to its improved compactness and higher coating thickness when the immersion time was relatively long (3 min). It is interesting to note that the sample obtained at pH 2.0 exhibited better corrosion resistance than that treated at pH 2.5. This might indicate that for the enhancement of corrosion resistance the role of coating thickness can outweigh that of coating compactness, since the specimen treated at pH 2.0 had a thicker coating but with more cracks than the specimen treated at pH 2.5.

In summary, the effects of bath pH on the coating include: (1) a thick Mn-P coating can be formed on the surface of Mg alloy AZ31B in a very short duration if treated in a low-pH bath (below 2.0) while it requires much more time to produce a relatively thick coating layer if treated in a high-pH bath (above 3.0); (2) the coating obtained in a low-pH bath tends to have wide cracks and low compactness while the coating built in a high-pH bath tends to be dense and have no significant cracks; (3) the integrity (i.e. extent of cracking), thickness and compactness of the coating are the main characteristics that determine its corrosion resistance.

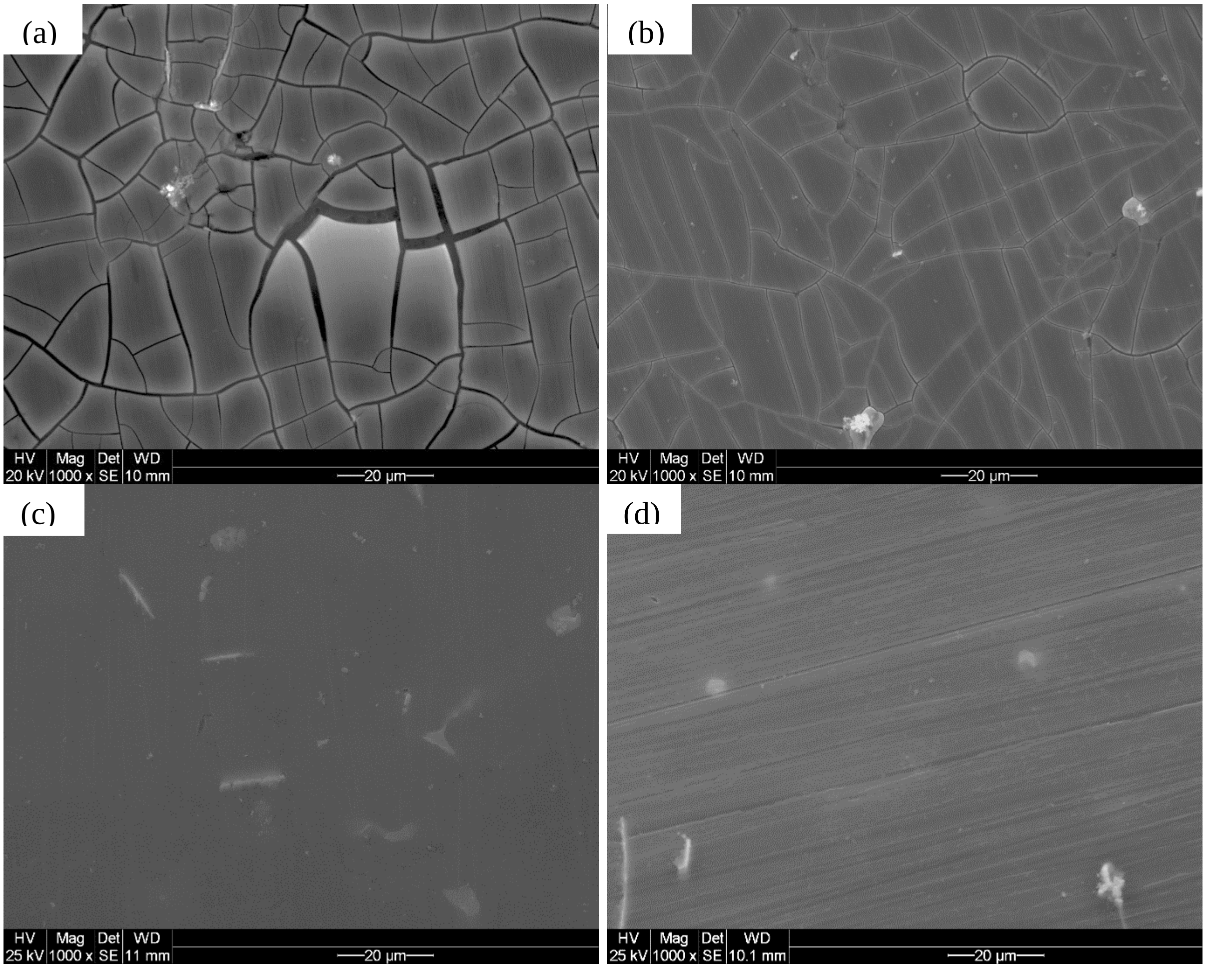

Figure 4-5 The SEM images of surface morphology of the coatings obtained at various pH values with immersion time of 3 min: (a) 1.8; (b) 2.0; (c) 2.5; and (d) 3.0

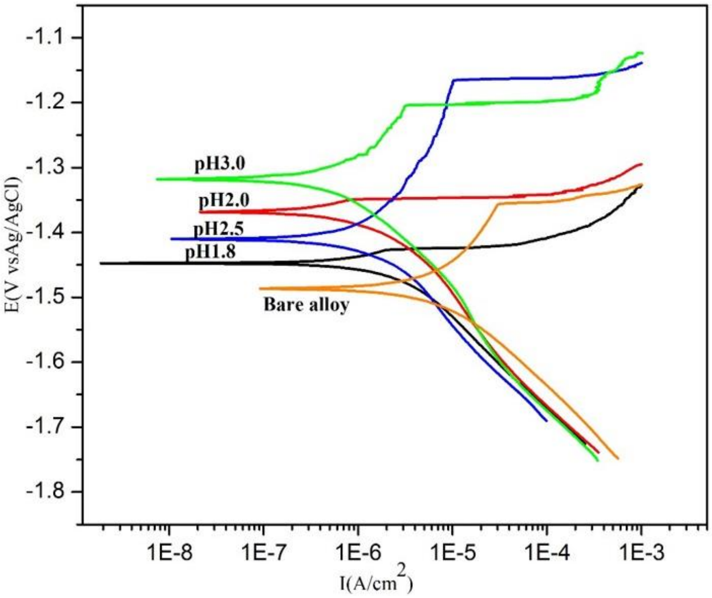

Figure 4-6 Potentiodynamic polarization curves for the bare AZ31B and coated samples treated at various pH values with immersion time of 3 min under room temperature

4.1.3 The effects of temperature

To study the effects of bath temperature on the performance of the Mn-P coating, AZ31B alloy samples were coated under three different temperatures (20, 50, and 75 °C), at pH 3.0 and immersion time of 10 min. The results of the coating microstructure analysis and potentiodynamic polarization tests are given in Figure 4-7 and Figure 4-8, respectively. It can be clearly seen from Figure 4-7 that higher bath temperature damaged the coating. At 20 °C, a continuous coating with only shallow cracks formed on the sample surface. In contrast, as the solution temperature increased to 50°C, a few large cracks appeared in the coating that became the passageways for corrosive ions to penetrate the coating. Furthermore, when the temperature went up to 75°C, cracking in the coating became much more severe. However, the coating thickness seemed to also increase with the rising temperature. As reactions (4-5) and (4-6) are endothermic, higher temperature accelerated this process and hence improved the coating thickness.

The results of the potentiodynamic polarization tests to some extent validated this hypothesis. As can be seen from the Figure 4-8, the coating obtained at room temperature displayed the highest corrosion potential and lowest corrosion current owing to its dense and crack-free microstructure, which was in accordance with the expectation. The corrosion current of the coating obtained at 75 °C with large cracks was lower than that of the coating obtained at 50 °C with much smaller cracks.

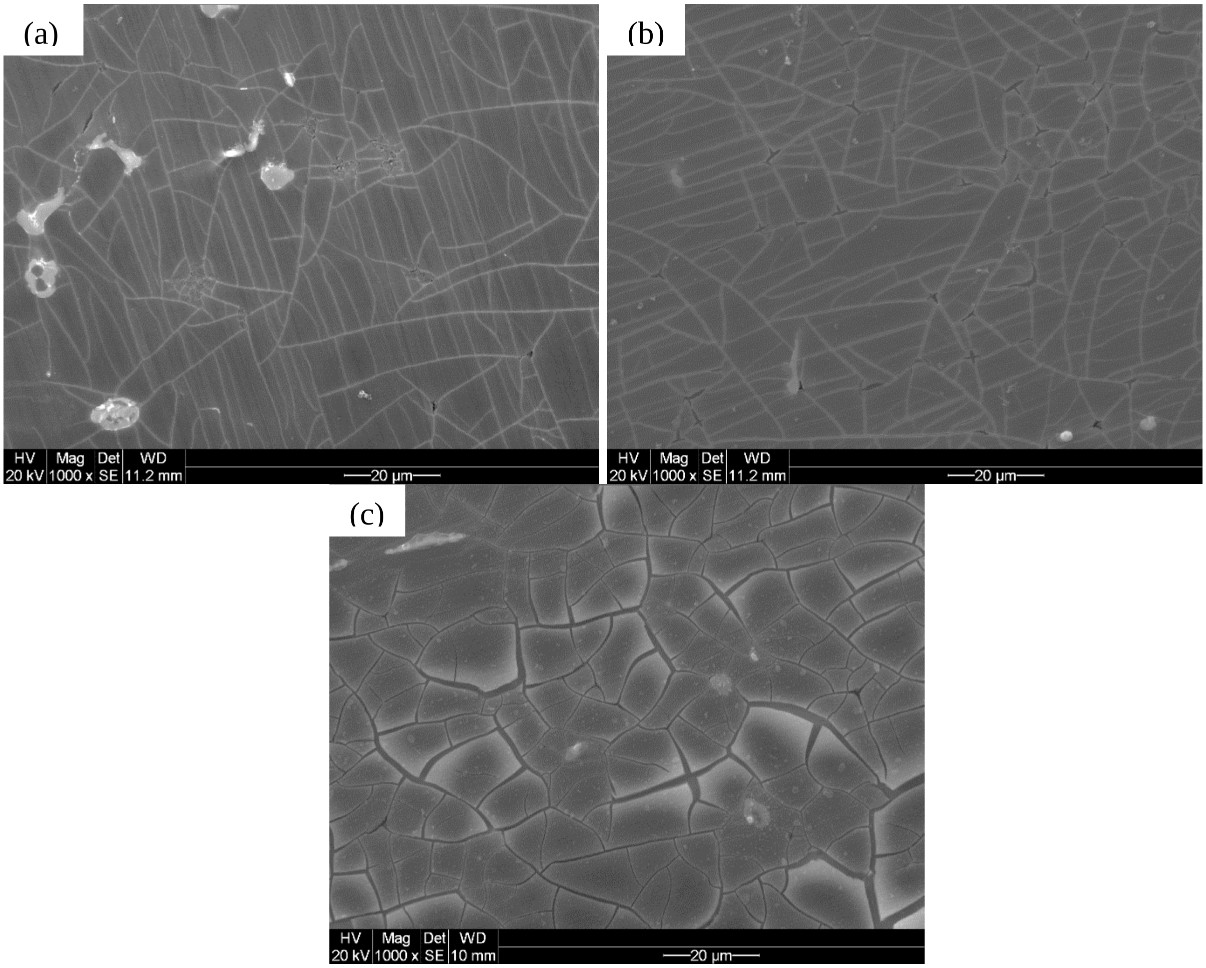

Figure 4-7 The SEM images of surface morphology of coatings obtained under various temperatures at bath pH 3.0 and immersion time of 10 min: (a) room temperature; (b) 50℃; and (c) 75 ℃

To sum up, the increase in immersion time and bath temperature both led to an increase in the coating thickness, which means enhancement in corrosion resistance. However, serious cracks in the coating were also induced during drying process with the rising coating thickness. Therefore, a compromise between the coating thickness and coating quality, especially the extent of cracking, is needed to identify the optimum bath temperature. Note that since the increase in immersion time and bath temperature both promote the growth of thick coatings there may exist more than one set of optimal coating processing conditions. In other words, similar coating thickness and quality can be achieved via the combination of a shorter immersion time with a higher bath temperature or a longer immersion time with a lower bath temperature. However, experimental trials have shown that it is quite difficult to achieve the fine balance between various factors and produce high quality corrosion protective Mn-P conversion coatings via a one-bath/one-stage process.

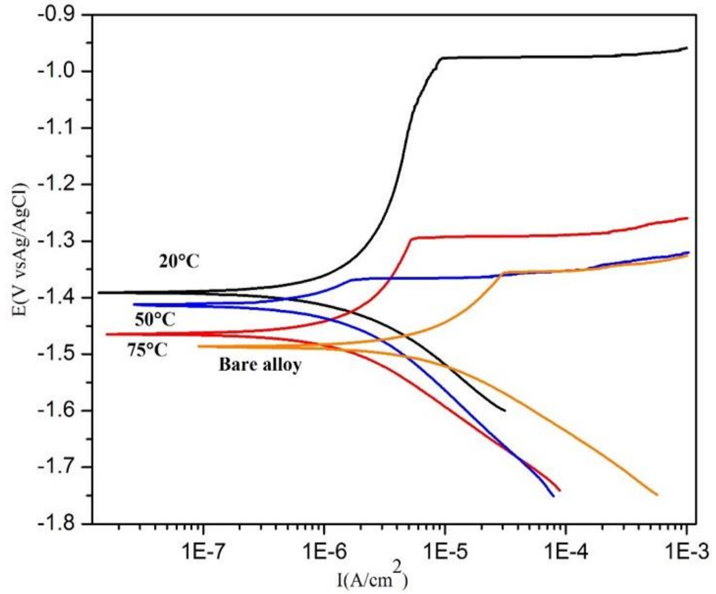

Figure 4-8 Potentiodynamic plarization curves for the bare and coated AZ31B samples treated under various temperatures at pH 3.0 and immersion time of 10 min

4.2 A novel two-stage conversion process

4.2.1 The model of a novel two-stage conversion process

Based on the above research results, a two-stage conversion coating process was proposed to deposit the Mn-P coating with large thickness, high compactness, and less cracks on the surface of Mg alloy AZ31B. The procedure of this conversion coating process is described as follows: (a) immerse the bare alloy first into a low-pH bath (1.8 for this study) for 65-75 s (Low pH treatment), in which process the bare alloy would be covered by a layer of Mn-P coating with high thickness and a few large cracks; (b) then, after washing in pure water, put the same sample into another solution with high pH value (3.0 for this study) for 10 min (High pH treatment). In the 2nd bath treatment, another thin and dense coating will be deposited on top of the thick coating formed in the first step. These two steps are both processed at room temperature. Through this two-stage conversion process, a thick Mn-P coating with few large cracks and good compactness is expected to be formed on the surface of Mg alloy AZ31B, as illustrated in Figure 4-9. The following section is going to present the characterization results of the coating produced via this two-stage conversion process

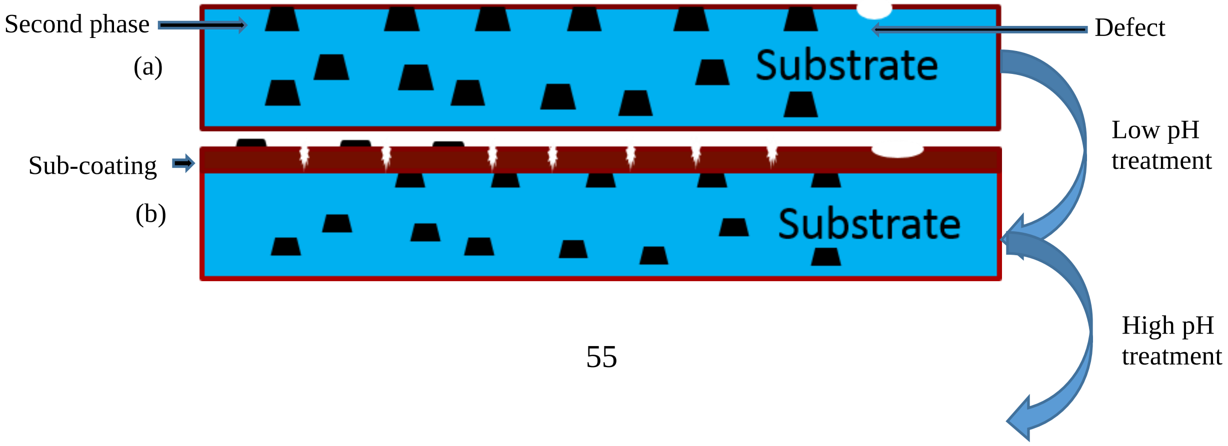

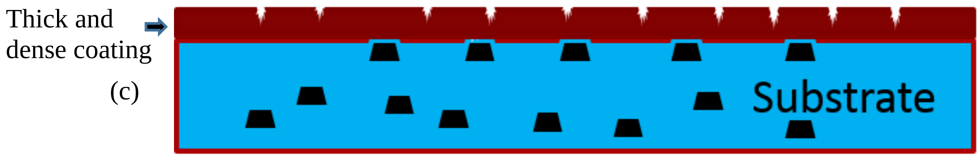

Figure 4-9 Schematic forming procedure of the Mn-P coating obtained by a two-stage conversion coating process: (a) the bare Mg alloy after cleaning pretreatments; (b) after Low pH treatment (LP coating); and (c) after High pH treatment (HP coating).

4.2.2 Characterization of the two-stage conversion coating

Figure 4-10 shows the SEM images of the surface morphology of the bare and coated AZ31B specimens treated via the two-stage conversion coating process. Images of the two coatings obtained via a low pH treatment only (Figure 4-10 (b)) and a high pH treatment only (Figure 4-10 (c)) are also presented for comparison. In general, all the coatings displayed very similar surface morphology with networks of shallow cracks except that some cracks in the two-stage coating was slightly wider (Figure 4-10 (d)). EDS analysis data (Table 4-1) suggested that the second phase particles in the AZ31B Mg alloy were oxidized after the conversion coating process, as shown in the Table 4-1. And it can be seen from Figure 4-10 that more oxidized second phase particles were seen in the coating from the high pH treatment (HP coating) than in the coating from the low pH bath (LP coating). The fact that the second phase particles can be seen on the coating surface indicates that the coating was quite thin. The most interesting aspect of the EDS results is that some manganese oxides were also detected in the two-stage conversion coating (spot D in Figure 3-10d). Manganese oxides (MnO/MnO$_2$) are generally more corrosion resistant than MgO and Al$_2$O$_3$ [51]. Therefore, this two-stage conversion coating process has the potential to produce Mn-P coating of enhanced corrosion resistance, as compared to a single-stage conversion coating process. Additionally, the thickness of each type of coating could be evaluated from the weight gain of the coated samples, as presented in Figure 4-11. It is distinctly demonstrated that the two-stage conversion coating had the highest thickness and the HP coating film was the thinnest, indicating that the two-stage conversion coating process can be used to grow thick and corrosion resistant Mn-P coating on Mg alloys.

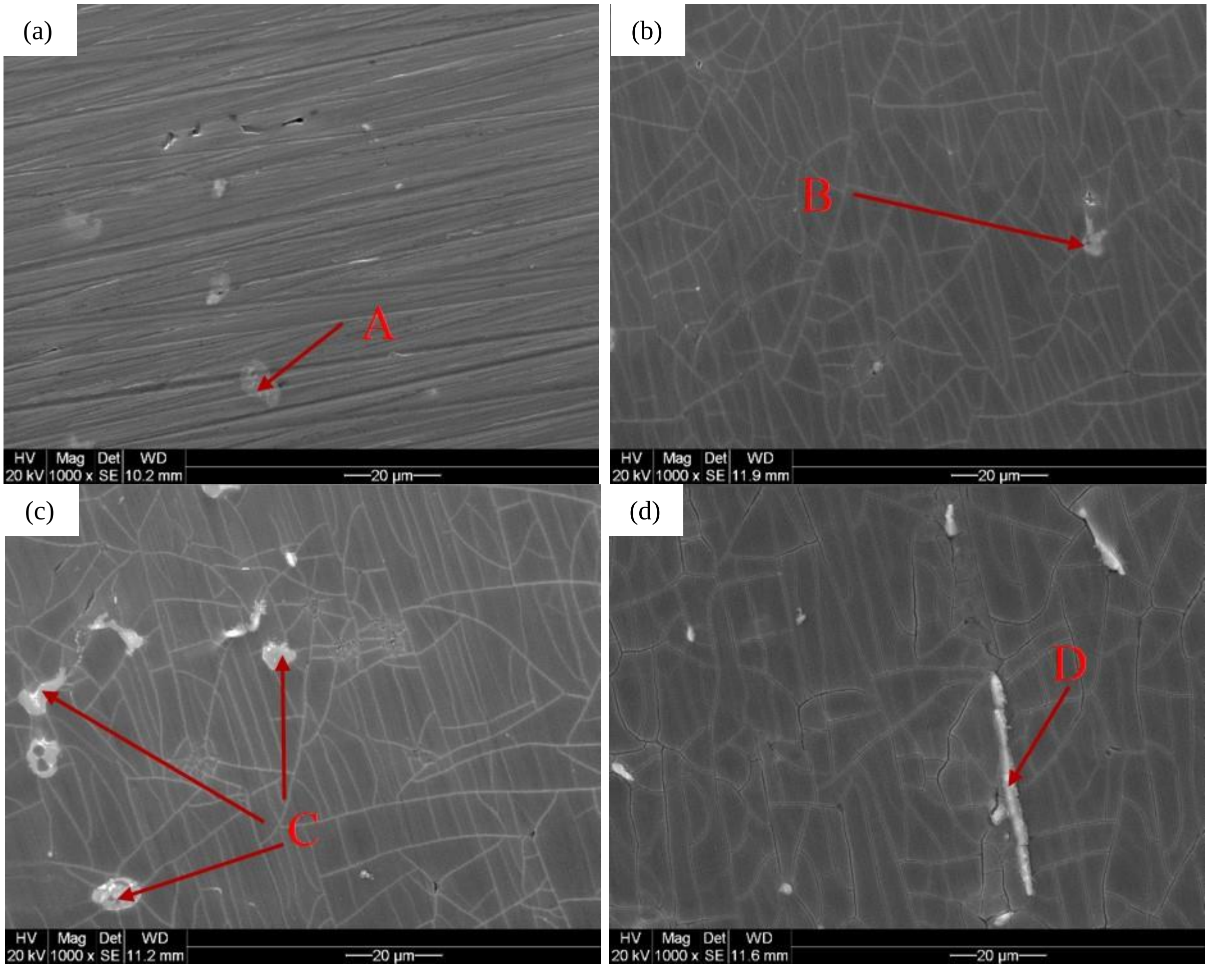

Figure 4-10 The SEM images of surface morphology of the (a) bare alloy and coatings obtained via the (b) low pH treatment (LP coating), (c) high pH treatment (HP coating), and (d) two-stage conversion treatment.

Table 4-1 Chemical composition (atm.%)of the compounds indicated in Figure 4-10

Spot	Mg	Al	Zn	Mn	O
A	90.65	6.88	2.47	/	/
B	90.50	3.69	3.81	/	2.00
C	67.64	19.01	12.18	/	1.16
D	50.45	9.45	2.31	25.04	9.79

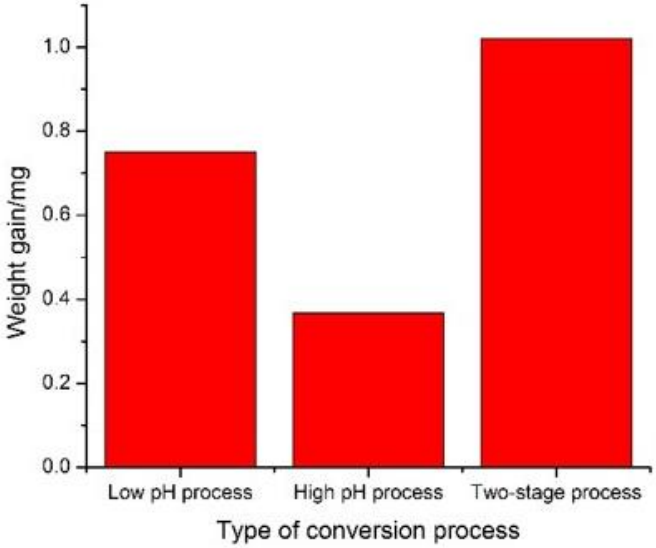

Figure 4-11 Weight gain of the samples after being treated by various conversion coating processes

4.2.3 Electrochemical test

Figure 4-12 shows the potentiodynamic polarization curves of the various conversion coated AZ31B specimens in 3.5 wt.% NaCl solution. As can be seen in the figure, the polarization curves of the conversion coated specimens shifted toward the lower current direction (left) significantly compared to that of the bare alloy, indicating that both the anodic and cathodic reactions were inhibited and hence the corrosion resistance of the AZ31B was effectively improved by the conversion coating. Moreover, it can be observed that a passive region (where a low corrosion current density was achieved between the active oxidation region and the breakdown potential E_{break}) occurred in the anodic polarization branch of the coated samples. Once the applied potential became more positive than the breakdown potential E_{break}, the corrosion current density increased rapidly. Among all coated samples, the HP coating exhibited the largest passive region. From the polarization test results we can see that the HP coating and two-stage coating showed similar corrosion behavior, and both were more corrosion resistant than the LP coating.

Electrochemical impedance spectroscopy (EIS) was then used to further study the corrosion resistance of the coated samples. As can be clearly observed from the Bode plots (Figure 4-13) of various conversion coatings and the bare alloy, the two-stage conversion coating exhibited the highest impedance values in the low frequency range. The impedance is a measure of the ability of a circuit to resist the flow of electrical current. Electrochemical impedance is measured by applying a small AC potential excitation to an electrochemical cell and then measuring the current through the cell. The Randles cell, consisting of a solution resistance R_s, a double layer capacitor C_{dl}, and a charge transfer R_{ct} or polarization resistance R_p, is one of the most common cell models that are used to represent an electrochemical system [142]. Figure 4-14 shows the equivalent circuit simulation of the bode plot for the two-stage conversion coating. R_c and

Q_c represent the coating resistance and capacitance, respectively. Higher impedance in the low frequency range suggests a higher charge transfer or polarization resistance, and thus better corrosion resistance. Therefore, from the EIS point view, the two-stage conversion coating shows the best corrosion resistance.

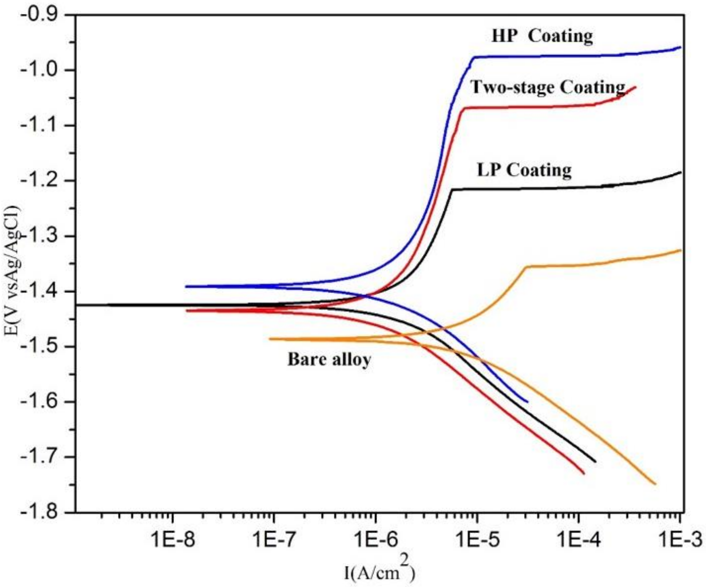

Figure 4-12 Potentiodynamic polarization curves of the bare alloy and various conversion coated samples

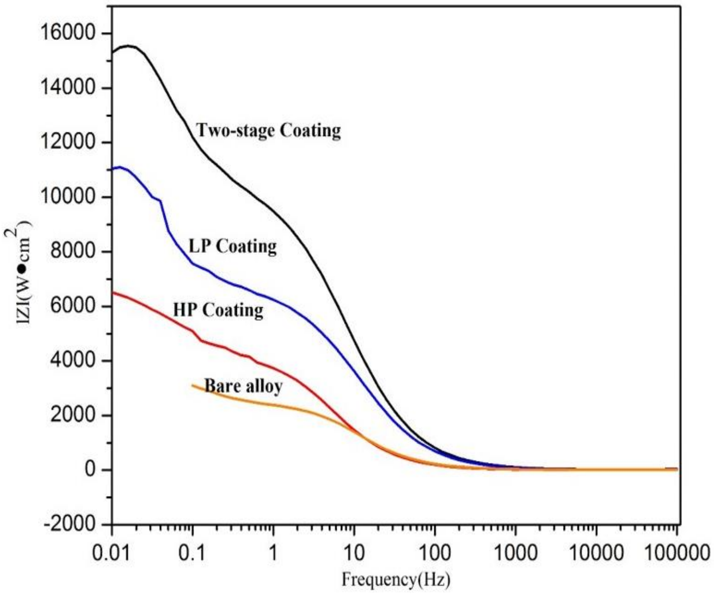

Figure 4-13 EIS data in the form of Bode plots for the bare alloy and various conversion coated samples

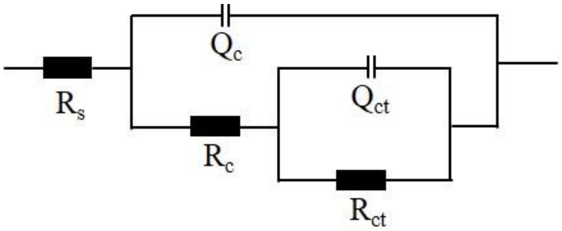

Figure 4-14 Equivalent circuit model for the simulation of the bode plot of the two-stage conversion coating

4.2.4 Salt spray test

To characterize long-term corrosion performances of the coated specimens, salt spray chamber test according to SAE J2334 standard [140] was conducted for up to 168 hrs. By visual examination of the conversion coated and the bare alloy samples as shown in Figure 4-15, we observed that after 96 hours of test the main corrosion mode for the bare alloy specimen was general corrosion, while only some corrosion pits were seen on the surface of LP coated and HP coated samples. In particular, only several small corrosion pits were found on the surface of the two-stage conversion coated specimen after 96 hours. Furthermore, as the testing duration went up to 168 h, much worse general corrosion occurred on the bare alloy and corrosion pitting on the LP coated and HP coated coupons became more severe with an increased number of pits. In contrast, the corrosion of the two-stage conversion coated coupon did not deteriorate so much with the increasing testing time. The average corrosion pit depth for the bare alloy and various coated samples were presented in Figure 4-16. Again, it can be clearly seen that the two-stage conversion coating had the least corrosion pit depth at almost every testing time point as compared to the other two coatings. With dense microstructure and a larger thickness, the two-stage conversion coating is more resistant to breaking down caused by the penetration of corrosive species to the substrate. Interestingly, from the perspective of corrosion pit depth, the bare alloy seems to exhibit similar good performance to the two-stage conversion coating. This may attribute to the uniform oxidized film formed on the surface of the bare alloy during the corrosion. If corrosion pits can act as a stress raiser to initiate the corrosion fatigue crack propagation, it seems that there may be no big difference in the corrosion fatigue crack initiation time and corrosion fatigue life between the bare alloy and the two-stage conversion coated alloy sample. Thus, in order to enhance the corrosion fatigue life of the Mg alloy, it is necessary to use a topcoat on the conversion coating to provide further corrosion protection. In addition, the corrosion products that covered the corrosion pits were analyzed using XRD and it turned out that most of them was $Mg(OH)_2$, as seen in Figure 4-17. Considering the chemical composition of the surface coating, this product may arise from the coating or the corrosion of the Mg substrate or both. No peaks for phases such as $Mn_3(PO4)_2$ or metal oxides were found in the XRD data of corrosion products. This may be attributed to the low content of elements P and Mn, as shown in Figure 4-1 (m).

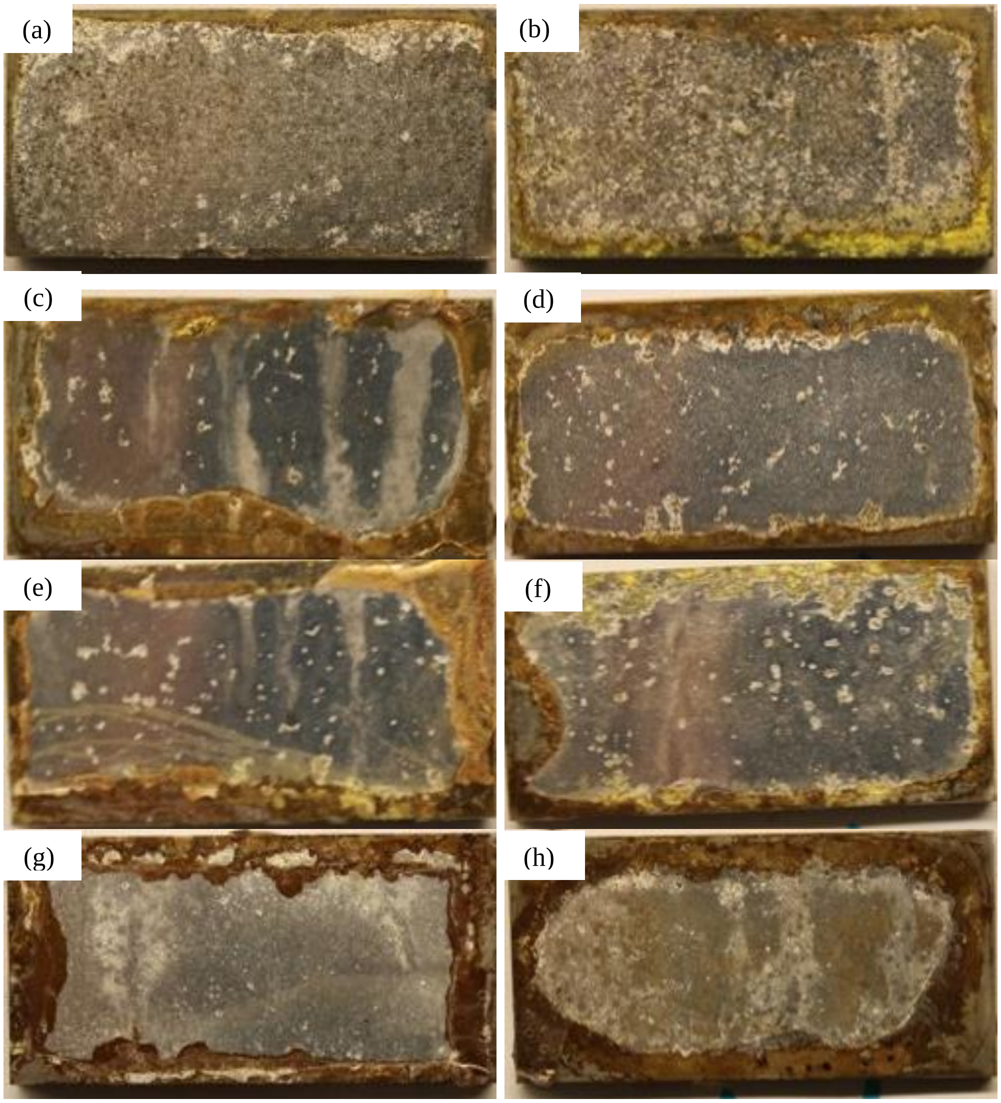

Figure 4-15 Optical images post salt spray test of the bare alloy and various conversion coated samples: (a)(b) bare alloy; (c)(d) LP coating; (e)(f) HP coating; (g)(h) Two-stage coating. (a)(c)(e)(g): tested for 96 hours; (b)(d)(f)(h): tested for 168 hours.

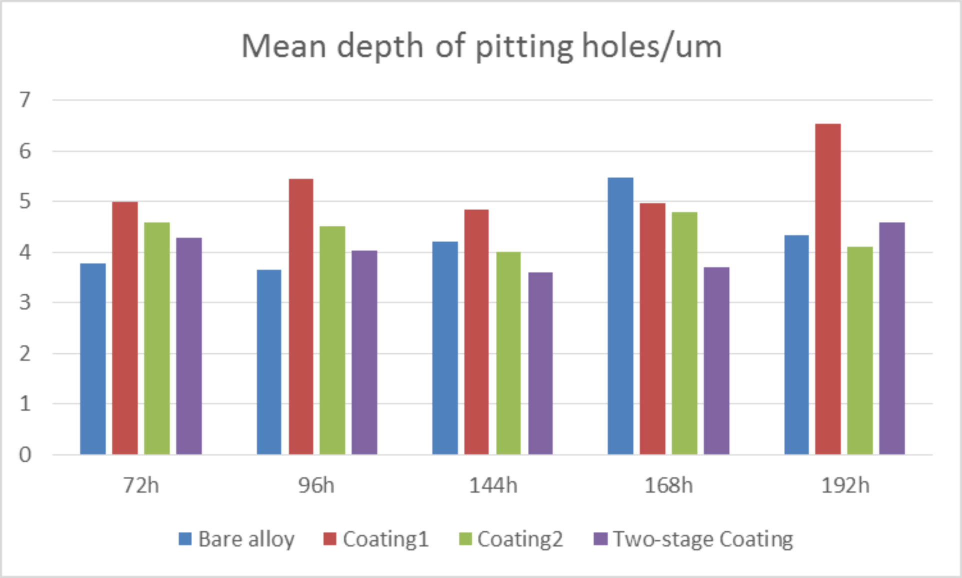

Figure 4-16 The results of corrosion pit depth measurement for the bare alloy and various conversion coated samples. Coating1: LP coating; Coating2: HP coating.

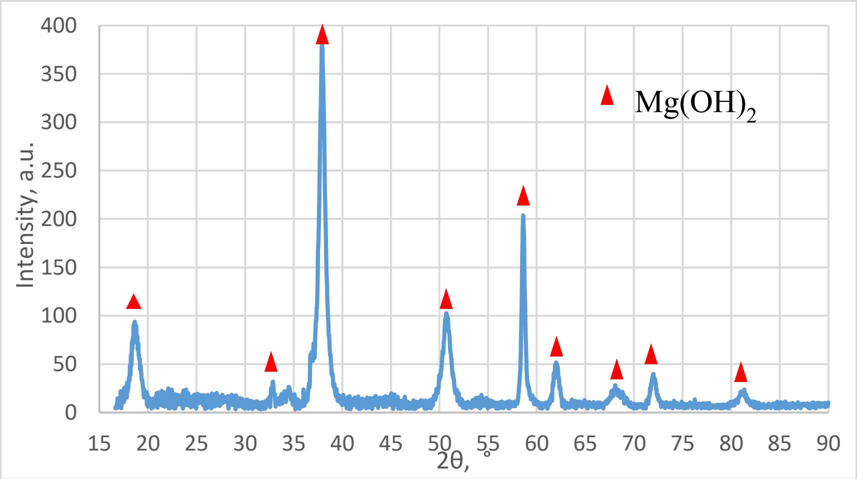

Figure 4-17 XRD diffraction pattern for the corrosion products from the AZ31B sample after salt spray testing

4.2.5 Corrosion fatigue test

Corrosion fatigue test results for various coated samples in 3.5% NaCl are shown in Figure 4-18. The fatigue test result of bare AZ31B in air was also included for comparison. It can be seen that the effects of E-coat and Mn-P+E-coat on the fatigue life of the Mg alloy specimens in the corrosive environment became increasingly evident with the decreasing stress amplitude using the S-N curve of the bare alloy as a baseline. This means that the stress factor dominates the corrosion fatigue life and the effect of the corrosion factor is insignificant in the high stress region. While in the low stress region (below 80 MPa), corrosion plays an important role in determining the fatigue life of the metal. Good corrosion protection can significantly improve the fatigue life of the Mg alloy in the corrosive environment. Because only one valid set of data is available for Mn-P coating (limitation of available samples), the effect of Mn-P coating plus E-coat cannot be clarified here. But it can be deduced that this two-stage conversion coating plus E-coat significantly improved the fatigue life of AZ31B in 3.5% NaCl solution. Lastly, it can be noted that even with the protection of surface coatings, the fatigue life of AZ31B in 3.5% NaCl under most of the stress levels was still not as good as that of the bare alloy in air. This is probably due to certain reasons such as the mismatch of mechanical strength and other properties between the coating and the alloy, the weak adhesion of the coating, and insufficient protection against corrosion in the salt solution provided by the surface coatings.

Overall, from the results of the electrochemical tests, salt spray chamber tests, and corrosion fatigue tests, it can be concluded that the two-stage conversion coating process was able to provide a thick and dense coating for the AZ31B Mg alloy with better corrosion resistance than the coatings obtained via a single conversion coating process (LP coating and HP coating).

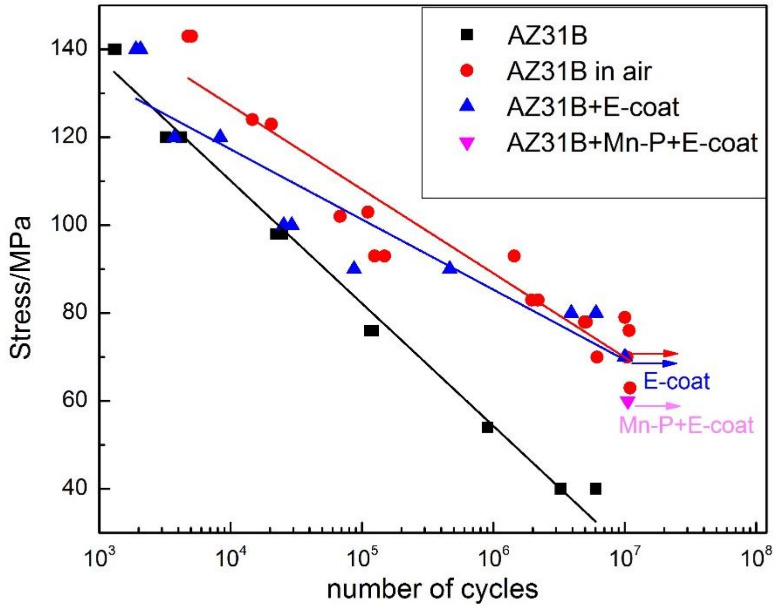

Figure 4-18 Corrosion fatigue test results in 3.5% NaCl for various coated AZ31B and fatigue test data for the bare AZ31B specimens

4.2.6 Summary

A two-stage conversion coating process, namely, the treatment in a low pH solution followed by an immediate treatment in a high pH solution, was developed to deposit a thick and dense protective surface coating on Mg alloy AZ31B. Results of the SEM analysis, electrochemical testing, and salt spray chamber tests exhibited that the two-stage conversion coating had better corrosion performances than either of the two types of single-stage conversion coating (LP and HP coatings).

Chapter 5 Evaluation of corrosion protection methods

One of the objectives of this research is to produce a robust coating system on the Mg alloys for corrosion protection [43]. A topcoat, as a part of a typical coating system, is almost always necessary to achieve a high-quality surface finish of Mg parts. E-coating and powder coating were both brought into this research to investigate their effectiveness on protection of the Mg alloys. In addition to the Mn-P conversion coating developed in this work, the chromate conversion coating and micro-arc oxidation (MAO) coating that were studied by another student Yuna Xue [146] in our group were also introduced in this chapter for assessing the efficacy of various corrosion protection methods for different Mg alloys. Table 5-1 listed all the investigated base materials and corresponding coating system. Salt spray test and scribe test were used to characterize their corrosion performance and SEM/EDS for the cross-section microstructure. The weight loss of each sample from salt spray tests was also measured.

Table 5-1 The investigated base material and corresponding coating system for corrosion performance evaluation

Base material	Surface treatment	Topcoat
AZ31B C*[1]	None	E-coating
	Mn-P	E-coating
AZ80 C	None	E-coating
	Mn-P	E-coating
ZK60 EF*[2]	CCC	Powder coating1 (P1)
ZK60 EF	MAO	Powder coating2 (P2)
AZ80 EF	MAO	Powder coating2

Notes: *[1] C: cast alloy, *[2] EF: extrusion/forged at 250℃

The corrosion properties of the three investigated Mg alloys were studied by Yuna Xue [147] in our group. As she explained, a amount of Al content in AZ80 leads to the formation of a continuous network β-phase ($Mg_{17}Al_{12}$) along the boundaries of α-matrix grains that can act as a corrosion barrier, which make it more corrosion resistant than AZ31. Similarly, a continuous network of β-phase ($MgZn_2$) is formed in the α-matrix of ZK60, which can as well server as a corrosion shelter. Moreover, the electrode potential of $MgZn_2$ is higher than that of $Mg_{17}Al_{12}$, so ZK60 shows better corrosion performance than AZ80. Briefly, the corrosion resistance increases in the order of ZK60>AZ80>AZ31.

5.1 The coating system with E-coating as a topcoat

E-coating as a topcoat is commonly used for surface finish of Mg parts in vehicles. This cost-effective surface technique capable of coating complex components attracted our first attention. Considering the availability of E-coating facilities and expertise, we sought help from a local company, MetoKote (Cambridge, Ontario) for applying E-coating on our Mg alloy specimens. Figure 5-1 gives an example of the cross-sectional microstructure of the E-coating on the MAO coated AZ31B alloy [146][148]. It can be evidently seen that the coating system comprised of an underlayer of MAO coating and a top E-coating. The thickness of the E-coating was about 27 μm.

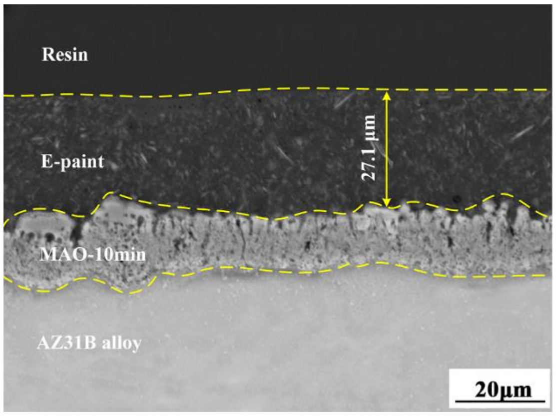

Figure 5-1 SEM image of cross-sectional microstructure of the E-coating (E-painting) on the MAO coated AZ31[148]

The Mn-P conversion coating process developed on AZ31B alloy was utilized to treat AZ80 alloy [149]. For comparison, the base material with the E-coating alone was also tested. Figure 5-2 shows the optical images of the Mg alloys specimens with various coatings (AZ31B+E-coating, AZ31B+Mn-P+E-coating, AZ80+E-coating, and AZ80+Mn-P+E-coating) prior to and post the scribe test and salt fog (5.0% NaCl) corrosion test (ASTM B117) for 7 days. The E-coating were uniformly deposited on all the substrates with or without Mn-P conversion coating (Figure 5-2(a-d)). However, after testing for 7 days in the salt fog, with corrosion initiated from both the scribe line and the edge of the samples, all the samples corroded to varying degrees (Figure 5-2(e-h)). The scribe line exposed the substrates underneath the protective coatings to the corrosive medium, thus corrosion propagated easily around the scribe line. The edges of the sample were also weak areas susceptible to corrosion initiation because it is difficult to obtain uniform coatings in these locations. Specifically, the AZ31B+E-coating specimen (Figure 5-2(e)) exhibited the most severe corrosion among all tested samples with most of the coating peeled off around the scribed line. This clearly indicated that without the surface treatment/preparation of the Mg alloy via a conversion coating the adhesive bonding between the AZ31B alloy and E-coating is rather weak, and thus insufficient corrosion protection is attained. When the Mn-P conversion coating was applied on the Mg alloy as an underlayer, the adhesion of the E-coating to the substrate was improved significantly and a much better corrosion resistance was seen (Figure

5-2(f)). The test results on AZ80 alloy (Figure 5-2(h)(g)) further confirmed the necessity of a surface pre-treatment such as the conversion coating or MAO coating prior to the E-coating process to ensure strong adhesion of the topcoat and robust protection against corrosion. It is worth noting that the high surface roughness of the Mn-P conversion coating with shallow cracks (Figure 4-10) is beneficial for mechanical anchoring of the topcoat and thus would enhance the bonding the E-coat to the alloy. In addition, the corrosion properties of the Mg alloy substrate also play an important role in determining the corrosion performances of coated specimens. The coated AZ80 alloy specimens (Figure 5-2(g)(h)) apparently showed better corrosion performance than their corresponding AZ31B specimens with the same coating system (Figure 5-2(e)(f)). This is because AZ80 alloy has a much higher content of Al and thus a large amount of β-phase. Despite the fact that β-phase can act as s local cathode and increase the corrosion rate of the Mg alloy, it can also function as a corrosion barrier if the α-matrix is largely covered by the β-phase [150][151]. AZ80 alloy with the Mn-P conversion coating plus an E-coating showed the best corrosion performance among all tested specimens.

Overall, the corrosion performances of coated Mg alloys are determined by combined effects of various factors including the corrosion susceptibility of the substrate, robustness and protectiveness of the surface coating, and the adhesion strength of the coating to the substrate. AZ80 shows high corrosion resistance than AZ31B alloy. The application of the Mn-P conversion coating not only provides moderate corrosion protection of the Mg alloy substrates, but also prepares the metal surface for strong adhesive bonding of the E-coating. However, the Mn-P coating does not have self-healing nature [47][67], as has the chromate conversion coating, which leads to easy propagation of corrosion along the coating/substrate interface once the coating system is damaged (i.e. scribed through). The E-coating indeed provides fairly good corrosion protection and satisfactory surface aesthetics, but considerable corrosion was still seen on the coated Mg alloys post 7-day salt fog corrosion test (Figure 5-2). Therefore, in the next stage, chromate conversion coating with self-healing ability and high corrosion resistant MAO coating plus the powder coating as topcoat were applied to the forged AZ80 and ZK60 alloys.

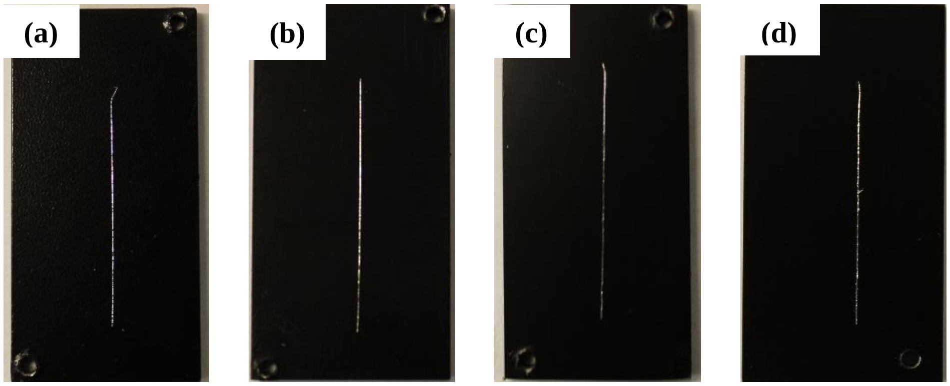

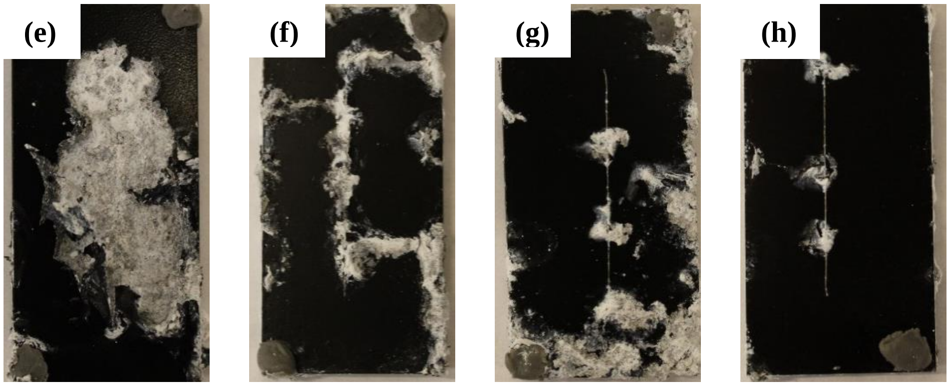

Figure 5-2 Optical images of coated Mg alloy coupons (a-d) prior to and (e-h) post the scribe and 7-day salt fog corrosion test: (a)(e) AZ31B+E-coating, (b)(f) AZ31B+Mn-P+E-coating, (c)(g) AZ80+E-coating, and (d)(h) AZ80+Mn-P+E-coating.

5.2 The coating system with powder coating as a topcoat

Figure 5-3 gives the SEM images of the cross-sectional microstructure of the CCC coated ZK60, MAO coated ZK60, and MAO coated AZ80 with a topcoat of powder coating (It is noteworthy to mention that no CCC coated AZ80 specimen is presented because the CCC processing developed for ZK60 did not work for AZ80 alloy). It can be clearly seen that the coating system consisting of two dense and uniform layers were formed on all three Mg alloys. The EDS analysis data (Figure 5-3(d)) for point 1 (CCC on ZK60) in Figure 5-3(a) revealed that the CCC layer was mainly composed of elements Mg, O, Cr, and Mn. Similarly, the elemental composition of the MAO coating investigated in this research is mainly Si, F, O, and Mg, as shown in the EDS analysis results (Figure 5-3(e)) of the points 2 and 3 in Figure 5-3(b)(c). Further analysis for possible phases in these undercoats could be found previous literature and in Yuna Xue's work [148]. On the other hand, the sole EDX analysis for these undercoats are to ensure that the coat system is indeed composed of two layers and the undercoats (i.e. CCC and MAO) were not removed during the subsequent powder coating process. The average thickness of the powder coating in Figure 5-3(a), (b), (c) are 53.8µm, 48.7µm, and 63.2µm, respectively. They are roughly two times thicker than that of the E-coating. The thickness of the CCC, P1, and P2 are 10.2µm, 12.8µm, and 9.0µm, respectively.

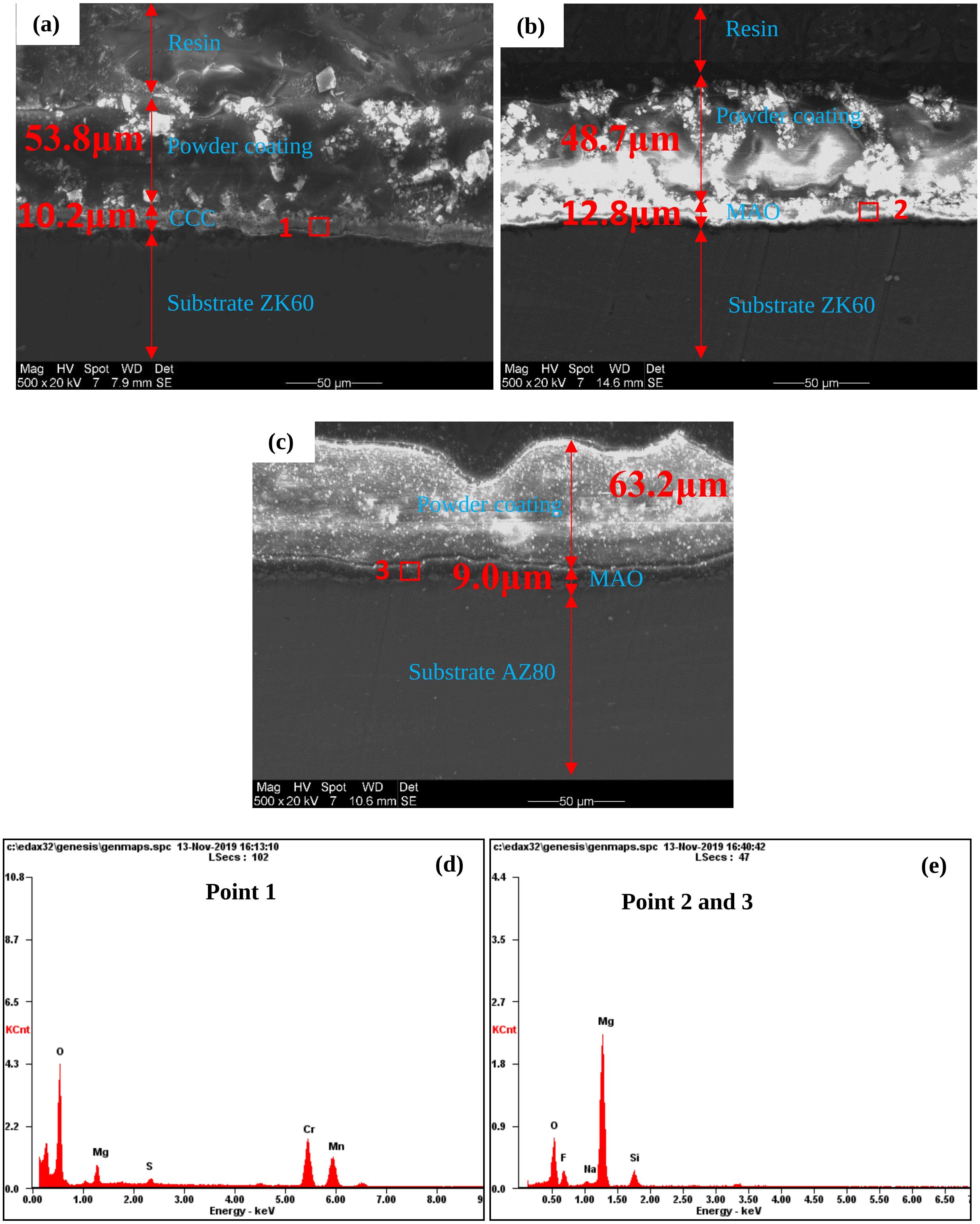

Figure 5-3 SEM images of cross-sectional microstructure of the (a) CCC coated ZK60, (b) MAO coated ZK60, and (c) MAO coated AZ80 with a topcoat of powder coating; and EDS results for the selected areas: (d) point 1 and (e) points 2 and 3.

Salt spray test as per SAE J2334 standard was conducted to characterize the corrosion performances of the three Mg alloys with different coatings. Figure 5-4 shows the optical images of the coated coupons that were tested for 7, 14, 21, 28, 35, 42, 63, and 77 days. At each time point, two repetitive specimens of each type were taken out of the salt spray chamber for observation and weight loss measurement. As can be seen from Figure 5-4(a1) (b1) (c1), after 7 days of salt spray test all the coated sample surfaces remained intact. After 14 days of salt spray, there was still no signs of corrosion on all the three alloy samples (Figure 5-4(a2) (b2) (c2)). As the test duration increased to 21 or even 28 days, only very limited localized corrosion occurred at the edges of the sample (Figure 5-4(b3) and Figure 5-4(a4)). When the test time extended to 35 days, we could see severe corrosion occurred on one of the two repetitive samples around the hole (needed for hanging the coupon during powder coating process) sealed by the plasticine, while the other specimen did not corrode so badly (Figure 5-4(a5) (b5) (c5)). The severe corrosion was likely caused by the bad sealing of the plasticine and could not represent the efficacy of the protective coating. Similar results were also seen in the samples tested for 42 days (Figure 5-4(a6) (b6) (c6)). Due to the shortage of specimens, no CCC coated ZK 60 specimens were tested beyond 42 days. For the MAO coated ZK60 and AZ80 specimens with powder coating, almost no corrosion was seen even after 77 days of salt spray testing, especially on the coated AZ80 coupons (Figure 5-4(b7)(c7)(b8)(c8)). The weight loss of the Mg alloy coupons per cubic centimeter as a function of the exposure time to salt spray is given in Figure 5-5. Generally, all the three types of samples showed no weight loss within the first 21 days and then some but still pretty low weight loss beyond 21 days, which is consistent with the results of the visual inspections. Specifically, the highest weight loss for the CCC coated ZK60, MAO coated ZK60, and MAO coated AZ80 with powder coating was 0.64 mg/cm^2 (after 35 days), 0.08 mg/cm^2 (after 28 days), and 0.6 mg/cm^2 (after 42 days), respectively. The results of the weight loss measurement indicated that the MAO coated ZK60 alloy with powder coating2 has the best corrosion performance.

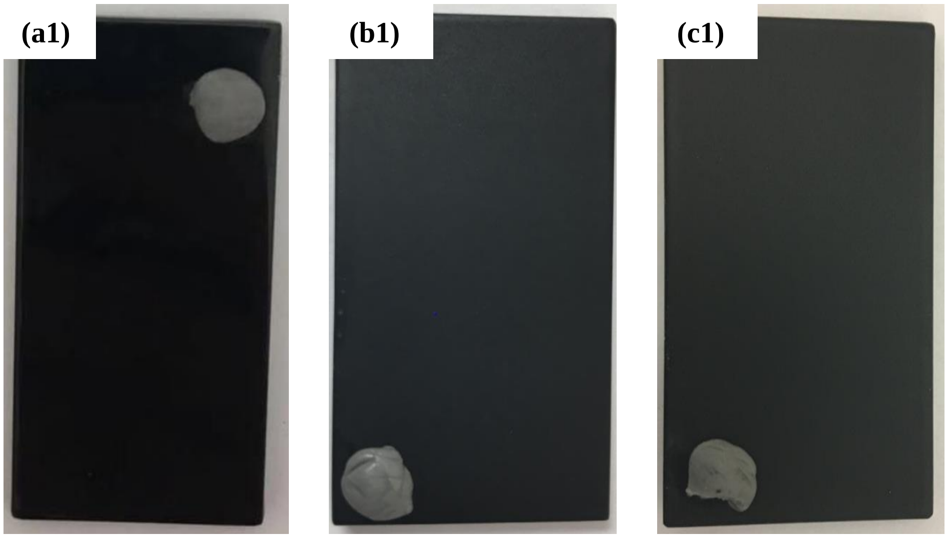

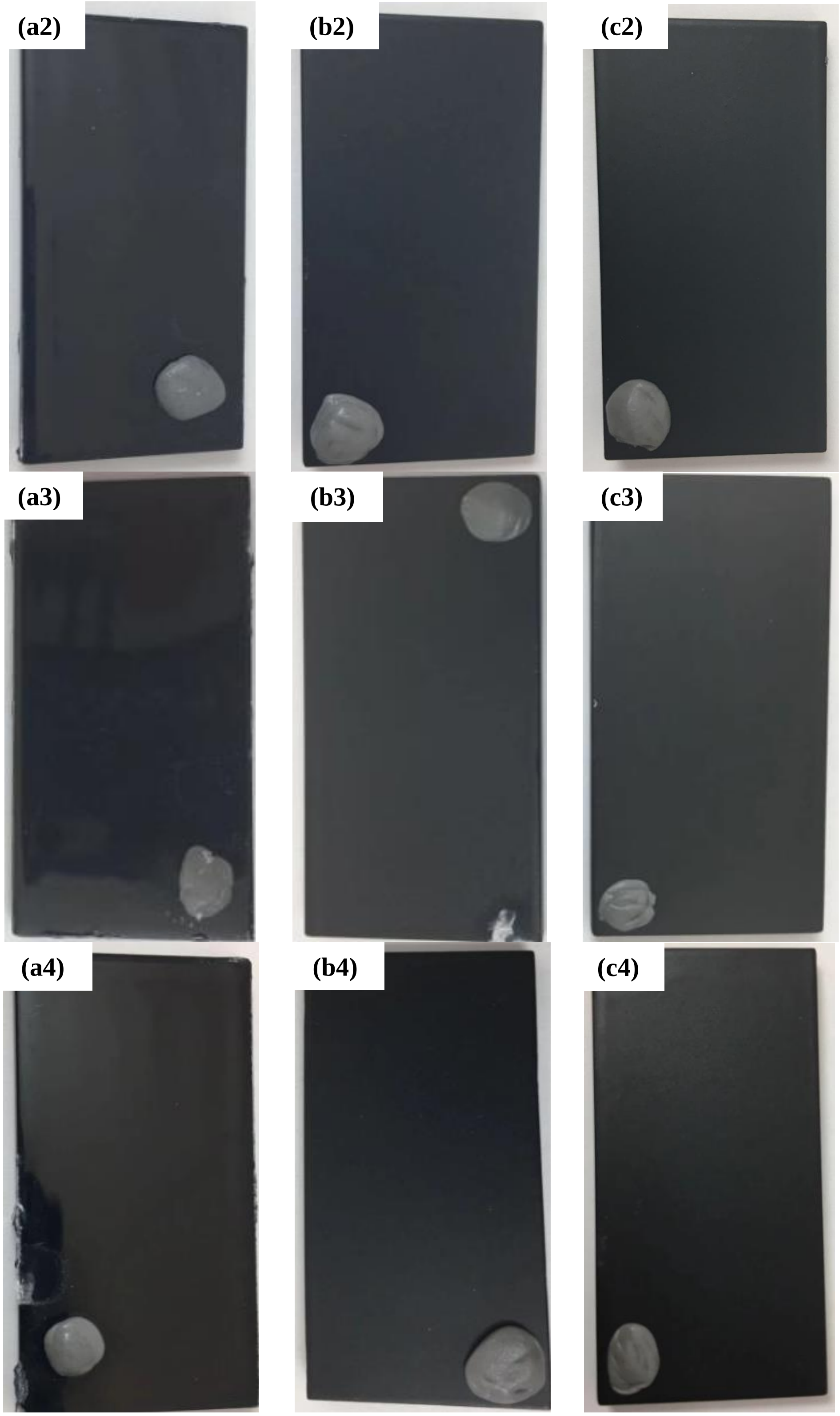
(a2)
(b2)
(c2)
(a3)
(b3)
(c3)
(a4)
(b4)
(c4)

(a5)

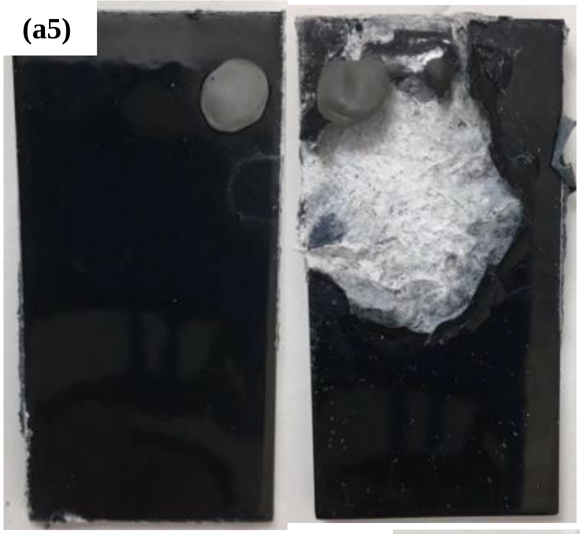

(b5)

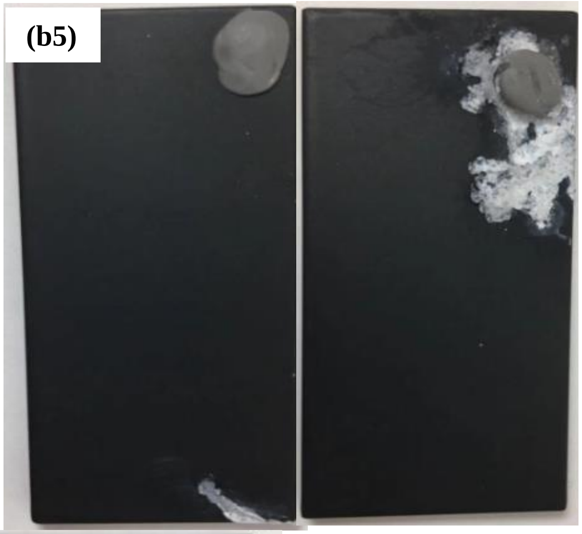

(c5)

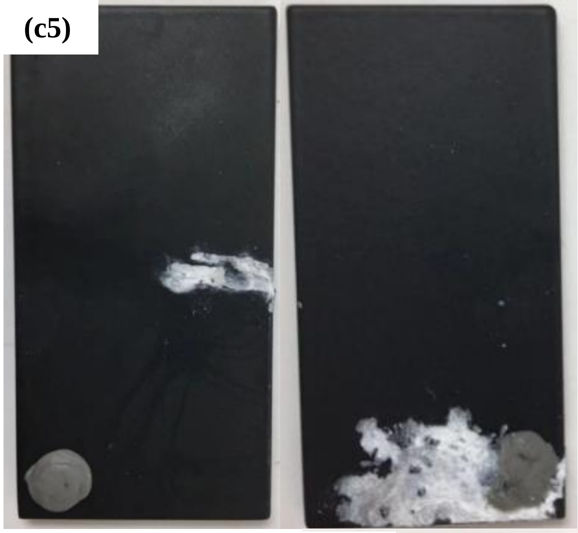

(a6)

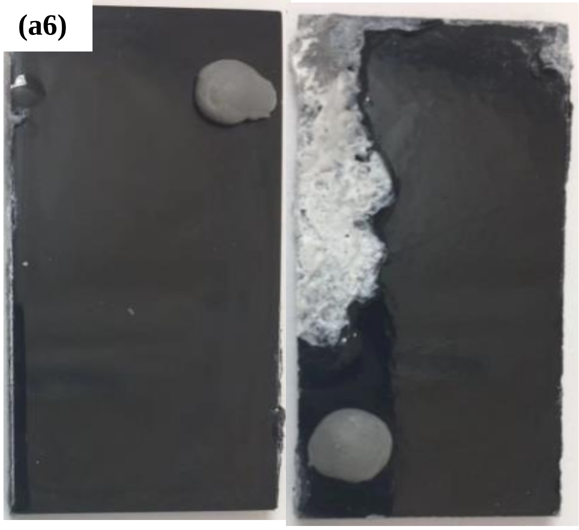

(b6)

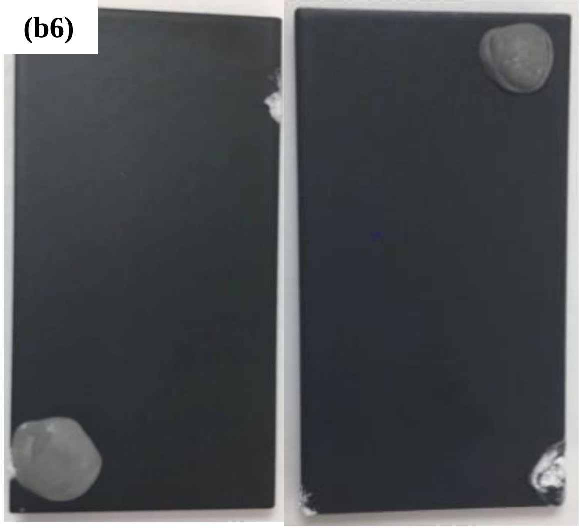

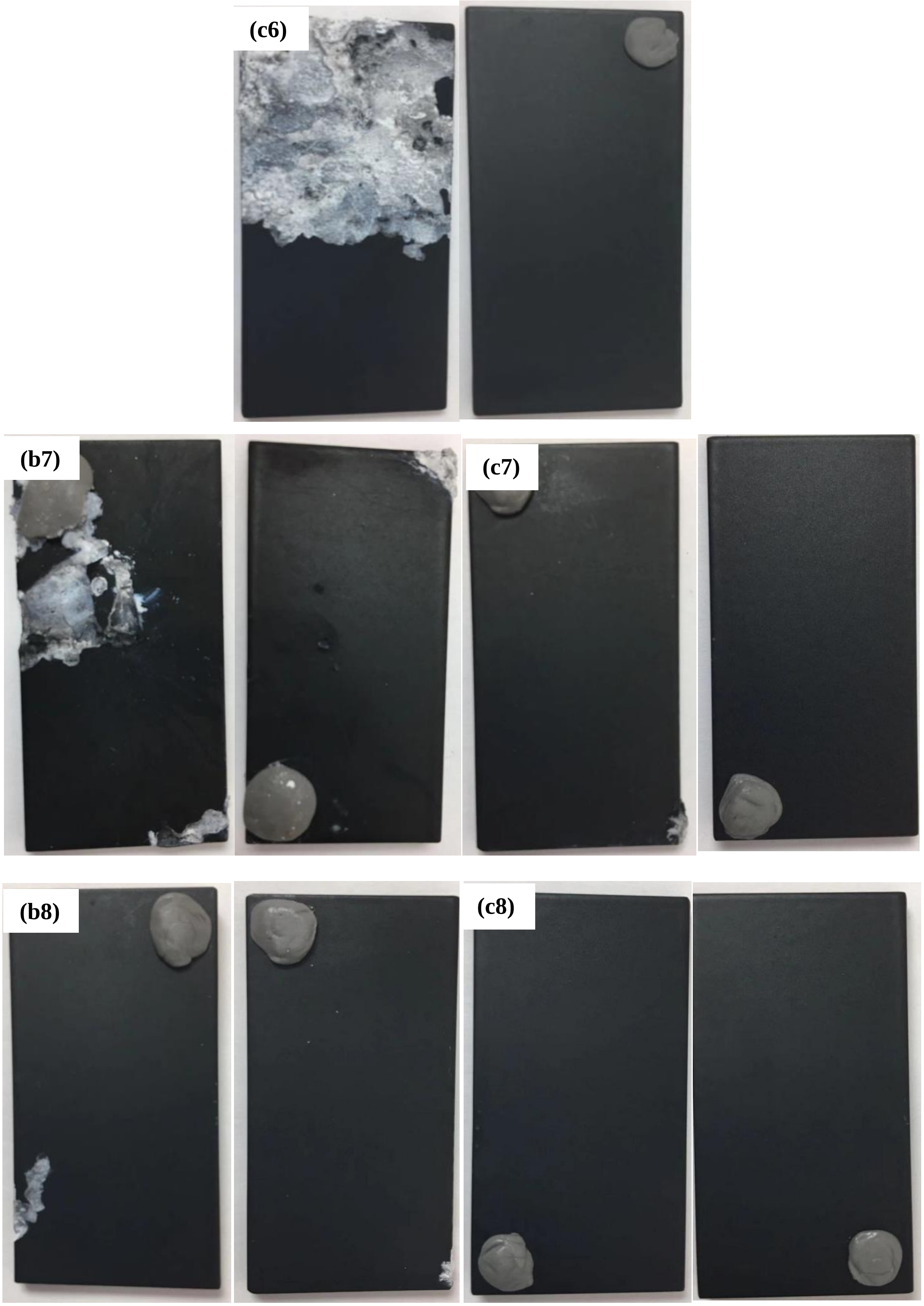

Figure 5-4 Optical images of the coated samples after salt spray test for 7 days: (a1)(b1)(c1); 14 days: (a2)(b2)(c2); 21 days: (a3)(b3)(c3); 28 days: (a4)(b4)(c4); 35 days: (a5)(b5)(c5); 42 days: (a6)(b6)(c6); 63 days: (b7)(c7); and 77

days: (b8)(c8). (a1-a6) CCC coated ZK60 with powder coating1; (b1-b8) MAO coated ZK60 with powder coating2; (c1-c8) MAO coated AZ80 with powder coating2.

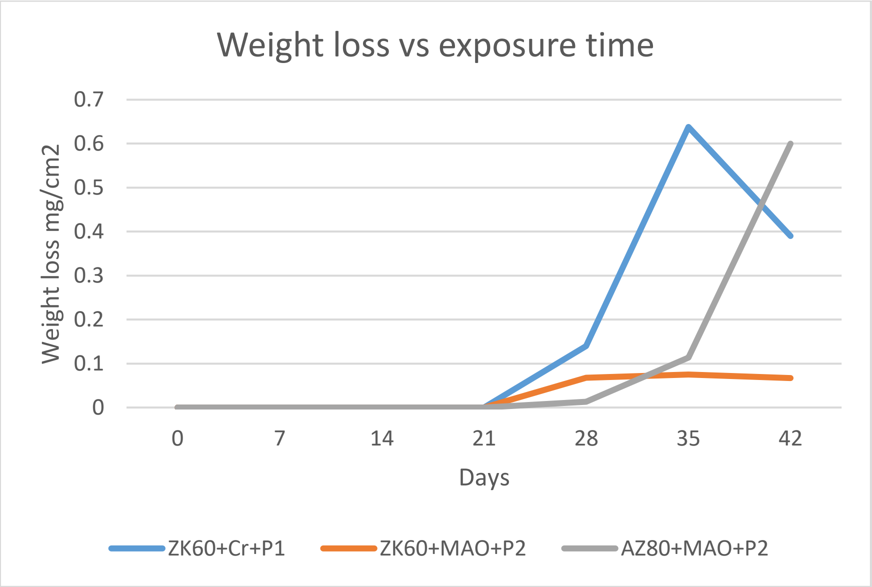

Figure 5-5 Weight loss as a function of exposure time for the three types of coated Mg alloy samples

To further characterize the adhesive property and protectiveness of the powder coating, a 0.5 mm wide scribe line was carved in the central of each sample according to standard ASTM D1654. This method uses corrosion creepage perpendicular to the scribe line as a quantitative measurement of corrosion performance. The less corrosion creep on either side of the scribe, the higher the corrosion resistance or better corrosion performance. Figure 5-6 shows the optical images of the scribed coupons exposed to 5% NaCl fog (ASTM B117) for 7, 14, 21, 28, and 35 days. It can be clearly seen in Figure 5-6(a1) (b1) (c1) that no general corrosion and no rust creepage along the scribe line occurred after testing for 7 days, which is much better than those samples with E-coating in Figure 5-2. This can be attributed to the stronger adhesion of the powder coating to the CCC and MAO coating, more robust powder coating with larger thickness, as well as the better corrosion resistance of the forged ZK60 and AZ80 substrates. When test duration goes up to 14 days, slight corrosion can be seen in localized areas, and the scribe line grew wider due to corrosion creepage (Figure 5-6(a2) (b2) (c2)). After 21 days of testing, the coated coupons started to show corrosion propagated much further from the scribe line while the width of the scribe line had little change (Figure 5-6(a3) (b3) (c3)). When the test time reached 28 days, the corrosion creepage on MAO coated ZK60 and AZ80 coupons with powder coating expanded to much larger areas and became even worse after testing for 35 days. In contrast, the CCC coated ZK60 coupons with powder coating showed much less corrosion creepage and better corrosion performance than the other two types of coated coupons (MAO coated ZK60 and AZ80 coupons with powder coating) at almost all test time points. This is probably related to the excellent self-healing ability of CCC [67], which would prevent the penetration of the corrosive species and inhibit the growth of rust creepage at the scribe line.

Overall, E-coat as a topcoat is not as effective as a powder coating in the case of the pretreated Mg alloys for corrosion protection. The best corrosion performance without a scribe was provided by the MAO-powder coating system on the ZK60 alloy while CCC-powder coating system could provide the best corrosion performance for the ZK60 alloy with a scribe. Corrosion fatigue tests were conducted by Yuna Xue for various coating systems with E-coat as a topcoat. It was found that the coating systems involving a MAO coating showed a poor corrosion fatigue resistance because of the ceramic brittle structure. More corrosion fatigue tests on other coating systems with powder coating as a topcoat needs to be further conducted.

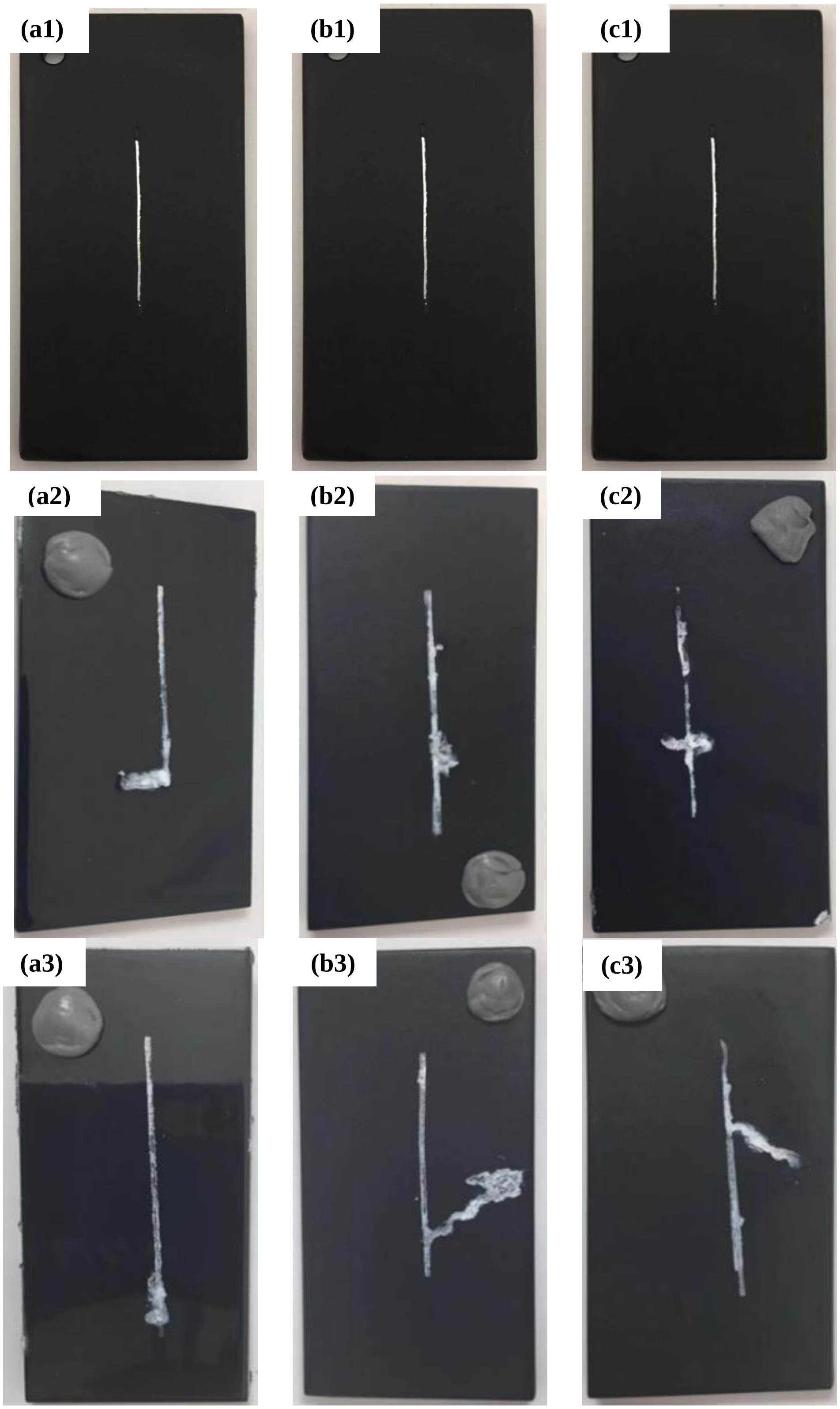
(a1)
(b1)
(c1)
(a2)
(b2)
(c2)
(a3)
(b3)
(c3)

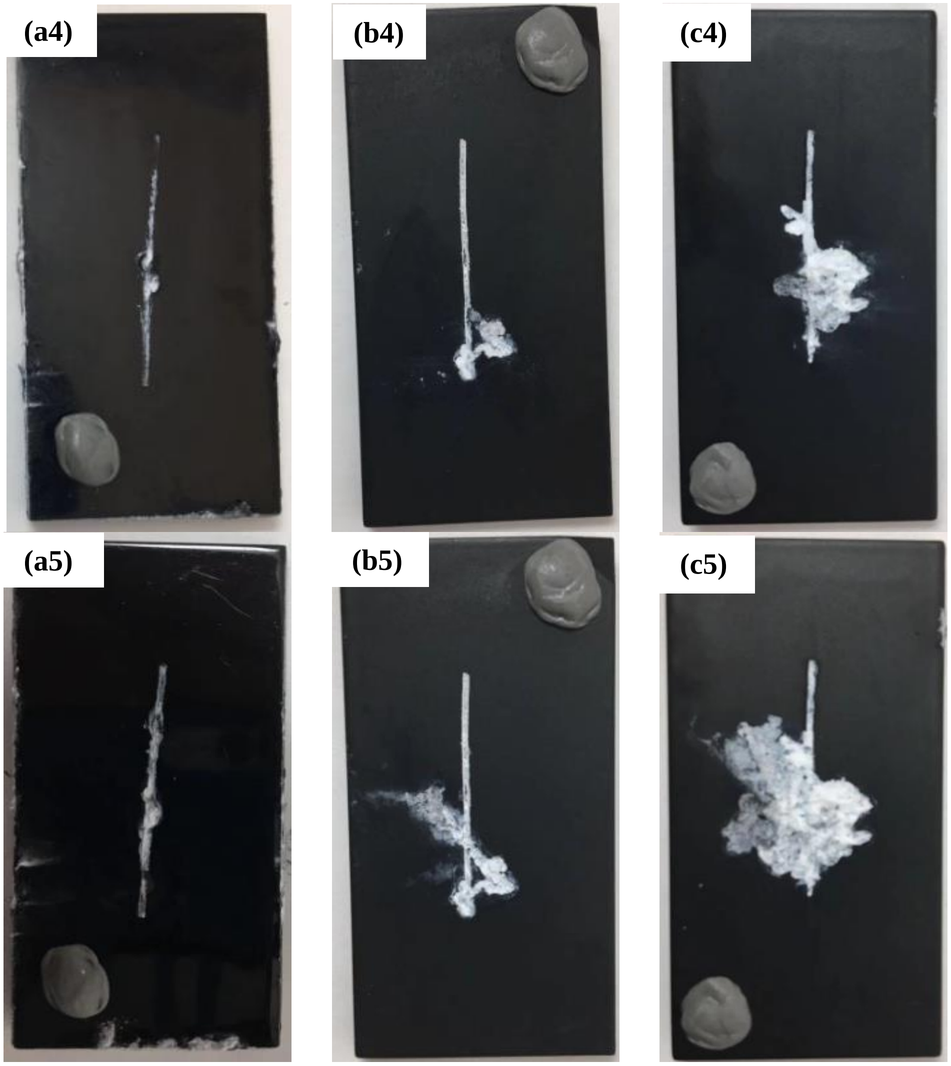

Figure 5-6 Optical images of the coated samples after the scribe and salt spray test for 7 days: (a1)(b1)(c1); 14 days: (a2)(b2)(c2); 21 days: (a3)(b3)(c3); 28 days: (a4)(b4)(c4); 35 days: (a5)(b5)(c5). (a1-a5) CCC coated ZK60 with powder coating1; (b1-b5) MAO coated ZK60 with powder coating2; (c1-c5) MAO coated AZ80 with powder coating2.

Chapter 6 Developed corrosion fatigue crack propagation model for metals

Experimental study on corrosion fatigue sometimes can be significantly time-consuming and needs well-designed experiments and specific facilities. In contrast, computational modelling can be a very convenient and efficient tool for understanding and simulating the corrosion fatigue behavior. Therefore, after identification of robust surface coating systems for the Mg alloys, the computational modelling of corrosion fatigue behavior of the coated Mg alloys has become the focus of the investigation. Currently, most of the experimental study of the corrosion fatigue of Mg alloys in literature involves rotating bending tests which produce data such a S-N curve and fatigue strength in certain corrosive environments. These data are not useful for the verification of computational model of the complex corrosion fatigue crack propagation behavior under different environmental and stress conditions. In fact, experimental investigation on the corrosion fatigue crack propagation of the coated Mg alloys is scarce. On one hand, Mg alloys are highly sensitive to the corrosive environment, which lead to the poor experiment reproducibility and scatter of experimental data. Thus, a large number of tests are required. Some tests such as the fracture toughness test as per ASTM standard E399-17 even require a sample thickness that is beyond the size of all available Mg specimens in this project. On the other hand, the existing standard testing methods are only meant for characterizing uncoated metal and thus new experimental procedures (i.e. new surface preparation process, new sample geometry, and new protocol to create pre-cracked samples etc.) are to be developed in order to effectively characterize the corrosion fatigue behavior of coated Mg alloys. To this end, the computational modelling approach was adopted and a reliable model to explain the corrosion fatigue crack propagation behavior of Mg alloys will be first theoretically discussed in this chapter.

Environmentally assisted fatigue cracking, or corrosion fatigue, has been recognized as one of the major causes for failure of various metallic engineering materials. The synergistic effect of the corrosive environment and fluctuated loading can lead to early fatigue crack initiation and enhanced FCG rate, and thus early fracture of structures and components. Considerable efforts have been made to quantitatively characterize and understand the mechanisms for corrosion fatigue for prediction of service life, design, and fatigue strength enhancements [32, 123-124, 152]. However, because of the complexity resulted from interaction in the material-cyclic loading-environment system, an accurate and reliable prediction of CFCP life still remains as a challenge.

6.1 The unified two-parameter driving force for corrosion fatigue crack propagation

An overview of the current literature suggests that the CFCG rate for a given material is influenced by three types of variables: mechanical variables (e.g. stress intensity factor range ΔK, maximum stress intensity K_{max}, stress ratio R, loading frequency f) [153], environmental variables (e.g. corrosive species, pH, corrosion potential) [154-155], geometrical variables (e.g. crack size, crack geometry) [156]. Interactions between cyclic loading and environment make CFCG rate depend not only on the elastic-plastic stress-strain state ahead of the crack tip but also on the electrochemical reactions at the crack tip [157]. As such CFCG involves a combination of a mechanical driving force and an electrochemical driving force.

It is customary to take FCG in an inert environment (termed as pure fatigue) as a reference to analyze CFCG [158]. In the analysis of fatigue, stress intensity factor range ΔK has usually been considered as its mechanical driving force, obeying Paris and Erdogan [159] CGR model:

$$\frac{da}{dN} = C(\Delta K)^m \tag{6-1}$$

Where C and m are material constants. To account for mean stress effect, Elber [160] was amongst the first researchers to propose the concept of crack closure to account for load ratio effect and used the effective stress intensity factor range ΔK_{eff} as the driving force for FCG：

$$\Delta K_{eff} = K_{max} - K_{op} \tag{6-2}$$

Where K_{max} and K_{op} correspond to the stress intensity factor calculated for the maximum load and the crack opening load, respectively. Then Kujawski [161][162] found that the effect of crack closure were greatly overestimated and a partial crack closure model should be used to address the stress ratio effect. In the partial crack closure model. The effective stress intensity range was modified to:

$$\Delta K_{eff} = K_{max} - K_{op}\left[1 + \left(\frac{2}{\pi} - 1\right) g\right] \tag{6-3}$$

$$g = exp\,[1 - \frac{K_{max}}{K_{max,th}}] \tag{6-4}$$

Where $K_{max,th}$ is the maximum stress intensity factor at threshold for a given R-ratio. However, many evidences suggested that this is not an easily applicable method and it required some experimental calibrations [162-165]. For example, the crack opening stress highly depends on the measurement location relative to crack tip and technique employed. Despite the fact that these crack-closure-based models can explain phenomenon such as crack growth delays and arrests after overloads, the load ratio effect, or the variable amplitude effect, there are still challenges in their applications [166-169]. On the other hand, other researchers have argued that the crack closure has limited effect on the fatigue crack propagation process since the closure takes place behind the crack tip [170-171]. Walker [172] proposed an effective stress involving the applied stress amplitude, $\Delta\sigma$, and the maximum applied stress, σ_{max}, to predict the load ratio effect on fatigue crack propagation and fatigue life.

$$\bar{\sigma} = \Delta\sigma^p \sigma_{max}^{1-p} \tag{6-5}$$

The above equation can be modified to the following form of effective stress intensity factor $\overline{K}$:

$$\overline{K} = \Delta K^{p} K_{max}^{1-p} \qquad 6\text{-}6$$

Where 0≤p≤1 is considered as a material parameter and it may depend on material and environment. Daniel Kujawski [166] proposed a similar equation to equation (6-6) but only considering the tensile part in one load cycle.

$$\frac{da}{dN} = C((\Delta K^{+})^{1-p} K_{max}^{p})^{m} \qquad 6\text{-}7$$

The significance of K_{max} on fatigue crack propagation was introduced by Sadananda [173] using a dislocation model. Furthermore, a unified approach was proposed by considering both ΔK and K_{max} as the driving forces along with their corresponding thresholds ΔK_{th} and $K_{max,th}$ which must be exceeded simultaneously for FCG to occur [174-177]. It was reported that this unified approach was able to correlate fairly well the FCG under threshold condition and at the low and intermediate stress intensities for stress ratios ranging from -1.0 to 1.0 [166, 174-177].

The two-parameter driving force approach has been further extended to describe the environment assisted FCG [177]. The basis for this extension is best described by the diagram shown in Figure 6-1. The diagram shows how the changes in each of the two parameters influences the FCG rate. As depicted by the figure, every L-shaped curve represents one FCG rate in terms of ΔK and K_{max} on both pure fatigue and corrosion fatigue condition. There are limiting threshold values for each of the parameters: ΔK* and K_{max}^{*}, for each crack growth rate. Lower limiting values are generally needed to reach the same crack growth rate for corrosion fatigue in comparison with the pure fatigue, which shows the detrimental effect of environment on FCG behavior. The figure also shows that the parameter ΔK predominantly contributes to the pure cyclic damage that is associated with dislocation reversibility [179]. The reduction in ΔK* is therefore attributed to the degree of restricted slip reversibility controlled by the influence of environment reactions on the emergent slip steps [180]. Correspondingly, K_{max} is the governing parameter in the static damage due to environment. The reduction in K_{max}^{*} is because the maximum applied force required to break atomic bonds is lowered due to environment interactions [181]. Therefore, while the electrochemical driving force contributed from environment cannot be directly quantified, the effect of environment on FCG can be expressed through K_{max}. A Unigrow model proposed by Glinka et al. [182][183] supports this idea. This model is based on a physical analysis of the elastic-plastic stress-strain history at the crack tip and thus gives a basic understanding of fatigue crack initiation and growth. More importantly, the obtained FCG expression was rather analogous to the previous two parameter driving force approach and could be also expanded to deal with CFCP. However, this model cannot account for the obvious frequency/time involved in CFCG.

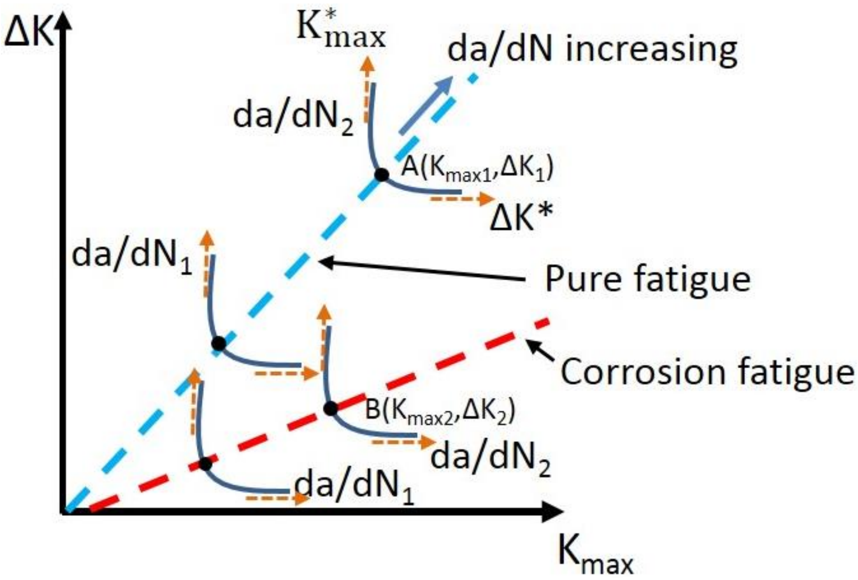

Figure 6-1 The ΔK-Kmax plot for the pure fatigue and the corrosion effect on fatigue behavior [154]

In this chapter, we propose a CFCP model based on the process interaction between FCG and SCC and the two-parameter driving force while accounting for the load ratio and frequency effects. Groups of FCG rate in vacuum, SCC velocity in 3.5 wt % NaCl solution, and CFCG rate in 3.5 wt % NaCl solution collected from several metallic materials will then be used to verify the effectiveness of this model.

6.2 Proposed Model

6.2.1 Corrosion fatigue crack propagation mechanisms

It is generally accepted that micro-cracks are nucleated from soft slip bands induced by cyclic loading [184]. The crack then propagates as a consequence of alternate plastic blunting in the loading part of the fatigue cycle followed by re-sharpening of the crack tip in the unloading part, as suggested by Laird [185]. In the aggressive environment, however, chemical reactions at the crack tip further complicates the mechanism of FCG. Two mainstream mechanisms on which a number of CFCG models were established have been brought forward to account for the accelerated crack growth. These are stress-assisted anodic dissolution (SAD) and hydrogen embrittlement (HE). For example, Wang [186] proposed a fracture model to predict CFCP was based on SAD mechanism. This model assumes that crack growth increment in every load cycle comprises two parts: one caused by mechanical damage and the other one due to corrosion dissolution of a metal at the crack tip. While the effect of HE on crack growth was acknowledged, but it was not considered in model [187]. In a superposition-based model Kim and Manning [127] used HE together with mechanical force to establish their crack propagation model. In their model, it is assumed that Hydrogen atoms produced by chemical reactions diffuse into the bulk material and accumulate at inhomogeneity ahead of the crack tip zone. The crack is then advance at an arbitrary hydrogen penetration distance when the accumulated damage reaches a critical value. However, it appears that there is no firm agreement evidence on which mechanism played a more dominant role in CFCG in any material-environment combinations [32][187]. Nevertheless, it can be reasonably hypothesized that the corrosive environment accelerates FCG by both SAD and HE mechanisms while their contribution varies in different material-environment system.

Based on above discussion and and Laird's plastic blunting-re-sharpening process [185], we propose a new model for CFCG. The fundamentals of this model are layed out in Figure 6-2. Several characteristic points on the loading and unloading reversals in one load cycle of stress- time curve is considered in Figure 6-2 (i) are selected to elucidate the CFCG. For comparison purposes, crack advancement due to a pure SCC Figure 6-2 (ii) and a pure fatigue Figure 6-2 (iii) in one load cycle are presented as well.

At the starting point a when no or small loads are applied to the crack body, the crack tip radius is small. As stress increases to point b, a large number of slips are activated which result in the separation of the material and the blunting of the crack tip. During this stage, hydrogen atoms produced by chemical reactions diffuse into the material and pile up to replace metal atoms ahead of the crack tip. This can reduce the cohesive strength and the surface energy required to create new crack surfaces [29][188], thereby accelerating the blunting process by HE. Noting that the parameter m in equation (6-1) indicates the resistance of the material to fatigue crack, a parameter θ (Eq. 6-9) is proposed in the new model to represent the deleterious effect of corrosion on the material properties. SCC does not occur at this stage because the stress level does not exceed the critical value K_{ISCC} [189].

When stress increases from point b to point c, the crack continuously advances, and the crack tip radius becomes larger. At this time, SAD starts joining with fatigue to contribute to the CFCP. Moreover, SAD at the crack tip leads to higher stress concentration [190], i.e. higher actual stress intensity at the crack tip. This was experimentally supported by smaller crack tip blunting angle in the corrosive environment compared to those in the air and/or in vacuum [191]. The effect of SAD on FCG, in the proposed new model, is represented by the enhanced actual stress intensities which is modified by proposed parameter β (Eq. 6-9) in the proposed model.

After point c above which SCC velocity remains constant, the fatigue crack propagates faster, and the crack tip radius further increases until stress reaches point d. When it comes to the unloading part, the slip direction is reversed, making the newly created crack faces crushed into the plane of crack and regenerate a sharp crack again. Simultaneously, stress-assisted dissolution occurring at the tip of the blunted crack makes the crack tip much sharper, which accelerates the re-sharpening process as well. Therefore, although the crack does not propagate mechanically in the unloading part, SCC still helps advance the crack until the stress level is decreased to point f (similar to point b) below which SCC does not occur. As a result, the total crack increment per cycle will be consisted of two parts:

$$\Delta a_{tot} = \Delta a_{cf} + \Delta a_{SCCf} \qquad 6\text{-}8$$

Where Δa_{cf} is the crack advancement per cycle from fatigue assisted by corrosion, and Δa_{SCCf} is the crack increment per cycle from SCC assisted by cyclic load.

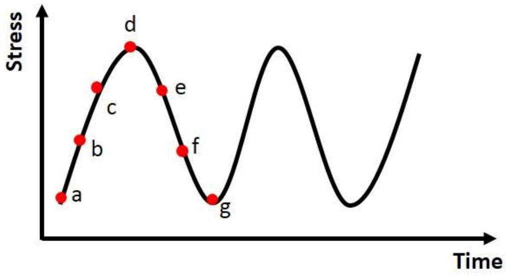

(i) Characteristic points on loading and unloading reversals of a typical load cycle

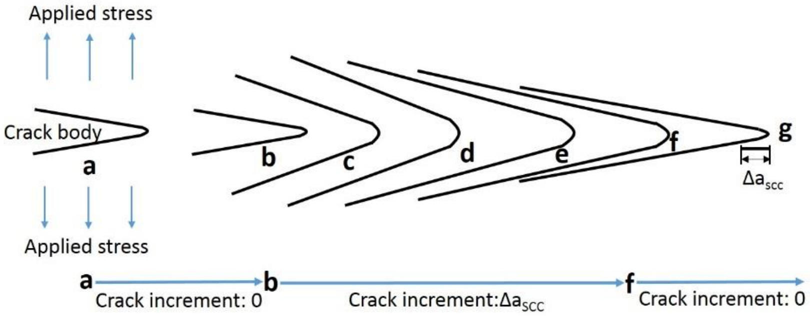

(ii) Crack advancement due to pure SCC occurring in one load cycle

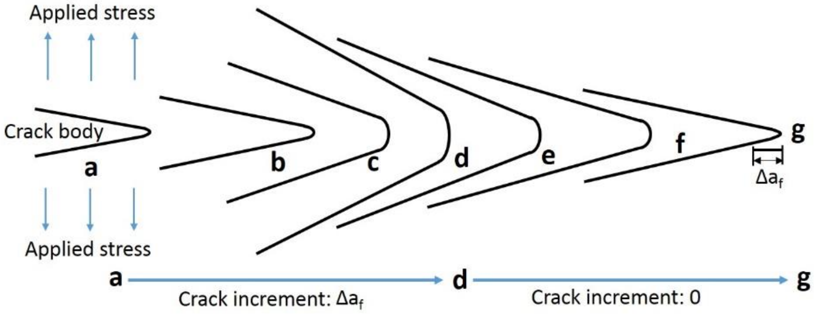

(iii) Crack advancement due to pure fatigue in one load cycle

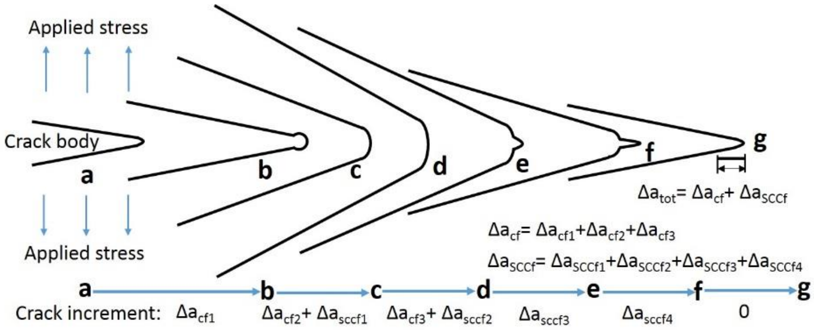

(iv) Crack advancement due to corrosion fatigue in one load cycle

Figure 6-2 CFCP mechanism

6.2.2 Description of the proposed model

The role of SCC in every load cycle on the whole CFCP has been explicitly characterized in the light of different crack growth stages as indicated in Figure 6-2. A two parameter driving force, ΔK and K_{max}, inspired by earlier models [166][182], is used to describe the CFCP. In other words, CFCP rate can be expressed as a function of ΔK and K_{max}, as oppose to the only driving force ΔK considered in Paris' equation for FCG [158]. The role of corrosion on CFCG is two-fold: direct contribution through SCC; and indirect contribution by accelerating FCG through material properties degradation. Therefore, a three-stage CFCG is proposed as follows and as depicted by Figure 6-3:

Stage I: before $\beta K_{max}<K_{ISCC}$ (Figure 6-3 (a) for $t<t_o$) below which SCC does not occur. In this stage fatigue is the only contributor to CFCG. However, due to the presence of corrosive environment, the FCG relation is modified by corrosion, as illustrated by region I in Figure 6-3(b), to the following relation:

$$(\frac{da}{dN})_{cf}= C_f(\beta \times {K_{max}}^{1-p} \times \Delta K^p)^{\theta m_f} \qquad 6\text{-}9$$

Where β and θ are parameters representing the effect of corrosion on the crack tip driving force and on the material property mf in FCG, respectively. C_f and mf are material constants in FCG, and p is in Walker's parameter accounting for stress ratio [172].

Stage II: when $K_{ISCC} \le \beta K_{max} < K_{pl}$ (Figure 6-3(a) for $t_o<t<t_1$), SCC starts joining FCG to contribute to the CFCG, as shown by the region II in Figure 6-3(b):

$$(\frac{da}{dN})_{cf}= Cf(\beta {K_{max}}^{1-p}\Delta K^p)^{\theta m_f}+2\int_{t0}^{1/f} Cscc(\beta K)^n dt \qquad 6\text{-}10$$

Where t_0 is set to the time when βK_{max} starts exceeding K_{ISCC} in one load cycle(Figure 6-3a). $Cscc$ and n are material constants associated with SCC.

Stage III: when $\beta K_{max} \ge K_{pl}$ (Figure 6-3(a) for $t>t_1$) above which SCC velocity is independent of stress intensity. The effect of corrosion on the driving force disappears while the influence of corrosion on degradation of material properties remains, as illustrated by the region III in Figure 6-3(b):

$$(\frac{da}{dN})_{cf}= Cf(\beta {K_{max}}^{1-p}\Delta K^p)^{\theta m_f}+2\int_{t0}^{t_1} Cscc(\beta K)^n dt + 2\int_{t_1}^{1/f} v_{pl} dt \qquad 6\text{-}11$$

Where t_1 is set to the time when βK_{max} starts exceeding K_{pl} in one load cycle (Figure 6-3(a)). v_{pl} is the constant SCC velocity in the plateau region III shown in Figure 6-3(b).

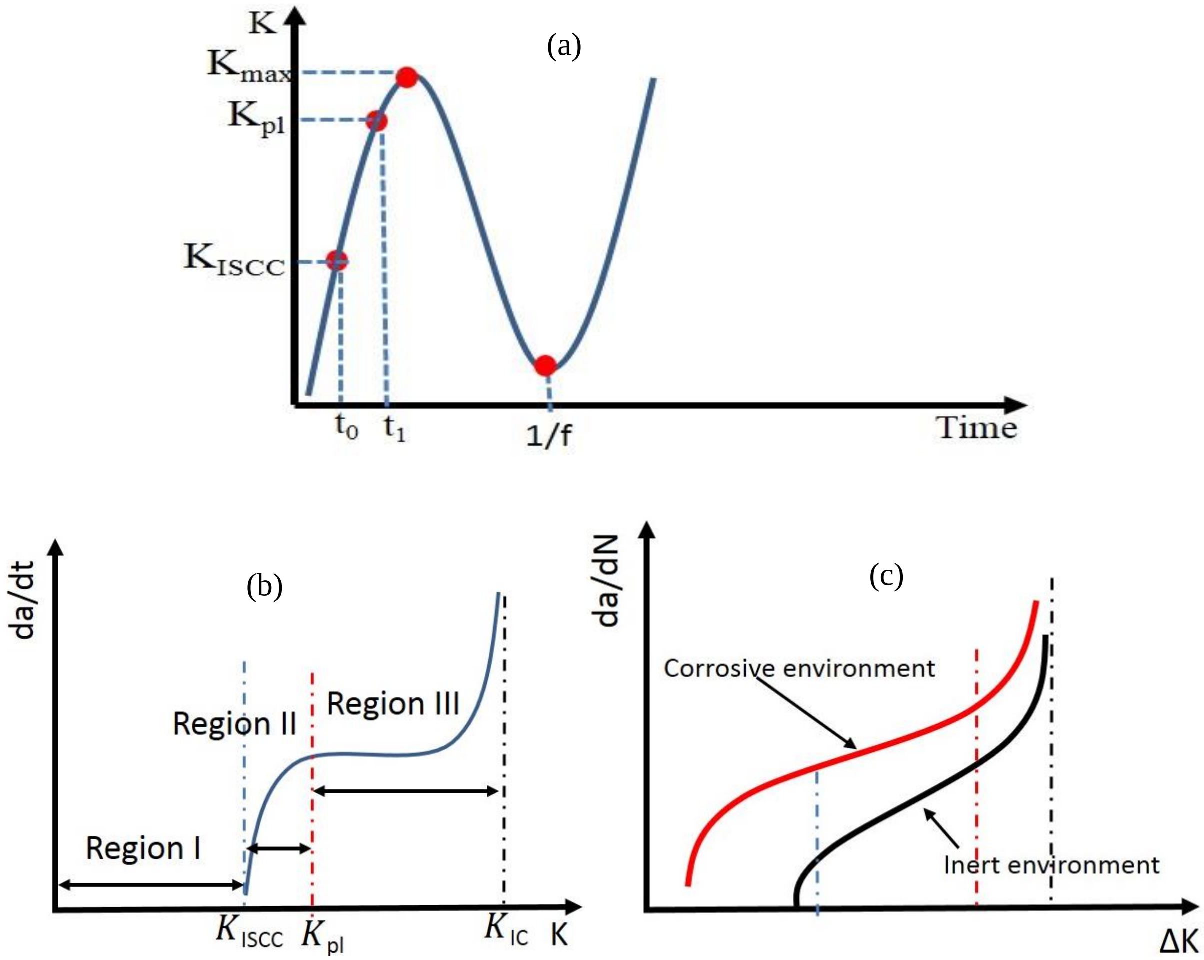

Figure 6-3 Description of CFCP model: (a) applied load history (stress intensity factor K); (b) the SCC velocity vs K curve; (c) the FCG rate in inert and corrosive environment vs ΔK curves.

6.2.3 Determination of correlation parameters in the proposed model

Apart from the usual constant employed in FCG: C_f, m_f, and p readily calculated through the curve fitting of FCG data in an inert environment [166]; and SCC parameters: C_{SCC} and n obtained by a similar experimental curve fitting using SCC data [169]; there are four other parameters introduced by proposed model: correlation parameters β and θ, and time constants t_0 and t_1. Determination of these four parameters β, θ, t_0 and t_1 alongside Walker's parameter p are discussed in the followings.

6.2.3.1 Determination of p

For one arbitrary FCG rate at different R-ratios in an inert environment such as vacuum, the effective driving force (${K_{max}}^{1-p}\Delta K^{p}$) should be the same [169]. As an example and for the case of AISI 4340 steel [192], FCG rates at two R-ratios of R_1=0.1 and R_2=0.9 against stress intensity range are shown in Figure 6-4. By drawing a random horizontal line that intersects these two curves, one gets two points that have the same crack growth rate but with different stress intensity ranges (Figure 6-4). Therefore,

$$K_{max1}^{1-p}\Delta K_1^{p} = K_{max2}^{1-p}\Delta K_2^{p} \qquad 6\text{-}12$$

Using the relation $\Delta \mathrm{K} = (1-\mathrm{R})\mathrm{K}_{\max}$, a typical value for p_i can be obtain from the following relation:

$$p_i = 1 - \frac{log\frac{\Delta K_1}{\Delta K_2}}{log\frac{1-R_1}{1-R_2}} \qquad 6\text{-}13$$

By repeating this process, a series of p values can be obtained and hence an average value can be finally determined as p= $\frac{\sum_{i=1}^{q} p_i}{q}$, q is the number of trials.

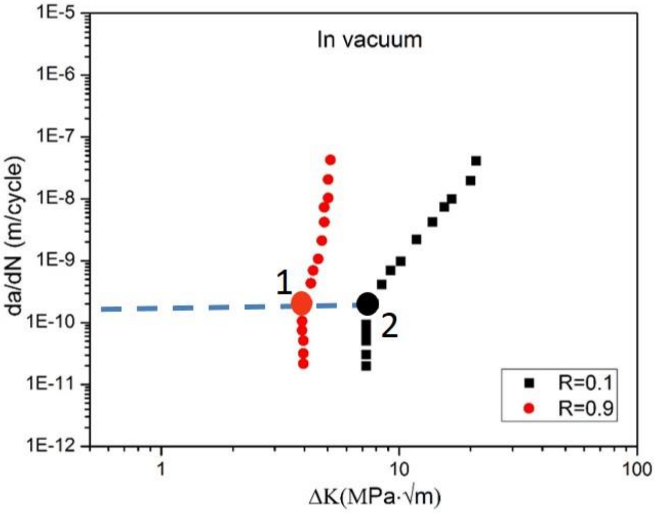

Figure 6-4 FCGR for AISI 4340 at R=0.1 and R=0.9 [188]. Example used to show determination of the parameter p.

6.2.3.2 Determination of time constants t_0, t_1

To illustrate the determination of time constant t_0 and t_1, let's consider an example of a load history K vs t given by a sinusoidal function that can be expressed as:

$$K = \frac{K_{max}+K_{min}}{2} + \frac{\Delta K}{2} sin\left(2\pi f t - \frac{\pi}{2}\right) \qquad 6\text{-}14$$

Where f is the cyclic frequency. Setting K to K_{ISCC} into the above equation and solving for t, t_0 can be obtained (Figure 6-*3*(a)):

$$t_0 = \left[\frac{\pi}{2} + arcsin\left(\frac{2K_{ISCC}}{\beta \Delta K} - \frac{1+R}{1-R}\right)\right] / (2\pi f) \qquad 6\text{-}15$$

Similarly, t_1 is determined by setting K in equation (6-14) to K_{pl}:

$$t_1 = \left[\frac{\pi}{2} + arcsin\left(\frac{2K_{pl}}{\beta \Delta K} - \frac{1+R}{1-R}\right)\right] / (2\pi f) \qquad 6\text{-}16$$

6.2.3.3 Determination of correlation parameters β, θ

Parameters β and θ are obtained in an iterative manner. One set of corrosion fatigue experimental results is required. First a value of 1.00 is set to β and θ (i.e., no corrosion effect) in equations (6-9) for region I (similar procedure is repeated for regions II and III) to come up with a predicted FCGR (da/dN) pre in region I. This value is the compare to the actual corrosion fatigue results to calculate the standard error:

$$\text{Standard error} = \frac{\sqrt{\sum \left(\frac{da}{dN_{pre}} - \frac{da}{dN_{actual}}\right)^2}}{\eta} \qquad 6\text{-}17$$

Where η is the number of data points selected for standard error calculation. Using a desirable increment (e.g., 0.01), the new values of β, θ are used in equation (6-9) to obtain a new standard error. Specifically, we first fix the value of θ to 1.00, and then substitute different set values of β, increasing from 1.00 to 2.00 with an increment step of 0.01 (i.e. plug (θ, β) values of (1.00, 1.00), (1.00, 1.01), (1.00, 1.02), …. (1.00, 2.00),) into equations (6-9) to (6-16). A series of predicted CFCG rates for each pair of (β, θ) are obtained and then used to calculate the 'standard error' using equation (6-17). Then this process is repeated with different θ values varying from 1.00 to 2.00 with an increment step of 0.01. This procedure is continued until the standard error become less than a designated convergence value (e.g., 10^{-3}).

In general, β and θ are both in the range of 1 to 2, therefore the values are obtained relatively quickly. The parameter β and θ in each region may be different and they mainly depend on the material-environment system.

6.3 Numerical examples for verification of the proposed model

FCG data in vacuum and corresponding SCC data for five different alloys are used to validate the proposed CFCG model. These examples include alloys most commonly used as structures. They include two types of 4340 steel with different yield strength, 300M steel, Titanium alloy Ti-6Al-4V and Aluminum alloy 7075-T651. In what follows, the same parameter β and θ are used for each stage of CFCP.

6.3.1 CFCG prediction in AISI 4340 steel ($\sigma_y = 1503MPa$)

The fatigue data in vacuum for AISI 4340 steel ($\sigma_y = 1503\text{MPa}$) was taken from [192] and the corrosion fatigue data and SCC data in 3.5% NaCl were taken from Ref [193]. Corrosion fatigue tests were conducted at a loading frequency 10Hz and at stress ratios 0.1 and 0.5. Figure 6-5 shows the test results and the corresponding predictive results using the proposed model as a function of the applied stress intensity range. At stress ratio R=0.1, as can be seen in Figure 6-5(a), the proposed model prediction shows fairly good agreement with experimental results, especially at high stress intensity ranges. Moreover, for R=0.5, the proposed model almost precisely predicts the actual CFCG rates. The parameter β and θ in the proposed model for this steel in 3.5%NaCl were found to be 1.15 and 1.17, respectively. All the values of other parameters are presented in Table 6-1.

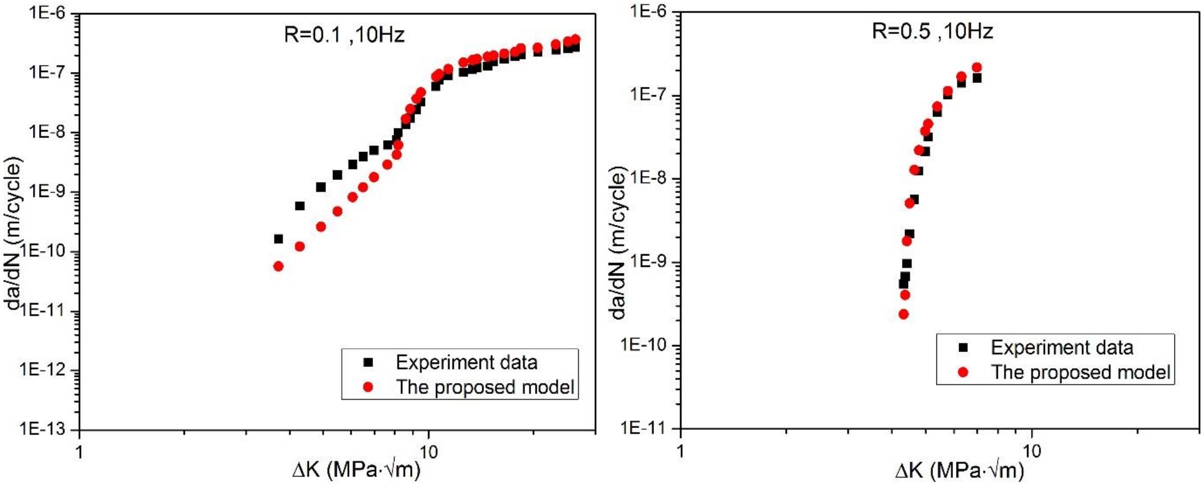

Figure 6-5Experimental CFCG rates of AISI 4340 steel ($\sigma_y = 1503MPa$) in 3.5% NaCl [193] and model prediction

Table 6-1 Values of the fitted experimental parameters in the corrosion fatigue model for each material

Material	C_f (m/cycle)/(MPa$\cdot\sqrt{m})^{m_f}$	m_f	p	C_{SCC} (m/s)/(MPa$\cdot\sqrt{m})^n$	n	β	θ
AISI 4340 steel ($\sigma_y = 1503MPa$)	$10^{-13.70}$	4.60	$p=0.027*\Delta K_{eff}+0.0765$	$10^{-30.33}$	17.45	1.15	1.17
AISI 4340 steel ($\sigma_y = 1669MPa$)	$10^{-13.70}$	4.60	$p=0.027*\Delta K_{eff}+0.0765$	$10^{-8.82}$	9.21	1.5	1.05
300M steel	$10^{-12.55}$	3.83	-	$10^{-48.92}$	32.36	1.2	1.07
Ti-6Al-4V	$10^{-11.74}$	3.65	0.294	10^{-20}	8.78	1.05	1.21
7075-T651	$10^{-13.74}$	6.17	-	$10^{-11.9}$	2.75	1.12	1.01

6.3.2 CFCG prediction in 4340 steel ($\sigma_y = 1669MPa$)

The fatigue data in vacuum and in 3.5% NaCl for 4340 steel ($\sigma_y = 1669$MPa) and SCC data in 3.5% NaCl were all collected from in Ref [192]. In this case, corrosion fatigue tests were performed with a frequency of 10 Hz at stress ratios 0.1 and 0.9 in 3.5% NaCl solution. Figure 6-6 shows the test CFCG rates and the corresponding predictive results using the proposed model as a function of the applied stress intensity range ΔK. Similarly, when R=0.1, the proposed model gives very good consistent results with the observed CFCG rate. In the case of R=0.9, good predictive results were also obtained by the proposed model except for slight discrepancies at the low ΔK, comparing with the actual CFCG rate. The values of the fitted parameters in the proposed model for the 4340 steel ($\sigma_y = 1669$MPa) in 3.5%NaCl are presented in Table 6-1.

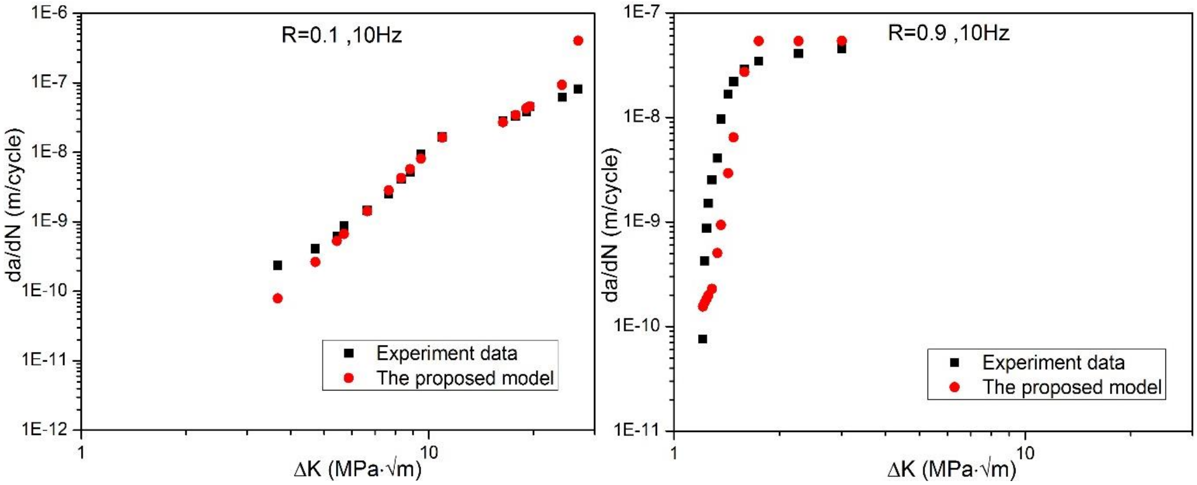

Figure 6-6 Experimental CFCG rates of AISI 4340 steel ($\sigma_y = 1669MPa$) in 3.5% NaCl [189] and model prediction

6.3.3 CFCG prediction in 300M steel

The fatigue data in vacuum and in 3.5% NaCl and SCC data in 3.5% NaCl for 300M steel used for validation of the proposed model were also collected from in Ref [192]. Similarly, corrosion fatigue tests were performed with a frequency of 10 Hz at stress ratios 0.1 and 0.9 in 3.5% NaCl environment. Figure 6-7 shows the test CFCG rates and the corresponding predictive results using the proposed model as a function of the applied stress intensity range ΔK. At both two stress ratios, the proposed model gives fairly good correlations to the experimental data except that the underestimation of CFCG rates at relatively low applied stress intensity ranges. This may be due to the use of the same parameter β and θ in three regions. The values of the fitted parameters in the proposed model for 300M steel in 3.5%NaCl are presented in Table 6-1.

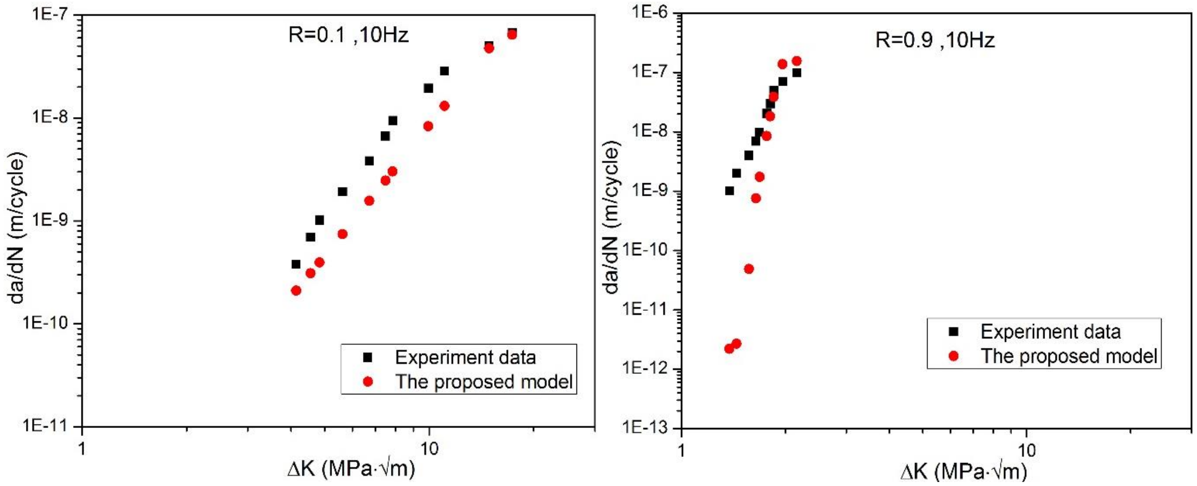

Figure 6-7 Experimental CFCG rates of 300M steel in 3.5% NaCl [192] and model prediction

6.3.4 CFCG prediction in Titanium alloy Ti-6Al-4V

The fatigue data in vacuum and in 3.5% NaCl and SCC data in 3.5% NaCl for Titanium alloy Ti-6Al-4V used for validation of the proposed model were obtained from in Ref [194]. Corrosion fatigue tests were performed with a stress ratio of 0.1 at frequencies 1Hz, 5Hz and 10Hz in 3.5% NaCl environment. Figure 6-8 shows the test CFCG rates and the corresponding predictive results using the proposed model as a function of the applied stress intensity range ΔK. When frequency f=1 Hz, the proposed model appears to be applicable at high stress intensity ranges. When f=5Hz and 10Hz, the proposed model shows fairly good agreement with the test data. Besides, the inappropriate use of the same β and θ in three regions can be clearly seen from the proposed model predictions in the case of f=5Hz and 10Hz. The values of the fitted parameters in the proposed model for Titanium alloy Ti-6Al-4V in 3.5%NaCl are presented in Table 6-1.

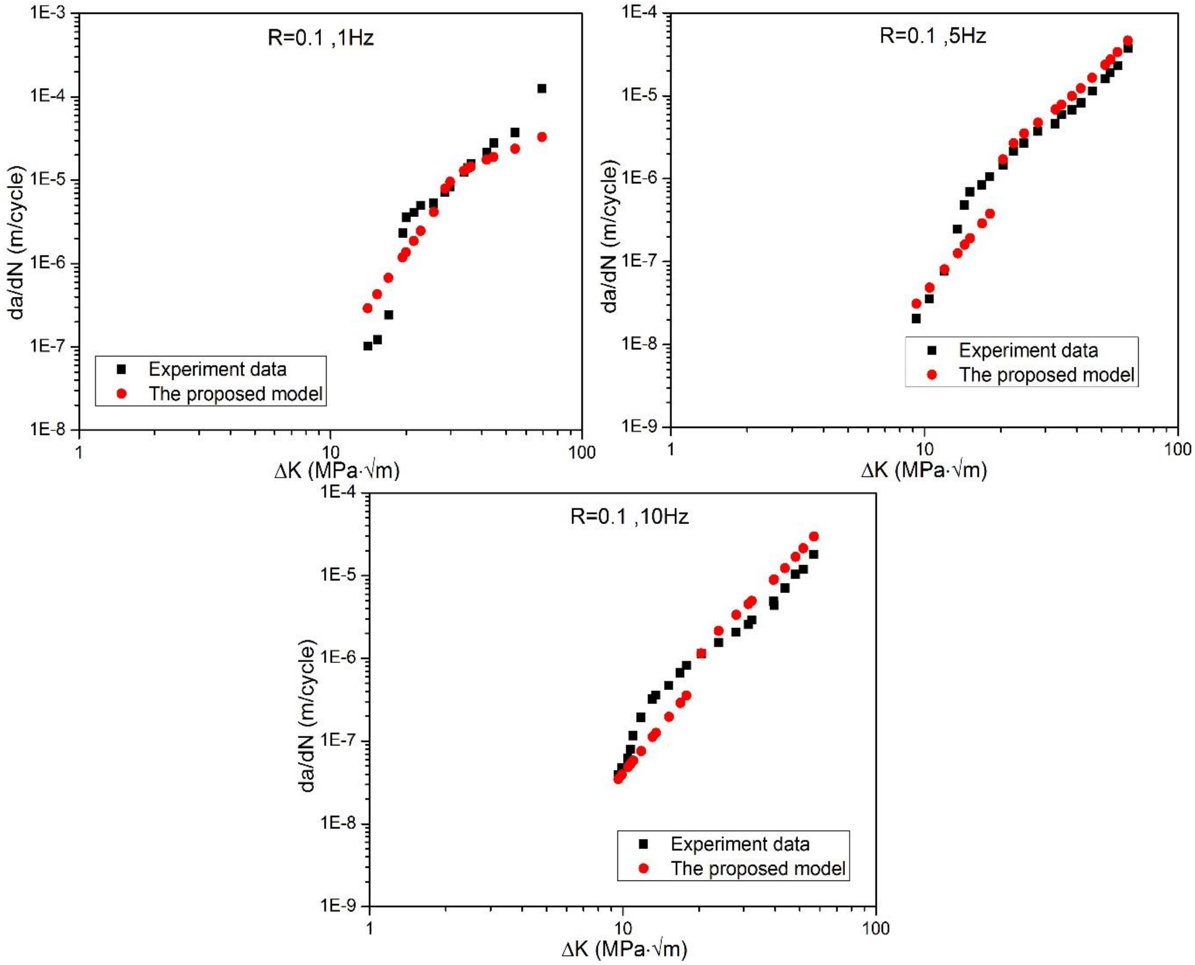

Figure 6-8 Experimental CFCG rates of Titanium alloy Ti-6Al-4V in 3.5% NaCl [194] and model prediction

6.3.5 CFCG prediction in Al alloy 7075-T651

The fatigue data in vacuum and in 3.5% NaCl and SCC data in 3.5% NaCl for Al alloy 7075-T651used for validation of the proposed model came from the Ref [195-196]. Corrosion fatigue tests were performed with a frequency of 10Hz at stress ratios 0.1 and 0.5 in 3.5% NaCl environment. Figure 6-9 shows the test CFCG rates and the corresponding predictive results using the proposed model as a function of the applied stress intensity range ΔK. In this alloy, the proposed model did not effectively provide the good predictions except for the high level of ΔK. The use of the same β and θ in three regions and low SCC velocities may be the reason for the underestimation. The values of the fitted parameters in the proposed model for Al alloy 7075-T651 in 3.5%NaCl are presented in Table 6-1.

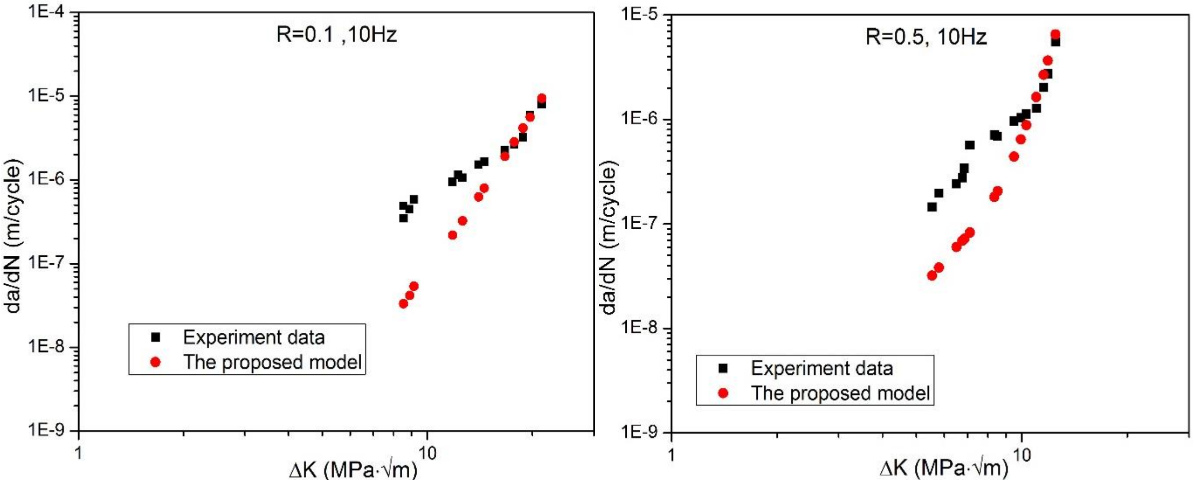

Figure 6-9 Experimental CFCG rates of Aluminum alloy 7075-T651 in 3.5% NaCl [195] and model prediction

6.4 Discussion

Two interacting processes including pure fatigue and SCC are assumed to happen simultaneously in the fatigue crack propagation of a metal in aqueous environments. In this model the interaction effect is considered by taking the FCG rate in an inert environment as a reference, the environmental contribution to the fatigue crack propagation rate is considered in terms of both changes in the crack tip driving force and the crack growth rate for a given applied stress, as expressed by equations (6-9) to (6-11). In this model, the two-parameter driving force approach was used to describe the environment-assisted FCG. It can be seen that the equation (6-9) is indeed expressed in terms of the driving forces ΔK and K_{max}. Since the characteristic time t_0 and t_1 in the second term of equation (6-10) and (6-11) are able to be represented by ΔK and K_{max}, the equation (6-10) and (6-11) can be converted into expressions (6-18) and (6-19) below in terms of ΔK and Kmax as well, which again supported the basic assumption of the two parameter driving force approach.

$$(\frac{da}{dN})_{cf} = C_f(\beta K_{max}^{1-p}\Delta K^{P})^{\theta m_f} + 2\int_{\left[\frac{\pi}{2}+\arcsin\left(\frac{2K_{ISCC}}{\beta\Delta K}-\frac{1+R}{1-R}\right)\right]/(2\pi f)}^{1/f} \frac{C_{SCC}}{\pi f\Delta K}\frac{(\beta K)^{n}}{\sqrt{1-(\frac{2K-K_{max}-K_{min}}{\Delta K})^{2}}}dK \qquad 6\text{-}18$$

$$(\frac{da}{dN})_{cf} = C_f(\beta K_{max}^{1-p}\Delta K^P)^{\theta m_f} + 2\int_{\left[\frac{\pi}{2}+\arcsin\left(\frac{2K_{ISCC}}{\beta\Delta K}-\frac{1+R}{1-R}\right)\right]/(2\pi f)}^{\left[\frac{\pi}{2}+arcsin\left(\frac{2K_{pl}}{\beta\Delta K}-\frac{1+R}{1-R}\right)\right]/(2\pi f)} \frac{C_{SCC}}{\pi f\Delta K}\frac{(\beta K)^n}{\sqrt{1-(\frac{2K-K_{max}-K_{min}}{\Delta K})^2}}dK + 2\int_{\left[\frac{\pi}{2}+arcsin\left(\frac{2K_{pl}}{\beta\Delta K}-\frac{1+R}{1-R}\right)\right]/(2\pi f)}^{1/f} \frac{v_{pl}}{\pi f\Delta K}\frac{1}{\sqrt{1-(\frac{2K-K_{max}-K_{min}}{\Delta K})^2}}dK \qquad 6\text{-}19$$

One of the most important capabilities of CFCG models is the ability to account for the characteristic phenomenon of environment-assisted FCG such as frequency and R-ratio effects [197][198]. The proposed new model is not only able to incorporate the influence of load ratio using the two-parameter approach, but it can also account for the frequency effect through the integration of crack velocity in every load cycle. Moreover, the effect of waveform on CFCG [199] can be considered as well in this model since SCC velocity varies with stress intensity factor and is integrated stage-by-stage, as can be seen in equation (6-10) and (6-11).

The correlation parameter β introduced into the model represents the effect of stress corrosion on the crack tip driving force for FCG. The crack tip driving force was enhanced by stress-assisted dissolution and thus increases the FCG rate, which generally makes the value of parameter β greater than 1.0, or empirically in the range of 1.0 to 2.0. It should be noted that all the discussion here are based on fatigue crack propagation in an inert environment. On the other hand, parameter θ is characterizing the degraded material property by the corrosive environment. The exponent m_f represents the ability of a metal to resist fatigue crack propagation, the lower its value, the higher its resistant ability. Therefore, the value of θ should be greater than 1.0 in the corrosive environment. The magnitude of both parameters β and θ actually depends on the susceptibility of the metallic material to the corrosive environment. For example, the effect of environment on FCG rate was reduced, as can be found from the nearly overlapped da/dN vs ΔK curves in the corrosive environment and in air at high stress intensities [192]. This means that the parameter β or θ may vary in different stages of CFCP. Also, as we can see from the verification results above, the predictions of the proposed model near thresholds are mostly below the test data. One of the reasons may lie in the use of same values of the parameter β and θ in the three different regions. Another reason is that we neglect the role of short crack propagation at the very early stage of the whole crack growth in the proposed model since this process is very short for Mg alloys but that’s probably not the case for other engineering metals.

The threshold stress intensity range ΔK_{th} for FCG and the threshold stress intensity K_{ISCC} for SCC are key parameters for material design. ΔK_{th} is normally defined as the critical value below which there is no fatigue crack advancement. In practical condition, however, it is mostly obtained when the FCG rate exceeds 10^{-10}m/cycle [199]. Many experiments have demonstrated that ΔK_{th} values are generally higher in vacuum than in the corrosive environment [192][193]. The formulation for the proposed model also follows this observation. At threshold point, we know that CFCG rate (10^{-10}m/cycle in this case) can be basically determined by below equation:

$$10^{-10} = \mathrm{C_f}(\beta \Delta K_{th,corro}^{p} \mathrm{K_{max}}^{1-\mathrm{p}})^{\theta m_f} \tag{6-20}$$

Assuming that the FCG rate at threshold point in an inert environment can be determined by Paris equation,

$$10^{-10} = \mathrm{C_f}(\Delta K_{th,inert})^{m_f} \tag{6-21}$$

Where $\Delta K_{th,corro}$ is the threshold stress intensity range in the corrosive environment and $\Delta K_{th,inert}$ is the threshold value in an inert environment. Combing equation (6-20) and equation (6-21) yields

$$(\beta \Delta K_{th-corro}^{p} \mathrm{K_{max}}^{1-\mathrm{p}})^{\theta m_f} = (\Delta K_{th-inert})^{m_f} \tag{6-22}$$

Noting that $K_{max} = \frac{\Delta K}{1-R}$, we have

$$\Delta K_{th-corro} = \frac{\Delta K_{th-inert}^{\frac{1}{\theta}}(1-R)^{1-p}}{\beta} \text{ or } \frac{\Delta K_{th-corro}}{\Delta K_{th-inert}} = \frac{\Delta K_{th-inert}^{\frac{1}{\theta}-1}(1-R)^{1-p}}{\beta} \tag{6-23}$$

Because the parameter $\beta>1$, $(1-R)^{1-p}<1$ and $\Delta K_{th-inert}^{\frac{1}{\theta}-1}<1$, we have

$$\Delta K_{th,corro} < \Delta K_{th,inert} \tag{6-24}$$

Therefore, we can conclude that based on the proposed model fatigue crack propagation occurs earlier in the corrosive environment than in an inert environment. The same analysis may be also applied to the $\mathrm{K_{ISCC}}$. Crack velocity and threshold stress $\mathrm{K_{ISCC}}$ in SCC are highly sensitive to the effective strain rate at the crack tip [201]. Limited attention has been paid to the effect of cyclic loading on the $\mathrm{K_{ISCC}}$. However, in the proposed model this effect is accounted for and it is apparent that a lower threshold stress ${K_{ISCC}}/{\beta}$, termed as the effective threshold $\mathrm{K_{eff\text{-}ISCC}}$, is needed to initiate SCC.

6.4.1 Comparison with classical CFCG models

Figure 6-10 gives a comparison of the proposed model (for the case of 4340 steel example above with results shown in Figure 6-5) with two other classical models, superposition and competition models, with experiment results from Ref [193]. The experimental data was obtained from a fatigue test for 4340 steel in 3.5% NaCl solution at an R-ratio of 0.1 and a frequency of 10 Hz. It is clearly seen that the superposition model, the competition model, and the proposed model can all correlate well with the experimental results at high stress intensities, specifically after ΔK exceed the threshold value (around 10 MPa·√m) for the occurrence of SCC. This is because CFCG rates predicted in this range in all three models were contributed by the dominant SCC rate. The small difference in these predictions at high stress intensities is due to the different considerations of SCC. For example, the competition model uses $(\frac{da}{dN})_{cf}$=(da/dN)$_{SCC}$ at this stage while in the proposed model $(\frac{da}{dN})_{cf}$ is expressed in terms of $\beta^n(\frac{\mathrm{da}}{\mathrm{dN}})_{SCC}$ in equation (6-10). At low stress intensities, the competition model and the superposition model give the same predictive results, which show good correlations with experimental data for the earlier part. However, these two classical models both overestimated the threshold stress intensity range ΔK_{th} for fatigue crack propagation. In contrast, the proposed model gives a very good prediction in the ΔK_{th} and the trend of $(\frac{da}{dN})_{cf}$ vs ΔK curve but slightly underestimates the CFCG rates at this stage. Before K_{ISCC} where SCC does not occur, the superposition model and the competition model use the FCG rate in air to represent the CFCG rate here. As a result, the ΔK_{th} is overestimated. The corrosive environment seems to show no big influence on the FCG rate in comparison with the FCG rate in air as shown in Ref [128], thus these two classical CFCG models give good predictions in the linear regions. However, in the proposed model, CFCG rates at low stress intensities are determined from the reference data of FCG rate in an inert environment. This indeed will lead to some underestimations if the effect of corrosion on FCG rates is not considered. On the other hand, the phenomenon of short crack behavior [202] at the very beginning of crack propagation can also increase the inaccuracies and complexities of modeling on CFCP. The proposed model is based on the linear elastic fracture mechanism (LEFM) theory, which does not apply to short crack behavior as the size of the crack is comparable to the plastic zone.

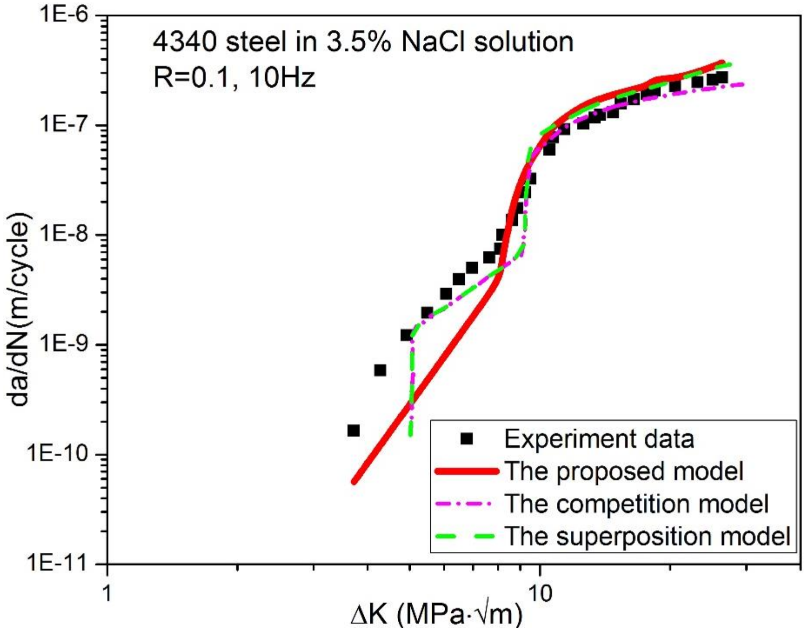

Figure 6-10 Experimental results and CFCG rates predicted by the proposed model and three other models

Chapter 7 Conclusions, Contributions, and Future work

7.1 Conclusions

This thesis investigated the surface coating for corrosion protection of Mg alloys and proposed a corrosion fatigue crack propagation model to predict the corrosion fatigue crack growth rate. Through this research, the following conclusions were drawn at the end of each chapter and are reiterated below:

- The effects of conversion process parameters on the coating microstructure and corrosion performance were examined: i) The coating grew thicker and more corrosion resistant with the increasing immersion time, but when the treatment time was too long, the corrosion resistance of the coated samples would decrease due to the appearance of large cracks in the coating; ii) a thick Mn-P coating can be formed on the surface of Mg alloy AZ31B in a very short duration if treated in a low-pH bath (below 2.0) while it requires much more time to produce a relatively thick coating layer if treated in a high-pH bath (above 3.0). The coating obtained in a low-pH bath tends to has wide cracks and low compactness while the coating built in a high-pH bath tends to be dense and has no significant cracks; iii) Increasing the bath temperature is able to enhance the coating thickness, but serious cracks were also gradually induced in the coating with the rising temperature.
- A two-stage conversion process was developed based on the examination of the effects of conversion process parameters. The two-stage conversion process includes a treatment in a low pH solution and then an immediate treatment in a high pH solution; A thick and dense protective surface coating was found to be deposited on the surface of Mg alloy AZ31B. Experimental results showed that the two-stage conversion coating exhibited better corrosion performances than either of the single conversion coatings.
- E-coat and powder coating were used as a topcoat for various coated Mg alloys. The Mn-P conversion coating improved not only the corrosion resistance of Mg alloys, but the adhesion between the substrate and E-coating; Powder coating shows better corrosion performance than E-coating; MAO coated ZK60 with powder coating showed the best corrosion performance among all the investigated coat system; The CCC coated ZK60 shows better performance in the scribe test due to the self-healing ability of CCC; The ability of coated Mg alloys to resist against general corrosion largely depends on the corrosion susceptibility of the substrate, surface coating strategies, and the adhesive bonding between them.
- A new process interaction model along with a CFCP mechanism are presented to account for fatigue crack propagation of a metal in the corrosive environment. This model assumes that that CFCG is an interactive process between pure fatigue and SCC. The FCG rates in an inert

environment are taken as a baseline and are combined with SCC to explain the CFCP rate; The role of SCC in every stages of a load cycle on the whole CFCP was explicitly accounted for accordingly using the SCC velocity curve. A two-parameter driving force (i.e. ΔK for FCG and K_{max} for SCC) inspired by previous models was employed to describe the CFCP.

- Five types of materials including two 4340 steels with different yield strength, 300M steel, 7075-T651, and titanium alloy Ti-6Al-4V have been used to verify the new model. Considering the scatter nature of corrosion fatigue data, it is found that good agreements can be obtained between the experiment data and the predictive results. However, due to the complexity of corrosion fatigue, more research is still needed to further improve the predictions.

7.2 Contributions

- A new process interaction model is proposed for the prediction of corrosion fatigue crack propagation rate in metals. The significance of stress corrosion cracking in contributing the fatigue crack propagation is explicitly considered stage-by-stage in the crack velocity curve of SCC.
- The effects of processing parameters on the corrosion behavior of AZ31 is systematically studied by using an orthogonal experimental plan. It is found that bath pH value, immersion time, and bath temperature become the three important factors in controlling the quality of the Mn-P conversion coating, especially the former two parameters. A two-stage conversion process is developed to produce a thick, dense and compact coating on AZ31.
- A two-layer corrosion protection strategy for forged AZ80, and ZK60 Mg alloys of a lower control arm were successfully evaluated and shown to significantly improve corrosion properties.
- Two journal papers have been published, and one is ready to be submitted.

7.3 Recommended and Future Work

Considering the long-term objective of predicting the corrosion fatigue life for the coated Mg alloys, the following work is recommended for next steps:

- The effect of surface coating on the corrosion fatigue crack initiation should be investigated. To complete the prediction of the whole corrosion fatigue life, the corrosion pit growth behavior, including the evolution of the corrosion pit size and shape at certain fatigue cycle, which has been reviewed in chapter 1 to model the corrosion fatigue crack initiation, need to be characterized on the coated Mg alloys; The effect of stress level (different $\Delta\sigma$, R-ration and σ_{max}) on the corrosion pit growth needs to be studied. Specifically, a designed corrosion salt spray test under cyclic loading would be recommended to collect such data.

- Stress corrosion cracking test for the uncoated Mg alloy should be conducted. The measurements of the threshold stress intensity factor (K_{ISSC}) and the crack velocity as a function of stress intensity factor (da/dt vs K) for the investigated Mg alloy need to be done to predict the corrosion fatigue crack propagation rate by combining with the fatigue data in an inert environment.
- Fatigue crack propagation test in air at a high frequency needs to be conducted to provide/simulate the fatigue data in an inert environment; In this test, at least two R-ratios should be used to determine the material constant C_f and m_f. In order to determine the correlating parameters β and θ and validate the corrosion fatigue crack propagation model, corrosion fatigue crack propagation tests for the Mg alloy at least two different R-ratios and two different frequencies need to be performed.

Reference

[1]. http://metalpedia.asianmetal.com/metal/magnesium/application.shtml

[2]. Kainer, Karl U. *Magnesium alloys and technology*. John Wiley & Sons, 2003.

[3]. Watarai, Hisao. "Trend of research and development for magnesium alloys." *Science&Technology* 7.18 (2006): 84-97.

[4]. Schumann, S. "The paths and strategies for increased magnesium applications in vehicles." *Materials Science Forum*. Vol. 488. Trans Tech Publications, 2005.

[5]. Kulekci, Mustafa Kemal. "Magnesium and its alloys applications in automotive industry." *The International Journal of Advanced Manufacturing Technology* 39.9-10 (2008): 851-865.

[6]. Blawert, C., N. Hort, and K. U. Kainer. "Automotive applications of magnesium and its alloys." *Trans. Indian Inst. Met* 57.4 (2004): 397-408.

[7]. He, X. L., et al. "Investigation on corrosion fatigue property of epoxy coated AZ31 magnesium alloy in sodium sulfate solution." *Theoretical and Applied Fracture Mechanics* 70 (2014): 39-48.

[8]. Materials Data Book. Cambridge University Engineering Department, 2003 Edtion.

[9]. Uematsu, Yoshihiko, et al. "Improvement of corrosion fatigue strength of magnesium alloy by multilayer diamond-like carbon coatings." *Surface and Coatings Technology* 205.8 (2011): 2778-2784.

[10]. Ishihara, S., et al. "Effect of electroless-Ni-plating on corrosion fatigue behavior of magnesium alloy." *Surface and Coatings Technology* 202.10 (2008): 2085-2092.

[11]. Bhuiyan, Md Shahnewaz, and Yoshiharu Mutoh. "Corrosion fatigue behavior of conversion coated and painted AZ61 magnesium alloy." *International Journal of Fatigue* 33.12 (2011): 1548-1556.

[12]. Ishihara, S., et al. "The corrosion fatigue resistance of an electrolytically-plated magnesium alloy." *International Journal of Fatigue* 32.8 (2010): 1299-1305.

[13]. Notoya, Hisakimi, Tomonori Namito, and Sotomi Ishihara. "Improvement in Corrosion Fatigue Resistance of Mg Alloy Due to Plating." *Magnesium Alloys-Corrosion and Surface Treatments*. InTech, 2011. Joost, William J., and Paul E. Krajewski. "Towards magnesium alloys for high-volume automotive applications." *Scripta Materialia* 128 (2017): 107-112.

[14]. Cao, Fuyong, et al. "Stress corrosion cracking of several solution heat-treated Mg–X alloys." *Corrosion Science* 96 (2015): 121-132.

[15]. Song, Guan Ling, and Andrej Atrens. "Corrosion mechanisms of magnesium alloys." *Advanced engineering materials* 1.1 (1999): 11-33.

[16]. Ghali, Edward. "Corrosion and protection of magnesium alloys." *Materials Science Forum*. Vol. 350. Trans Tech Publications, 2000.

[17]. Song, Guangling, and Andrej Atrens. "Understanding magnesium corrosion—a framework for improved alloy performance." *Advanced engineering materials* 5.12 (2003): 837-858.

[18]. Skar, J. I. "Corrosion and corrosion prevention of magnesium alloys." *Materials and Corrosion* 50.1 (1999): 2-6.

[19]. Zeng, Rong-chang, et al. "Review of studies on corrosion of magnesium alloys." *Transactions of Nonferrous Metals Society of China* 16 (2006): s763-s771.

[20]. Ghali, Edward, Wolfgang Dietzel, and Karl-Ulrich Kainer. "General and localized corrosion of magnesium alloys: a critical review." *Journal of Materials Engineering and Performance* 13.1 (2004): 7-23.

[21]. Greene, Norbert D., and Mars G. Fontana. "A Critical Analysis of Pitting Corrosion★." *Corrosion* 15.1 (1959): 41-47.

[22]. Tunold, Reidar, et al. "The corrosion of magnesium in aqueous solution containing chloride ions." *Corrosion Science* 17.4 (1977): 353-365.

[23]. Szklarska-Smialowska, Z. "Review of literature on pitting corrosion published since 1960." *Corrosion* 27.6 (1971): 223-233.

[24]. Roberge, Pierre R. *Handbook of corrosion engineering*. McGraw-Hill, 2000.

[25]. Winzer, Nicholas, et al. "A critical review of the stress corrosion cracking (SCC) of magnesium alloys." *Advanced Engineering Materials* 7.8 (2005): 659-693.

[26]. Stampella, R. S., R. P. M. Procter, and V. Ashworth. "Environmentally-induced cracking of magnesium." *Corrosion Science* 24.4 (1984): 325-341.

[27]. Fairman, Lawrence, and J. M. West. "Stress corrosion cracking of a magnesium aluminium alloy." *Corrosion Science* 5.10 (1965): 711IN7713-712IN9716.

[28]. Sieradzki, K., and R. C. Newman. "Stress-corrosion cracking." *Journal of physics and chemistry of solids* 48.11 (1987): 1101-1113.

[29]. Song, R. G., et al. "A study on stress corrosion cracking and hydrogen embrittlement of AZ31 magnesium alloy." *Materials Science and Engineering: A* 399.1 (2005): 308-317.

[30]. Atrens, Andrej, et al. "Stress corrosion cracking and hydrogen diffusion in magnesium." *Advanced Engineering Materials* 8.8 (2006): 749-751.

[31]. Atrens, Andrej, Nicholas Winzer, and Wolfgang Dietzel. "Stress corrosion cracking of magnesium alloys." *Advanced Engineering Materials* 13.1-2 (2011): 11-18.

[32]. Shipilov, S. A. "Corrosion fatigue." *Advances in Fatigue, Fracture and Damage Assessment of Materials, A. Varvani-Farahani, ed., WIT Press, Billerica, MA* (2005): 329-389.

[33]. Shaha, S. K., S. B. Dayani, and H. Jahed. "Influence of cold spray on the enhancement of corrosion fatigue of the AZ31B cast Mg alloy." *TMS Annual Meeting & Exhibition*. Springer, Cham, 2018.

[34]. Eliezer, A., et al. "Static and dynamic corrosion fatigue of Mg alloys used in automotive industry." *Materials and manufacturing processes* 20.1 (2005): 75-88.

[35]. Unigovski, Ya, et al. "Corrosion fatigue of extruded magnesium alloys." *Materials Science and Engineering: A* 360.1 (2003): 132-139.

[36]. Nan, Z. Y., S. Ishihara, and T. Goshima. "Corrosion fatigue behavior of extruded magnesium alloy AZ31 in sodium chloride solution." *International Journal of Fatigue* 30.7 (2008): 1181-1188.

[37]. Bhuiyan, Md Shahnewaz, et al. "Corrosion fatigue behavior of extruded magnesium alloy AZ61 under three different corrosive environments." *International Journal of Fatigue* 30.10 (2008): 1756-1765.

[38]. Stephens, R. I., C. D. Schrader, and K. B. Lease. "Corrosion fatigue of AZ91E-T6 cast magnesium alloy in a 3.5 percent NaCl aqueous environment." *Journal of engineering materials and technology* 117.3 (1995).

[39]. Chakrapani, D. G., and E. N. Pugh. "Hydrogen embrittlement in a Mg-Al alloy." *Metallurgical Transactions A* 7.2 (1976): 173-178.

[40]. Dubey, Dhananjay, et al. "Comparative study on the stress corrosion cracking susceptibility of AZ80 and AZ31 magnesium alloys." Materials Science and Engineering: A (2020): 139793.

[41]. Tokaji, Keiro, Masaki Nakajima, and Yoshihiko Uematsu. "Fatigue crack propagation and fracture mechanisms of wrought magnesium alloys in different environments." *International Journal of Fatigue* 31.7 (2009): 1137-1143

[42]. Wittke, P., M. Klein, and F. Walther. "Corrosion fatigue behaviour of creep-resistant magnesium alloy Mg-4Al-2Ba-2Ca." *Procedia Engineering* 74 (2014): 78-83.

[43]. Wang, Jie, Xin Pang, and Hamid Jahed. "Surface protection of Mg alloys in automotive applications: A review." (2019).

[44]. Gadow, R., Gammel, F. J., Lehnert, F., Scherer, D., & Skar, J. I. (2000). Coating system for magnesium diecastings in class A surface quality. Magnesium Alloys and Their Applications, 492-498.

[45]. Höche, D., Nowak, A., & John-Schillings, T. (2013). Surface cleaning and pre-conditioning surface treatments to improve the corrosion resistance of magnesium (Mg) alloys. In Corrosion Prevention of Magnesium Alloys (pp. 87-109).

[46]. Wu, C. Y., & Zhang, J. (2011). State-of-art on corrosion and protection of magnesium alloys based on patent literatures. Transactions of Nonferrous Metals Society of China, 21(4), 892-902.

[47]. Chen, X. B., N. Birbilis, and T. B. Abbott. "Review of corrosion-resistant conversion coatings for magnesium and its alloys." *Corrosion* 67.3 (2011): 035005-1.

[48]. Abela, S. (2011). Protective coatings for magnesium alloys. In Magnesium Alloys-Corrosion and Surface Treatments. InTech.

[49]. Pommiers, S., Frayret, J., Castetbon, A., & Potin-Gautier, M. (2014). Alternative conversion coatings to chromate for the protection of magnesium alloys. Corrosion Science, 84, 135-146.

[50]. Van Phuong, N., Lee, K., Chang, D., Kim, M., Lee, S., & Moon, S. (2013). Zinc phosphate conversion coatings on magnesium alloys: a review. Metals and Materials International, 19(2), 273-281.

[51]. Jian, S. Y., Chu, Y. R., & Lin, C. S. (2015). Permanganate conversion coating on AZ31 magnesium alloys with enhanced corrosion resistance. Corrosion Science, 93, 301-309.

[52]. Zeng, R. C., Zhang, F., Lan, Z. D., Cui, H. Z., & Han, E. H. (2014). Corrosion resistance of calcium-modified zinc phosphate conversion coatings on magnesium–aluminum alloys. Corrosion Science, 88, 452-459.

[53]. Lin, C. S., Lin, H. C., Lin, K. M., & Lai, W. C. (2006). Formation and properties of stannate conversion coatings on AZ61 magnesium alloys. Corrosion Science, 48(1), 93-109.

[54]. Greene, J. A., & Vonk, D. R. (2004). U.S. Patent No. 6,749,694. Washington, DC: U.S. Patent and Trademark Office.

[55]. Morris, W. C. (1942). U.S. Patent No. 2,294,760. Washington, DC: U.S. Patent and Trademark Office.

[56]. Guerci, G., Mus, C., & Stewart, K. (2000). Surface treatments for large automotive magnesium components. Magnesium Alloys and their Applications, 484-491.

[57]. Rudd, A. L., Breslin, C. B., & Mansfeld, F. (2000). The corrosion protection afforded by rare earth conversion coatings applied to magnesium. Corrosion Science, 42(2), 275-288.

[58]. Takenaka, T., Ono, T., Narazaki, Y., Naka, Y., & Kawakami, M. (2007). Improvement of corrosion resistance of magnesium metal by rare earth elements. Electrochimica Acta, 53(1), 117-121.

[59]. Doerre, Mark, et al. "Advances in Automotive Conversion Coatings during Pretreatment of the Body Structure: A Review." Coatings 8.11 (2018): 405.

[60]. Milošev, I., and G. S. Frankel. "Conversion Coatings Based on Zirconium and/or Titanium." Journal of The Electrochemical Society 165.3 (2018): C127-C144.

[61]. Giles, Terrence R., et al. "An update of new conversion coating for the automotive industry." SAE International Journal of Materials and Manufacturing 1.1 (2009): 575-581.

[62]. Brady, Michael P., et al. "Advanced characterization study of commercial conversion and electrocoating structures on magnesium alloys AZ31B and ZE10A." Surface and Coatings Technology 294 (2016): 164-176.

[63]. Li, N., Chen, X., Hubbert, T., & Berkmortel, R. (2005). 2005 Ford GT Magnesium Instrument Panel Cross Car Beam (No. 2005-01-0341). SAE Technical Paper.

[64]. Cole, G. S. (2013). Magnesium (Mg) corrosion protection techniques in the automotive industry. In Corrosion Prevention of Magnesium Alloys (pp. 489-508).

[65]. Blawert, C., Hort, N., & Kainer, K. U. (2004). Automotive applications of magnesium and its alloys. Trans. Indian Inst. Met, 57(4), 397-408.

[66]. Environmentally Friendly Conversion Coating on Mg Alloy [Internet]. [Place unknown: Institute of Metal Research Chinese Academy of Sciences]; c2018 [cited 2018 Sep]. Available from: http://english.imr.cas.cn/research/researchprogress/201408/t2014080-5_125571.html.

[67]. Gray, J. E., and Ben Luan. "Protective coatings on magnesium and its alloys—a critical review." *Journal of alloys and compounds* 336.1 (2002): 88-113.

[68]. Chiu, K. Y., Wong, M. H., Cheng, F. T., & Man, H. C. (2007). Characterization and corrosion studies of fluoride conversion coating on degradable Mg implants. Surface and Coatings Technology, 202(3), 590-598.

[69]. Chen, X. B., Yang, H. Y., Abbott, T. B., Easton, M. A., & Birbilis, N. (2014). Corrosion protection of magnesium and its alloys by metal phosphate conversion coatings. Surface Engineering, 30(12), 871-879.

[70]. Dolan, S. E. (1995). U.S. Patent No. 5,449,415. Washington, DC: U.S. Patent and Trademark Office.

[71]. Walter, M., & Kurze, P. (2004). MAGPASS-COAT® as a Chrome-free Pre-treatment for Paint Layers and an Adhesive Primer for Subsequent Bonding (No. 2004-01-0134). SAE Technical Paper.

[72]. Kainer, K. U. (Ed.). (2007). Magnesium: proceedings of the 7th International Conference on Magnesium Alloys and their Applications. John Wiley & Sons.

[73]. Chemetall. Oxsilan® [Internet]. [Place unknown: Chemetall GmbH]; c2018 [cited 2018 Sep]. Available from: http://www.chemetall.com/Products/Trademarks/Oxsilan/index.jsp.

[74]. CHEMEON TCP-HF [Internet]. [Place unknown: NALTIC Industrials, LLC]; [cited 2018 Sep]. Available from: http://naltic.com/chemeon-tcp-hf.html.

[75]. SurTec. SurTec 650: Chromium (VI)-Free Passivation for Aluminium for the Electronics,-Automotive and Aerospace Industry [Internet]. [Place unknown: SurTec]; [Cited 2018 Sep]. Available from: https://www.surtec.com/en/products/product-highlights/628/.

[76]. ATOTECH. Interlox® 5707: Phosphate-free paint pretreatment for multimetal applocations [Internet]. [Place unknown: ATOTECH]; [cited 2018 Sep]. Available from: https://www.atotech.com/paint-support-technologies/interlox-5707/.

[77]. PPG Industrial Coatings. ZIRCOBOND® and X-BONDTM: Zirconium-Based Thin-Film Pretreatment System [Internet]. [Place unknown: PPG Industrial Coatings]; [cited 2018 Sep]. Available from: http://www.ppgindustrialcoatings.com/getmedia/591ca2e3-ec3d-4f60-9315-5bd2b9e37159/Zircobond-X-Bond-Sell-Sheet_v2-02-06-16LowRes.pdf.aspx.

[78]. Blawert, C., Dietzel, W., Ghali, E., & Song, G. (2006). Anodizing treatments for magnesium alloys and their effect on corrosion resistance in various environments. Advanced Engineering Materials, 8(6), 511-533.

[79]. Jiang, B. L., & Ge, Y. F. (2013). Micro-arc oxidation (MAO) to improve the corrosion resistance of magnesium (Mg) alloys. In Corrosion Prevention of Magnesium Alloys (pp. 163-196).

[80]. Song, G. L., & Shi, Z. (2013). Anodization and corrosion of magnesium (Mg) alloys. In Corrosion Prevention of Magnesium Alloys (pp. 232-281).

[81]. Coating Applications [Internet]. [Place unknown: Technology Applications Group]; [cited 2018 Sep]. Available from: http://www.tagnite.com/applications/#?201,115.

[82]. Esmaily, M., Svensson, J. E., Fajardo, S., Birbilis, N., Frankel, G. S., Virtanen, S., & Johansson, L. G. (2017). Fundamentals and advances in magnesium alloy corrosion. Progress in Materials Science, 89, 92-193.

[83]. Blawert, C., Dietzel, W., Ghali, E., & Song, G. (2006). Anodizing treatments for magnesium alloys and their effect on corrosion resistance in various environments. Advanced Engineering Materials, 8(6), 511-533.

[84]. Azumi, K., Elsentriecy, H. H., & Tang, J. (2013). Plating techniques to protect magnesium (Mg) alloys from corrosion. In Corrosion Prevention of Magnesium Alloys (pp. 347-369).

[85]. Chen, X. B., Easton, M. A., Birbilis, N., Yang, H. Y., & Abbott, T. B. (2013). Corrosion-resistant electrochemical plating of magnesium (Mg) alloys. In Corrosion Prevention of Magnesium Alloys (pp. 315-346).

[86]. Lei, X. P., Yu, G., Zhu, Y. P., Zhang, Z. P., He, X. M., Hu, B. N., Chen, Y. (2010). Successful cyanide free plating protocols on magnesium alloys. Transactions of the IMF, 88(2), 75-80.

[87]. Hu, R. G., Zhang, S., Bu, J. F., Lin, C. J., & Song, G. L. (2012). Recent progress in corrosion protection of magnesium alloys by organic coatings. Progress in Organic Coatings, 73(2-3), 129-141.

[88]. Wang, G. G., Stewart, K., Berkmortel, R., & Skar, J. I. (2001). Corrosion prevention for external magnesium automotive components (No. 2001-01-0421). SAE Technical Paper.

[89]. Brady, M. P., Joost, W. J., & David Warren, C. (2016). Insights from a Recent Meeting: Current Status and Future Directions in Magnesium C.

[90]. Magnesium Coatings Suppliers. Thomas, 2018. Available from: https://www.thomasnet.com/products/magnesium-coatings-15800535-1.html.

[91]. Magnesium Coatings Suppliers [Internet]. [Place unknown: Thomas]; [Updated 2018 Sep, cited 2018 Sep]. Available from: https://www.thomasnet.com/products/magnesium-coatings-15800535-1.html.

[92]. Guo L, Wu W, Zhou Y, et al. (2018) Layered double hydroxide coatings on magnesium alloys: A review. J Mater Sci Technol 34: 1455–1466.

[93]. Zhang G, Wu L, Tang A, et al. (2017) A novel approach to fabricate protective layered double hydroxide films on the surface of anodized Mg-Al alloy. Adv Mater Interfaces 4: 1700163.

[94]. Wu L, Zhang G, Tang A, et al. (2017) Communication—fabrication of protective layered double hydroxide films by conversion of anodic films on magnesium alloy. J Electrochem Soc 164: C339–C341.

[95]. Wu L, Yang D, Zhang G, et al. (2018) Fabrication and characterization of Mg-M layered double hydroxide films on anodized magnesium alloy AZ31. Appl Surf Sci 431: 177–186.

[96]. Zeng RC, Liu ZG, Zhang F, et al. (2014) Corrosion of molybdate intercalated hydrotalcite coating on AZ31 Mg alloy. J Mater Chem A 2: 13049–13057.

[97]. Adsul SH, Raju KRCS, Sarada BV, et al. (2018) Evaluation of self-healing properties of inhibitor loaded nanoclay-based anticorrosive coatings on magnesium alloy AZ91D. J Magnesium Alloy 6: 299–308.

[98]. Bala, N., Singh, H., Karthikeyan, J., & Prakash, S. (2014). Cold spray coating process for corrosion protection: a review. Surface Engineering, 30(6), 414-421.

[99]. Hassani-Gangaraj, S. M., Moridi, A., & Guagliano, M. (2015). Critical review of corrosion protection by cold spray coatings. Surface Engineering, 31(11), 803-815.

[100]. Mahmoudi-Asl, Hassan. *The Effect of Cold Spray Coating on Fatigue Life of Magnesium Alloy, AZ31B*. MS thesis. University of Waterloo, 2011.

[101]. Spencer, K., Fabijanic, D. M., & Zhang, M. X. (2009). The use of Al–Al2O3 cold spray coatings to improve the surface properties of magnesium alloys. Surface and Coatings Technology, 204(3), 336-344.

[102]. Wang, Q., Spencer, K., Birbilis, N., & Zhang, M. X. (2010). The influence of ceramic particles on bond strength of cold spray composite coatings on AZ91 alloy substrate. Surface and Coatings Technology, 205(1), 50-56.

[103]. DeForce, B. S., Eden, T. J., & Potter, J. K. (2011). Cold spray Al-5% Mg coatings for the corrosion protection of magnesium alloys. Journal of Thermal Spray Technology, 20(6), 1352-1358.

[104]. Bu, H., Yandouzi, M., Lu, C., MacDonald, D., & Jodoin, B. (2012). Cold spray blended Al+ Mg17Al12 coating for corrosion protection of AZ91D magnesium alloy. Surface and Coatings Technology, 207, 155-162.

[105]. Hou, Jian, and Li Song. "Numerical investigation on stress concentration of tension steel bars with one or two corrosion pits." Advances in Materials Science and Engineering 2015 (2015).

[106]. Ebara, R. "Corrosion fatigue phenomena learned from failure analysis." Engineering Failure Analysis 13.3 (2006): 516-525.

[107]. Buxton, D. C., et al. "Life prediction in corrosion fatigue." *Proc. Int. Conf. Corrosion-Deformation Interaction, Fontainebleau, France*. 1992.

[108]. Wei, R. P. "Environmental considerations for fatigue cracking." *Fatigue & Fracture of Engineering Materials & Structures* 25.8-9 (2002): 845-854.

[109]. Kondo, Y. "Prediction of fatigue crack initiation life based on pit growth." *Corrosion* 45.1 (1989): 7-11.

[110]. Ishihara, S., et al. "Prediction of corrosion fatigue lives of aluminum alloy on the basis of corrosion pit growth law." *Fatigue & Fracture of Engineering Materials & Structures* 29.6 (2006): 472-480.

[111]. Rajasankar, J., and Nagesh R. Iyer. "A probability-based model for growth of corrosion pits in aluminum alloys." *Engineering fracture mechanics* 73.5 (2006): 553-570.

[112]. Harlow, D. Gary, and Robert P. Wei. "Probability approach for prediction of corrosion and corrosion fatigue life." *AIAA journal* 32.10 (1994): 2073-2079.

[113]. Mao, Miaodong, et al. "Prediction of crack initiation life due to corrosion pits." *Journal of Aircraft* 51.3 (2014): 805-810.

[114]. Sriraman, M. R., and R. M. Pidaparti. "Crack initiation life of materials under combined pitting corrosion and cyclic loading." *Journal of Materials Engineering and Performance* 19.1 (2010): 7-12.

[115]. Chen G S, Wan K C, Gao M, et al. Transition from pitting to fatigue crack growth—modeling of corrosion fatigue crack nucleation in a 2024-T3 aluminum alloy [J]. Materials Science and Engineering: A, 1996, 219(1-2): 126-132.

[116]. Hu, Ping, et al. "A continuum damage mechanics approach coupled with an improved pit evolution model for the corrosion fatigue of aluminum alloy." Corrosion Science 113 (2016): 78-90.

[117]. Amiri M, Arcari A, Airoldi L, et al. A continuum damage mechanics model for pit-to-crack transition in AA2024-T3 [J]. Corrosion Science, 2015, 98: 678-687.

[118]. Bannantine, Julie. "Fundamentals of metal fatigue analysis." *Prentice Hall*, *1990*, (1990): 273.

[119]. Hoeppner, D. W., V. Chandrasekaran, and A. M. H. Taylor. "Review of pitting corrosion fatigue models." *International Committee on Aeronautical Fatigue* (1999).

[120]. Pidaparti, Ramana M., and Ronak R. Patel. "Correlation between corrosion pits and stresses in Al alloys." *Materials Letters* 62.30 (2008): 4497-4499.

[121]. Cerit, M., K. Genel, and S. Eksi. "Numerical investigation on stress concentration of corrosion pit." *Engineering Failure Analysis* 16.7 (2009): 2467-2472.

[122]. Zhao, Wei, et al. "Correlation between the geometric parameters of corrosion pit and stress concentration factor." *Applied Mechanics and Materials*. Vol. 327. Trans Tech Publications, 2013.

[123]. Wei, R. P., and G. W. Simmons. "Recent progress in understanding environment assisted fatigue crack growth." *International Journal of Fracture* 17.2 (1981): 235-247.

[124]. Wei, R. P. "On understanding environment-enhanced fatigue crack growth—a fundamental approach." *Fatigue Mechanisms*. ASTM International, 1979.

[125]. Wei, R. P., and Ming Gao. "Reconsideration of the superposition model for environmentally assisted fatigue crack growth." *Scripta metallurgica* 17.7 (1983): 959-962.

[126]. Landes, J. D., and R. P. Wei. "The kinetics of subcritical crack growth under sustained loading." *International Journal of Fracture* 9.3 (1973): 277-293.

[127]. Kim, Y. H., and S. D. Manning. "A Superposition Model for Corrosion-Fatigue Crack Propagation in Aluminum Alloys." *Fracture Mechanics: Fourteenth Symposium—Volume I: Theory and Analysis*. ASTM International, 1983.

[128]. Weng, Lin, et al. "Corrosion fatigue crack growth of AISI 4340 steel." International Journal of Fatigue 48 (2013): 156-164.

[129]. Austen, I. M., and P. McIntyre. "Corrosion fatigue of high-strength steel in low-pressure hydrogen gas." *Metal Science* 13.7 (1979): 420-428.

[130]. Rhodes, D., J. K. Musuva, and J. C. Radon. "The significance of stress corrosion cracking in corrosion fatigue crack growth studies." *Engineering Fracture Mechanics* 15.3-4 (1981): 407-419.

[131]. Gryguc, Andrew, et al. "Monotonic and cyclic behaviour of cast and cast-forged AZ80 Mg." International Journal of Fatigue 104 (2017): 136-149.

[132]. Karparvarfard, S. M. H., et al. "Microstructure, texture and mechanical behavior characterization of hot forged cast ZK60 magnesium alloy." Journal of Materials Science & Technology 33.9 (2017): 907-918.

[133]. E8/E8M，ASTM, Standard test methods for tension testing of metallic materials, ASTM. (2010) 1–27. doi:10.1520/E0008.

[134]. Fan, Xiao-Li, et al. "Corrosion resistance of nanostructured magnesium hydroxide coating on magnesium alloy AZ31: influence of EDTA." Rare Metals 38.6 (2019): 520-531.

[135]. Baudrand, Dan. "Conversion coatings for aluminum and magnesium." Plating and surface finishing 92.1 (2005): 30-34.

[136]. Lev Deresh. "Composition and method for producing chromate conversion coatings composition." European Patent No. 0451409A1. 16 Oct. 1991.

[137]. Standard, A. S. T. M. "G3,“Standard Practice for Conventions Applicable to Electrochemical Measurements in Corrosion Testing”." Annual Book of ASTM Standards, ASTM International, West Conshohocken, PA 3 (2006).

[138]. Standard, A. S. T. M. (1997). B117. Standard practice for operation salt spray (fog) apparatus, 3(2).

[139]. YING-YU, L., and W. QUI-DONG. "ASTM D 1654: standard test method for evaluation of painted or coated specimens subjected to corrosive environments." Annual Book of ASTM Standards. West Conshohocken (1992).

[140]. SAE J2334. (2003). Laboratory Cyclic Corrosion Test.

[141]. Borhan Dayani, Siavash. Improvement of fatigue and corrosion-fatigue resistance of AZ31B cast alloy by cold spray coating and top coating. MS thesis. University of Waterloo, 2017.

[142]. Chen, Xiao-Bo, et al. "Double-layered manganese phosphate conversion coating on magnesium alloy AZ91D: Insights into coating formation, growth and corrosion resistance." Surface and Coatings Technology 217 (2013): 147-155.

[143]. Cui, Xue-jun, et al. "Duplex-layered manganese phosphate conversion coating on AZ31 Mg alloy and its initial formation mechanism." Corrosion science 76 (2013): 474-485.

[144]. Yan, Y. "Tribology and tribo-corrosion testing and analysis of metallic biomaterials." Metals for Biomedical Devices. Woodhead Publishing, 2010. 178-201.

[145]. Lasia, Andrzej. "Electrochemical impedance spectroscopy and its applications." Modern aspects of electrochemistry. Springer, Boston, MA, 2002. 143-248.

[146]. Xue, Yuna, et al. "Corrosion performances of micro-arc oxidation coatings on Az31B, Az80 and Zk60 cast Mg alloys." (2018).

[147]. Xue, Yuna, et al. "Characterization of the corrosion performances of as-cast Mg–Al and Mg–Zn magnesium alloys with microarc oxidation coatings." Materials and Corrosion 71.6 (2020): 992-1006.

[148]. Xue, Yuna, et al. "Corrosion and corrosion fatigue performances of micro-arc oxidation coating on AZ31B cast magnesium alloy." Materials and Corrosion 70.2 (2019): 268-280.

[149]. Wang, Jie, Hamid Jahed, and Xin Pang. "A two-stage conversion process for AZ31B corrosion." (2018).

[150]. Zhao, Ming-Chun, et al. "Influence of the β-phase morphology on the corrosion of the Mg alloy AZ91." Corrosion Science 50.7 (2008): 1939-1953.

[151]. Gusieva, K., et al. "Corrosion of magnesium alloys: the role of alloying." International Materials Reviews 60.3 (2015): 169-194.

[152]. Stewart, Ao T. "The influence of environment and stress ratio on fatigue crack growth at near threshold stress intensities in low-alloy steels." Engineering Fracture Mechanics 13.3 (1980): 463-478.

[153]. Adedipe, O., F. Brennan, and A. Kolios. "Corrosion fatigue load frequency sensitivity analysis." Marine Structures 42 (2015): 115-136.

[154]. Kakiuchi, Toshifumi, et al. "Effect of hydrogen on fatigue crack propagation behavior of wrought magnesium alloy AZ61 in NaCl solution under controlled cathodic potentials." Engineering Fracture Mechanics 137 (2015): 88-96.

[155]. En-Hou, Han, and Ke Wei. "Chemical and electrochemical conditions within corrosion fatigue cracks." Corrosion science35.1-4 (1993): 599-610.

[156]. Suresh, S., and R. O. Ritchie. "A geometric model for fatigue crack closure induced by fracture surface roughness." Metallurgical transactions A 13.9 (1982): 1627-1631.

[157]. Wan, K-C., et al. "Interactions between mechanical and environmental variables for short fatigue cracks in a 2024-T3 aluminum alloy in 0.5 M NaCl solutions." Metallurgical and Materials Transactions A 31.3 (2000): 1025-1034.

[158]. Vasudevan, A. K., and K. Sadananda. "Classification of environmentally assisted fatigue crack growth behavior." *International Journal of Fatigue* 31.11 (2009): 1696-1708.

[159]. Paris, Paul Croce, and Fazil Erdogan. "A critical analysis of crack propagation laws." ASME, 1963.

[160]. Elber, Wolf. "The significance of fatigue crack closure." *Damage tolerance in aircraft structures*. ASTM International, 1971.

[161]. Kujawski, Daniel. "Enhanced model of partial crack closure for correlation of R-ratio effects in aluminum alloys." *International Journal of Fatigue* 23.2 (2001): 95-102.

[162]. Kujawski, D. "ΔK eff parameter under re-examination." *International Journal of Fatigue* 25.9 (2003): 793-800.

[163]. Macha, D. E., D. M. Corbly, and J. W. Jones. "On the variation of fatigue-crack-opening load with measurement location." *Experimental Mechanics* 19.6 (1979): 207-213.

[164]. Shih, T. T., and Robert Peh-ying Wei. "A study of crack closure in fatigue." *Engineering Fracture Mechanics* 6.1 (1974): 19-32.

[165]. Donald, Keith, and Paul C. Paris. "An evaluation of ΔK eff estimation procedures on 6061-T6 and 2024-T3 aluminum alloys." *International Journal of fatigue* 21 (1999): S47-S57.

[166]. Kujawski, Daniel. "A fatigue crack driving force parameter with load ratio effects." International Journal of Fatigue 23 (2001): 239-246.

[167]. Hertzberg, R. W., C. H. Newton, and R. Jaccard. "Crack closure: correlation and confusion." Mechanics of fatigue crack closure. ASTM International, 1988.

[168]. Vasudeven, A. K., K. Sadananda, and N. Louat. "A review of crack closure, fatigue crack threshold and related phenomena." Materials Science and Engineering: A 188.1-2 (1994): 1-22.

[169]. Sadananda, K., and A. K. Vasudevan. "Analysis of fatigue crack closure and thresholds." Fracture Mechanics: 25th Volume. ASTM International, 1995

[170]. Garrett, G. G., and J. F. Knott. "On the effect of crack closure on the rate of fatigue crack propagation." International Journal of Fracture 13.1 (1977): 101-104.

[171]. Glinka, G., and A. Buczynski. "Experimental and numerical analysis of elastic-plastic strains and stresses ahead of a growing fatigue crack." Giornata IGF Forni di Sopra (UD) 2011. 2011.

[172]. Walker, K. "The effect of stress ratio during crack propagation and fatigue for 2024-T3 and 7075-T6 aluminum." *Effects of environment and complex load history on fatigue life*. ASTM International, 1970.

[173]. Sadananda, K., and Dorai-Nirmal V. Ramaswamy. "Role of crack tip plasticity in fatigue crack growth." Philosophical Magazine A 81.5 (2001): 1283-1303.

[174]. Kujawski, Daniel. "A new (ΔK+ Kmax) 0.5 driving force parameter for crack growth in aluminum alloys." International Journal of Fatigue 23.8 (2001): 733-740.

[175]. Sadananda, K., A. K. Vasudevan, and I. W. Kang. "Effect of superimposed monotonic fracture modes on the ΔK and Kmax parameters of fatigue crack propagation." Acta Materialia51.12 (2003): 3399-3414.

[176]. Sadananda, K., and A. K. Vasudevan. "Crack tip driving forces and crack growth representation under fatigue." International Journal of Fatigue 26.1 (2004): 39-47.

[177]. Stoychev, Stoyan, and Daniel Kujawski. "Analysis of crack propagation using ΔK and Kmax." International Journal of Fatigue 27.10-12 (2005): 1425-1431.

[178]. Sadananda, K., A. K. Vasudevan, and R. L. Holtz. "Extension of the unified approach to fatigue crack growth to environmental interactions." International Journal of Fatigue23 (2001): 277-286.

[179]. Oda, Yasuji, et al. "AFM and SEM observation on mechanism of fatigue crack growth in an Fe-Si single crystal." International Journal of Fracture 113.3 (2002): 213-231.

[180]. Fong, Clinton, and Desmond Tromans. "Stage I corrosion fatigue crack crystallography in austenitic stainless steel (316L)." Metallurgical Transactions A 19.11 (1988): 2765-2773.

[181]. Vasudevan, A. K., K. Sadananda, and N. Iyyer. "Fatigue damage analysis: Issues and challenges." International Journal of Fatigue 82 (2016): 120-133.

[182]. Glinka, G. "A notch stress-strain analysis approach to fatigue crack growth." Engineering Fracture Mechanics 21.2 (1985): 245-261.

[183]. Noroozi, A. H., G. Glinka, and S. Lambert. "A two parameter driving force for fatigue crack growth analysis." International Journal of Fatigue 27.10-12 (2005): 1277-1296.

[184]. Chowdhury, P., and H. Sehitoglu. "Mechanisms of fatigue crack growth–a critical digest of theoretical developments." Fatigue & Fracture of Engineering Materials & Structures 39.6 (2016): 652-674.

[185]. Laird, Campbell. "The influence of metallurgical structure on the mechanisms of fatigue crack propagation." Fatigue crack propagation. ASTM International, 1967.

[186]. Wang, Rong. "A fracture model of corrosion fatigue crack propagation of aluminum alloys based on the material elements fracture ahead of a crack tip." International Journal of Fatigue 30.8 (2008): 1376-1386.

[187]. Shipilov, S. A. "Mechanisms for corrosion fatigue crack propagation." Fatigue & Fracture of Engineering Materials & Structures 25.3 (2002): 243-259.

[188]. Barsom, J. M. "Mechanisms of corrosion fatigue below K Iscc." International Journal of Fracture Mechanics 7.2 (1971): 163-182.

[189]. Ramsamooj, D. V., and T. A. Shugar. "Modeling of corrosion fatigue in metals in an aggressive environment." International Journal of Fatigue 23 (2001): 301-309.

[190]. Feeney, John A., J. Corey Mcmillan, and Robert P. Wei. "Environmental fatigue crack propagation of aluminum alloys at low stress intensity levels." Metallurgical Transactions 1.6 (1970): 1741-1757.

[191]. Pippan, R., et al. "On the mechanism of fatigue crack propagation in ductile metallic materials." Fatigue & Fracture of Engineering Materials & Structures 34.1 (2011): 1-16.

[192]. Lee, E. U., and A. K. Vasudevan. "Environmentally influenced fatigue in high strength steels." Journal of ASTM International2.3 (2005): 1-13.

[193]. Weng, Lin, et al. "Corrosion fatigue crack growth of AISI 4340 steel." International Journal of Fatigue 48 (2013): 156-164.

[194]. Sadananda, K., and A. K. Vasudevan. "Fatigue crack growth behavior of titanium alloys." International Journal of Fatigue 27.10 (2005): 1255-1266.

[195]. Pao, P. S., and R. L. Holtz. Corrosion-Fatigue Cracking in Al 7075 Alloys. No. NRL/MR/6355--14-9582. NAVAL RESEARCH LAB WASHINGTON DC, 2014.

[196]. Hall, L. R., R. W. Finger, and W. F. Spurr. Corrosion fatigue crack growth in aircraft structural materials. BOEING AEROSPACE CO SEATTLE WA, 1973.

[197]. Sadananda, K., and A. K. Vasudevan. "Crack growth behavior of 4340 steel under corrosion and corrosion fatigue conditions." Corrosion Reviews 33.6 (2015): 335-349.

[198]. Wei, R. P. "Some aspects of environment-enhanced fatigue-crack growth." Engineering Fracture Mechanics 1.4 (1970): 633-651.

[199]. Kawai, S., and K. Koibuchi. "Effect of waveform on corrosion fatigue crack growth." Fatigue & Fracture of Engineering Materials & Structures 1.4 (1979): 395-407.

[200]. ASTM International. E647-15e1 Standard Test Method for Measurement of Fatigue Crack Growth Rates. West Conshohocken, PA; ASTM International, 2015.

[201]. Parkins, R. N. "Environmental effects in crack growth." Journal of Strain Analysis 10.4 (1975): 251-257.

[202]. Suresh, So, and R. O. Ritchie. "Propagation of short fatigue cracks." International Metals Reviews 29.1 (1984): 445-475.